

ABSTRACT

GUO, SIJIA. High-Intensity Ultrasound in Adherent Cell Sorting and Tissue Ablation. (Under the direction of Dr. Xiaoning Jiang).

High-power ultrasound has been applied in many biomedical applications. However, many new applications and the associated challenges need to be addressed to advance high power ultrasound technology in medicine and biology. In this dissertation, the research objectives are: (1) to explore new high-intensity focused ultrasound (HIFU) applications in biology; (2) to enhance tissue ablation efficiency for more power efficient HIFU therapies. In order to achieve these objectives, several tasks were executed, and the background, design method and materials, experimental results and conclusions for each task were presented.

To explore new HIFU application in biology, the use of ultrasonic waves to release pallets for isolation of adherent live cells was investigated with high cell survivability. This technique has the potential for use in high-throughput cell sorting. This highly selective pallet/cell release method yields significantly higher cell viability after single-pallet release, comparing with other existing methods, largely resulting from the relatively slow release speed and low radiation forces.

To investigate more efficient HIFU therapies, a combined modeling and experimentation approach was employed to understand the physics behind the differences in tissue ablation behavior between single- and multi-frequency ultrasound. It is found that tissue ablation using multi-frequency HIFU yielded a up to 37.9 % higher temperature rise rate compared to ablation using single-frequency HIFU under the same exposure power and time. This finding has been verified by both thermocouple and MRI measurements, but cannot be explained

well by the Pennes bio-heating theory, which does not consider cavitation. This more effective tissue ablation using multi-frequency HIFU is likely attributed to the enhanced cavitation effect based on the obtained cavitation detection results.

To investigate the cavitation effect under multi-frequency sonications, the enhanced effect of dual-frequency ultrasonic irradiation on cavitation yield was reported, for the first time, via the cavitation bubble modeling, followed by the cavitation yield characterization using the PCD (passive cavitation detection) method. Two-frequency (1.5 MHz/3 MHz) orthogonal pulse ultrasound was used in the tests. It was found that the simultaneous irradiation of dual frequency ultrasound can produce a significant increase in cavitation yield compared with single frequency irradiation. The possible mechanisms of the enhanced effect were briefly discussed and explained by the single-bubble cavitation model, where the calculated radiated pressure generated by acoustic bubble cavitation was found to be greater in dual-frequency cases.

Both the ultrasonic cell sorting study and the multi-frequency HIFU study suggest that high power ultrasound is promising for a broader range of applications in medicine and biology.

© Copyright 2015 Sijia Guo

All Rights Reserved

High-Intensity Ultrasound in Adherent Cell Sorting and Tissue Ablation

by
Sijia Guo

A dissertation submitted to the Graduate Faculty of
North Carolina State University
in partial fulfillment of the
requirements for the degree of
Doctor of Philosophy

Mechanical Engineering

Raleigh, North Carolina

2015

APPROVED BY:

Dr. Xiaoning Jiang
Chair of Advisory Committee

Dr. Nancy Allbritton

Dr. Yun Jing

Dr. Fuh-Gwo Yuan

DEDICATION

To my family who always support me.

BIOGRAPHY

Sijia Guo received his B. S. degree from the Department of Mechanical Engineering at Zhejiang University, China, in 2009. In August 2009, he started pursuing his Ph.D. degree in the department of Mechanical and Aerospace Engineering at North Carolina State University, Raleigh, NC. Currently he is working as a research assistant at the Micro/Nano Engineering Laboratory, directed by Dr. Xiaoning Jiang. His main research interests are ultrasound transducer design, and acoustic field modeling and applications of ultrasound.

The following publications were authored or co-authored by Sijia Guo in peer-reviewed journals and conference proceedings during his study at North Carolina State University:

Journal articles,

S. Guo, C. Eldeniz, L. Phillips, W. Lin, P. Dayton and X. Jiang, "MR-compatible multi-frequency ultrasound for tissue ablation" , *Ultrasound in Medicine & Biology*, submitted, 2014.

S. Guo, Y. Jing and X. Jiang, "Temperature rise in tissue ablation using multi-frequency ultrasound", *Ultrasonics, Ferroelectrics and Frequency Control, IEEE Transactions on*, vol. 60(8), 2013.

J. Ma, S. Guo, D. Wu, X. Geng and X. Jiang, "Design, fabrication, and characterization of a single-aperture 1.5-MHz/3-MHz dual-frequency HIFU transducer", *IEEE Transactions on Ultrasonics, Ferroelectrics and Frequency Control*, vol. 60(7), 2013.

Guo, S., Y. Wang, N. Allbritton and X. Jiang, "Ultrasound-induced release of micropallets with cells", *Applied Physics Letters*, vol. 101(16), 163703, 2012.

Conference Proceedings

S. Guo and X. Jiang, "Enhancement of ultrasonic cavitation yield by dual-frequency sonication", *ASME*, accepted, 2014.

S. Guo, X. Jiang, and W. Lin, "Tissue ablation using multi-frequency focused ultrasound", *IEEE Ultrasonic Symposiums*, Orlando, October, 2011.

S. Bakshi, S. Guo, and X. Jiang, "Multi-frequency focused ultrasound for tissue ablation", *ASME*, IMECE2011-64076, Denver, November, 2011.

ACKNOWLEDGMENTS

First and foremost, I'm very thankful for my advisor, Dr. Xiaoning Jiang, for supporting and guiding me in my graduate studies for the past four years. He taught me how to be an independent researcher and a self-motivated person no matter what you are working on, which will guide me in my future career and my entire life.

I am thankful for my advisory committee members, Dr. Nancy Allbritton, Dr. Yun Jing and Dr. Fuh-Gwo Yuan for their support and advice on my research. I would also like to acknowledge Dr. Paul Dayton, Dr. Weili Lin and their groups at University of North Carolina, Chapel Hill for their help.

It's been a pleasure working in the Micro&Nano Engineering Lab at North Carolina State University for the last four years. I'm thankful for interesting discussions and help that I've received from my lab mates, Laura, Kim, Saurabh, Wenbin, Vish, Jianguo, Gio. Dr. Wu, Seol, Wei-Yi, Sibbo, Zhuochen, Joe, Dr. Jian, Dr. Hsieh and Jinwook, who always help and encourage me as friends. Again, I would thank Dr. Jiang to give this opportunity of working in such an exciting laboratory and doing exciting research.

Last but not the least, I'd like to thank all friends and family, especially my parents, for their support.

TABLE OF CONTENTS

LIST OF TABLES.....	ix
LIST OF FIGURES.....	x
CHAPTER 1 Introduction.....	1
1.1 High power ultrasound	1
1.1.1 Ultrasound	1
1.1.2 High intensity focused ultrasound (HIFU)	5
1.2 High intensity ultrasound applications.....	10
1.2.1 High power ultrasound for thermal ablation.....	14
1.2.2 High power ultrasound for cell sorting	15
1.3 Objectives.....	16
CHAPTER 2 Ultrasonic cell sorting.....	19
2.1 Background.....	19
2.1.1 Cell sorting	19
2.1.2 Microarray technologies for adherent sorting	21
2.1.3 Ultrasound for cell manipulation.....	26
2.1.4 Motivation and objective	28
2.2 Micro-pallet release modeling.....	28
2.2.1 Acoustic radiation force modeling	28
2.2.2 Acoustic cavitation modeling	31
2.2.3 Attraction force and global force balance	32
2.3 Experimental method	33
2.3.1 Micropallet arrays and HeLa cells preparation	33
2.3.2 Experimental setup	35
2.4 Results and discussion.....	37
2.4.1 Experimental results	37
2.4.2 Modeling results and discussion	42
2.5 Summary	45
CHAPTER 3 Tissue ablation using multi-frequency ultrasound.....	46

3.1	Background	46
3.1.1	Tissue ablation using high-intensity focused ultrasound (HIFU).....	46
3.1.2	Objective and approach.....	51
3.2	Tissue ablation modeling	52
3.2.1	Acoustic field modeling.....	52
3.2.2	Temperature rise modeling.....	55
3.3	Experimental method	57
3.3.1	Ultrasound transducers.....	57
3.3.2	Tissue ablation monitoring using a thermocouple.....	61
3.3.3	Tissue-mimicking phantom ablation in a magnetic resonance imaging (MRI) environment	63
3.4	Results and discussion	66
3.4.1	Modeling results.....	66
3.4.2	Experimental results.....	71
3.4.3	Discussion.....	79
3.5	Summary	82
CHAPTER 4 Multi-frequency cavitation study		84
4.1	Background	84
4.1.1	Cavitation effect and physics.....	84
4.1.2	Multi-frequency ultrasound for cavitation enhancement.....	86
4.1.3	Motivation, objective and approach.....	87
4.2	Bubble cavitation modeling	88
4.2.1	Bubble dynamics modeling.....	88
4.2.2	Radiated force modeling.....	91
4.3	Experimental method	91
4.4	Results and discussion	93
4.4.1	Bubble cavitation modeling results.....	93
4.4.2	Experimental results.....	101
4.5	Summary	104
CHAPTER 5 Conclusions		106

REFERENCES..... 108

APPENDICES..... 126

Appendix I..... 127

Appendix II..... 137

Appendix III..... 142

LIST OF TABLES

Table 2-1. Acoustic radiation pressure under 1 MPa, 3.3 MHz ultrasound wave.	43
Table 3-1. Characteristics of ultrasound transducers used in tissue ablation experiments.	58
Table 3-2. Input voltages for 25 W input power under different frequencies and the corresponding output acoustic powers.	61
Table 3-3. Measured temperature rise (°C) at 10 seconds, 20 seconds and 30 seconds during the ablation experiments under different HIFU configurations.	76
Table 3-4. Summarized enhancement on temperature rise by multi-frequency ultrasound.	80

LIST OF FIGURES

Figure 1-1. Approximate frequency ranges corresponding to ultrasound, with general guide of some applications [1].	2
Figure 1-2. A plane-wave sound source and its wavefront.	3
Figure 1-3. Examples of ultrasound applications.	4
Figure 1-4. Illustration of a focused ultrasound transducer.	7
Figure 1-5. The acoustic pressure distribution for a 1.5 MHz ultrasound transducer. The axial direction is the acoustic emitting direction. (a) 2D pressure distribution along the axial and lateral directions. (b) pressure distribution along the acoustic axis.	9
Figure 1-6. Examples for high-intensity focused ultrasound applications.	11
Figure 1-7. Particles within acoustic field will be forced from higher-intensity area to lower-intensity area in the parallel plane of the ultrasound surface, and spontaneously forced along the acoustic transmitting direction by acoustic radiation force.	13
Figure 1-8. The use of ultrasound provides specific activation based on a physical phenomenon: acoustic cavitation [20].	14
Figure 2-1. Sketch of a 500- μm SU-8 micropallet array on a glass substrate.	23
Figure 2-2. Experimental system for laser-based pallet release [64].	24
Figure 2-3. Micraft release by a tiny needle [31].	25
Figure 2-4. A radiation force acting on a density media causes fluidic movement.	27
Figure 2-5. Acoustic radiation force on an arbitrary particle generated by a plane wave. P_0 is the acoustic pressure of the plan wave, after the absorption of the particle, the pressure difference cause the acoustic radiation force.	29

Figure 2-6. Pressure field simulation of the 3.3 MHz transducer used in pallet release tests on 500 μm samples. The output acoustic power is 30 W. (Unit: MPa).....	30
Figure 2-7. Microbubbles generated radiated force (black arrows).....	31
Figure 2-8. Image of SU-8 micropallet array with square pallets having a 200 μm side lengths and 100 μm height taken by a measuring microscope (Olympus STM6, Olympus, Center Valley, PA).....	34
Figure 2-9. Schematic of the experimental setup for pallet release.	36
Figure 2-10. (a) Single pallet was released by 15 W input power after 10 seconds. (b) Two pallets were released by 20 W input power after 5 seconds. (c) Four pallets were released by 30 W input power after 5 seconds. (d) Nine pallets were released by 30 W input power after 15 seconds.....	38
Figure 2-11. Ultrasound induced pallet release with HeLa cells (shown in green). (a)-(b) Selective release of a single 500 μm micropallet with HeLa cells. Pallet array before the single pallet release (arrow points to the pallet to be released) (a), and after released (b). (c)-(e) Collected 500 μm micropallet with HeLa cells. (e) Merged image. 95 cells (stained both green and red) from a total number of 109 were alive. Scale bar = 500 μm	39
Figure 2-12. Photograph pictures from a movie (7 ms) of pallet release process recorded using a high-speed camera. Scale bar = 500 μm	41
Figure 2-13. The relationship between working frequency and -6 dB ultrasonic beam width at fixed F number (Focal length = 30 mm, diameter of aperture = 29 mm).	43
Figure 2-14. Acoustic cavitation modeling. The radiated pressure is calculated under 1 MPa, 3.3 MHz ultrasonic sonication.	44

Figure 3-1. Focused ultrasound on tumor treatment [89].	46
Figure 3-2. Schematic diagram of dual-frequency HIFU lesioning apparatus [9].	49
Figure 3-3. Photographs of lesions in the degassed liver samples induced by dual-frequency HIFU and conventional single-frequency HIFU (from 1 to 5, the exposure times are 10, 15, 20, 25 and 30 s, respectively) [9].	49
Figure 3-4. Experimental setup of dual-beam orthogonal low MHz sonication.	50
Figure 3-5. The amount of I2 released (represent the cavitation efficiency) under dual-beam orthogonal low MHz ultrasound [100].	50
Figure 3-6. Schematic diagrams of tissue ablation using different HIFU configurations in simulations. (a) con-focal dual-frequency configuration; (b) separated dual-frequency configuration.	55
Figure 3-7. Schematic of the acoustic beam focal zone length and diameter (units of mm) of ultrasound transducers: 950 kHz transducer (top), 1.5 MHz transducer (middle) and 3.3 MHz transducer (bottom).	58
Figure 3-8. Configuration of the dual frequency transducer. Arrows on the transducer around “P” indicate the polarization direction [109].	60
Figure 3-9. Schematic diagram of the experimental setup of dual-frequency tissue ablation tests using a thermocouple for temperature measurement.	62
Figure 3-10. Schematic diagram of the tissue-mimicking phantom ablation tests in a MR scanner using a dual-frequency HIFU transducer. The HIFU transducer could be plugged into the fixture through the upper red arrow, and the gelatin phantom is placed at the bottom.....	66
Figure 3-11. Simulation of acoustic pressure spectrum at the focal point while assuming dual-	

frequency ultrasound beams were emitted from a dual-frequency source as shown in Fig. 2(a).	67
Figure 3-12. Simulation of acoustic pressure spectrum at the focal point while assuming dual-frequency ultrasound beams were emitted from two separated transducers as shown in Fig. 2(b).	68
Figure 3-13. Simulated acoustic pressure field of (a) 950 kHz transducer, (b) 1.5 MHz transducer.	70
Figure 3-14. Simulated temperature vs. time of single- and dual-frequency tests between 950 kHz and 1.5 MHz under 15 W total input power for 30 seconds.	70
Figure 3-15. Measured change in chicken tissue temperature with exposure time for single frequency and dual-frequency (950 kHz and 1.5 MHz) tests under 15 W total input power, and 5 mm depth below the tissue surface.	72
Figure 3-16. Measured change in chicken tissue temperature with exposure time for single-frequency and dual-frequency (950 kHz and 3.3 MHz) tests under 15 W total input power, and 5 mm depth below the tissue surface.	73
Figure 3-17. Measured change in chicken tissue temperature with exposure time for single-frequency and dual-frequency (1.5 MHz and 3.3 MHz) tests under 15 W total input power, and 5 mm depth below the tissue surface.	73
Figure 3-18. Measured change in chicken tissue temperature with exposure time for single-frequency and tri-frequency tests under 15 W total input power, and 5 mm depth below the tissue surface.	74
Figure 3-19. Measured change in chicken tissue temperature with exposure time for dual-	

frequency and tri-frequency tests under 15 W total input power, and 5 mm depth below the tissue surface.	75
Figure 3-20. Temperature vs. imaging luminance in T1-MPRage mode on gelatin phantom.	77
Figure 3-21. MR imaging of the phantom before and after HIFU exposure. The target areas of HIFU transducer are shown in the red circle (a) before ultrasonic exposure; (b) after 25 W single-frequency (1.5 MHz) exposure; and (c) after 25 W dual-frequency (1.5 MHz:3 MHz = 5:1) exposure.	78
Figure 3-22. Temperature rises in single- and dual-frequency tests. The amplitude ratio shown is 1.5 MHz:3 MHz.	79
Figure 4-1. Non-inertial and inertial acoustic cavitation.	85
Figure 4-2. Schematic diagram of the experimental setup for cavitation detection by a 10 MHz receiving transducer.	93
Figure 4-3. (a) Input pressure function used by Church [151]. (b) The pressure pulse as a function of time with the function in Church's paper. (c) The bubble dynamics modeling results in Church's paper. (d) Normalized bubble radius is plotted against normalized time, which corresponds to Fig. 47(a).	95
Figure 4-4. The pressure vs. time graph for the input acoustic excitation.	96
Figure 4-5. Bubble dynamics modeling shows the bubble diameter vs. time during 10- μ s excitations (a) under a 1.5 MHz ultrasonic excitation. (b) under a 3 MHz excitation. (c) under a dual-frequency (amplitude ratio of 3 MHz : 1.5 MHz is 1:5) excitation.	98
Figure 4-6. The generated cavitation pressure during the 10-ms bubble oscillation from the radiated pressure modeling. (a) in response to 1.5 MHz ultrasonic excitation. (b) in response	

to 3 MHz excitation. (c) in response to dual-frequency excitation (amplitude ratio of 3 MHz : 1.5 MHz is 1:5) excitation	99
Figure 4-7. The calculated root-mean-square radiated pressure under different ultrasound sonications (the amplitude ratio shown is the value of 1.5 MHz : 3 MHz).	100
Figure 4-8. The calculated root-mean-square radiated pressure under ultrasound sonications with different acoustic pressure (the presentage shown is the amplitude rate of 3 MHz). ...	101
Figure 4-9. PCD signals from single-frequency ultrasound and dual-frequency ultrasound at 5 second after starting the ultrasound exposure.	103
Figure 4-10. Frequency spectrum of single- and dual-frequency ultrasound. (a) single-frequency case with 1.5 MHz under 25 W acoustic power. (b) dual-frequency case with the amplitude rate of 1.5 MHz:3 MHz = 5:1 under 25 W.....	104

CHAPTER 1 Introduction

1.1 High power ultrasound

1.1.1 Ultrasound

Acoustics, the science of sound, starts as far back as Pythagoras in the 6th century BC, who wrote on the mathematical properties of stringed instruments. Echolocation in bats was discovered by Lazzaro Spallanzani in 1794, when he demonstrated that bats hunted and navigated by inaudible sound but not vision. The piezoelectric effect, discovered by Jacques and Pierre Curie in 1880, was instrumental in the creation and detection of ultrasonic waves. After the discovery of the piezoelectric effect, and subsequent development and research, transducers could be used to generate and detect ultrasonic waves in air and water. Francis Galton constructed a whistle producing ultrasound in 1893, and the first technological application of ultrasound was an attempt to detect submarines by Paul Langevin in 1917 [1].

In acoustics, people from both academics and industry have drawn a lot of interest in ultrasonics. Ultrasound is an oscillating sound pressure wave with a frequency greater than the upper limit of the human hearing range. Ultrasound is thus only separated from audible sound by the fact that humans cannot hear it, and not based on differences in physical properties. Although this limit varies from person to person, it is approximately 20 kHz in healthy, young adults. Ultrasound devices operate with frequencies from 20 kHz up to several GHz (Fig. 1-1).

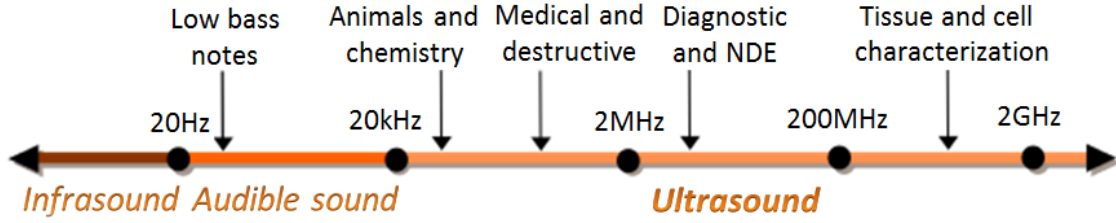


Figure 1-1. Approximate frequency ranges corresponding to ultrasound, with general guide of some applications [1].

To describe an ultrasound wave, considering a half-space filled with liquid or soft-tissue, and in most cases, the soft tissue may be considered as liquid-like medium. At $x = 0$ (Fig. 1-2), it is assumed that there is a thin solid-plane with lateral dimensions much greater than the wavelength (λ) of the sound wave. With a sound source located at this plane, its vibration leads to the generation of a sound wave in the region at $x > 0$. The displacement of this source plane with respect to $x = 0$ can be written as

$$x(t) = A \cos(2\pi ft + \phi_0), \quad (1)$$

where t is the time, f is the frequency of the vibration, A is the amplitude, and ϕ_0 is the initial phase, which determines the initial condition. The pressure in the medium caused by this vibration is a function of x and t and fluctuates around the equilibrium pressure. If we define the acoustic pressure $p(x,t)$ as the excess of the total pressure to the equilibrium pressure, it can be written as

$$p(x,t) = P_0(x) \cos(kx - \omega t), \quad (2)$$

where $P_0(x)$ is the acoustic pressure amplitude, which is a function of position x related with the attenuation coefficient of the medium α

$$P_0(x) = P(0) \cdot 10^{\frac{\alpha \cdot x \cdot f}{20}}, \quad (3)$$

Other parameters include the angular frequency $\omega = 2\pi f$, the wave number $k = 2\pi/\lambda$. In water, the attenuation coefficient is often negligible. Frequency and wavelength are dependent for a sound wave; they are related by the relationship of $f\lambda = c$, where c is the phase velocity and the wavefront $x_0 = ct$. As an example, in water or soft-tissue, the phase velocity at 20 °C is approximately 1500 m/s.

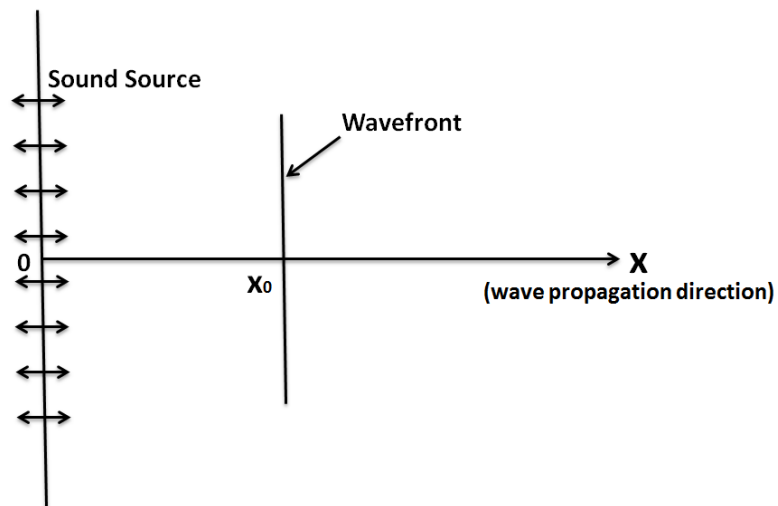


Figure 1-2. A plane-wave sound source and its wavefront.

Ultrasound is used in many different fields (Fig. 1-3), many of which take advantage of the ability to detect objects and measure distances using ultrasonic waves. Ultrasonic imaging is used in both veterinary medicine and human medicine; in the nondestructive testing of products and structures, ultrasound is used to detect invisible flaws such as cracks and material irregularities; ultrasound is also used for cleaning and for mixing, and to accelerate chemical processes. At higher power levels, ultrasonics is useful for therapy, micro-particle manipulation or changing the chemical properties of substances [2] [3].

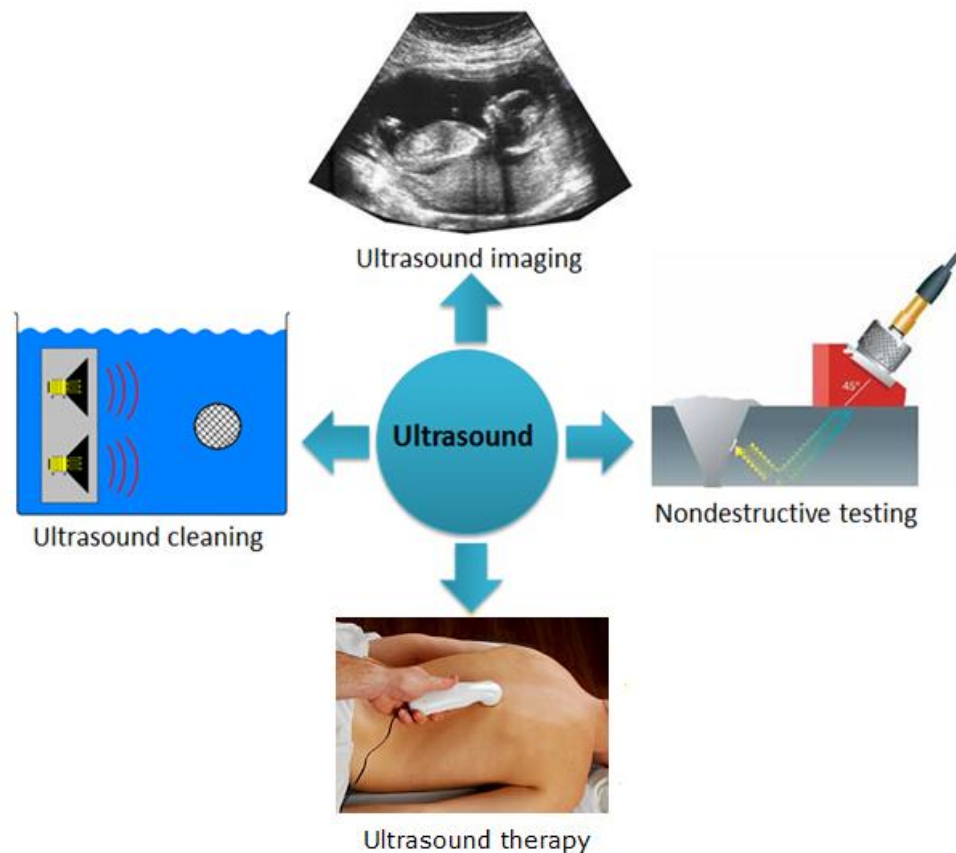


Figure 1-3. Examples of ultrasound applications.

1.1.2 High intensity focused ultrasound (HIFU)

High-intensity focused ultrasound is often considered a promising technology within the non-invasive or minimally invasive therapy segments of medical technology. HIFU's capacity to generate in-depth precise tissue necrosis using an external applicator, with no effect on the surrounding structures, is unique. The history of using therapeutic ultrasound dates back to early in the 20th century. Technology has continually improved and additional clinical applications, both diagnostic and therapeutic, have become an integral part of medicine today. Simple focusing can be achieved either by a spherical-shaped concave transducer or by using an acoustic focusing lens. High-power applications of ultrasound often use frequencies between 20 kHz and a few MHz. Intensities can be very high, above 10 watts per square centimeter. This high intensity can induce cavitation in liquid media, with some applications using up to 1000 watts per square centimeter.

Ultrasound intensity is defined as the power transferred per unit area, which is also related with the acoustic pressure and medium property

$$I = \frac{\text{Power}}{A} = \frac{\text{Pressure}^2}{2\rho c}, \quad (4)$$

where A is the area of the focal beam, ρ is the density of the medium. Here the pressure is the peak-to-peak pressure value. To understand the meaning of the intensity of ultrasound, we can recall that an oscillating source of ultrasound in contact with tissue transfer its mechanical energy to the particle of the tissue medium, causing them to vibrate. The medium

particles then possess energy by virtue of their motion. Intensity is a measure of this energy. It represents the feature of mechanical vibrations of the medium particles. Different physical parameters may be used to express this feature. These include particle velocity, particle acceleration and particle pressure. Each of these parameters varies in time and in space within the medium, and so does the intensity. Intensity may be expressed either as an absolute measurement, or using a relative scale. Knowledge of the absolute intensity of ultrasound is required in HIFU applications. The output intensity of an ultrasound transducer affects its sensitivity. As an example, when we wish to assess the potential biological consequences of the exposure to ultrasonic energy, we must know the amounts of energy actually dissipated in tissue.

As an example, a theoretical model will be discussed here and shown in Fig. 1-4. This type of focused transducer usually consists of a piezoelectric ceramic component whose front surface is nearly of spherical shape with the radius A . The geometrical center of the sphere is at C .

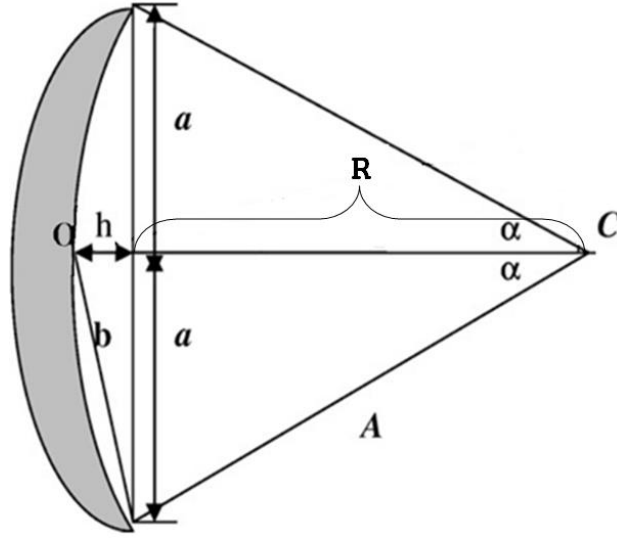


Figure 1-4. Illustration of a focused ultrasound transducer.

The dimensions of the curved front surface can be described as:

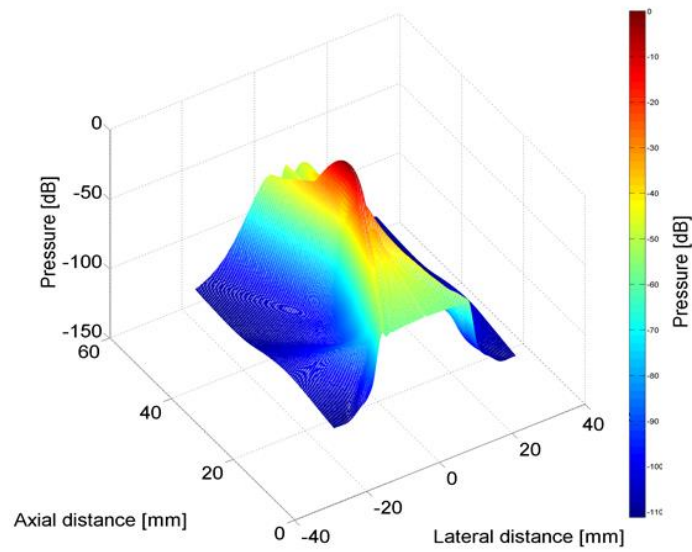
$$a = A \sin \alpha, h = A(1 - \cos \alpha), b^2 = a^2 + h^2, A = R + h$$

$$f\text{-number} = R/2a = 1/(2 \sin \alpha), \quad (5)$$

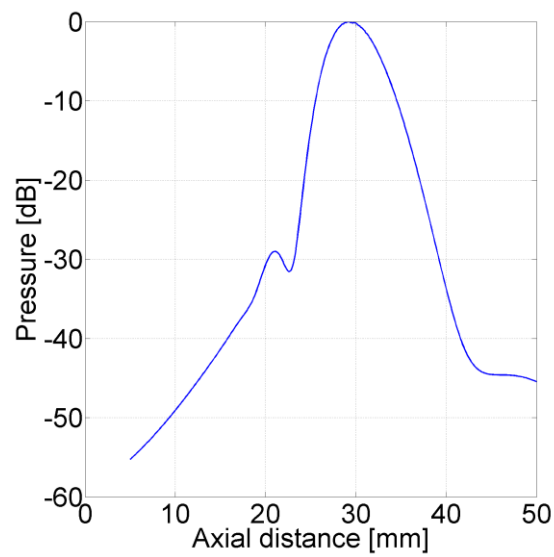
where R is called the focal length of a ultrasound transducer, h is called the depth of the concave surface, f -number is defined as the ratio of the focal length to the diameter of the spherical transducer.

It has been mathematically demonstrated by O'Neil [6] that the greatest intensity (the physical focus) takes place near C (the geometrical focus) but not exactly at C . The magnitude of focusing, expressed by the ratio of the intensity at C to the average intensity at the radiating surface, is equal to $2\pi h/\lambda^2$. In other words, increasing this ratio or equivalently

decreasing f-number increases the sharpness of the focusing. Furthermore, this also decreases the distance between the physical focus and the geometrical focus at C. The plane that contains C and is normal to the axis of the sound field is called the focal plane. To describe the directivity of the focused ultrasound field; we use the z direction as the direction of the wave propagation and the x-y plane is perpendicular to z direction. Fig. 1-5 shows an example of the acoustic pressure distribution vs. axial and lateral distances for a 1.5 MHz HIFU transducer. The simulation results are generated using Field II [4], which is a Matlab toolbox (MathWorks, MI, USA). Input parameters of this transducer are 30 mm-focal length and 29 mm-diameter aperture. This type of ultrasound transducers is also called piston transducers.



(a)



(b)

Figure 1-5. The acoustic pressure distribution for a 1.5 MHz ultrasound transducer. The axial direction is the acoustic emitting direction. (a) 2D pressure distribution along the axial and lateral directions. (b) pressure distribution along the acoustic axis.

A change of relative pressure by 6 dB is of special significance. For every 6 dB change, there is a change in absolute pressure by a factor of two. The area with the relative pressure above 6 dB is called the focal area of an ultrasound transducer.

1.2 High intensity ultrasound applications

High-intensity focused ultrasound has been demonstrated as a precise medical procedure (Fig. 1-6). Focused high intensity ultrasound pulses can be used to break calculi such as kidney stones and gallstones into fragments small enough to be passed from the body without undue difficulty, a process known as lithotripsy [5]. High intensity ultrasound has also been used to trigger the release of anti-cancer drugs from delivery vectors including liposomes, polymeric microspheres and self-assembled polymeric [6]. Another important application is that ultrasound can ablate tumors or other tissue non-invasively, which is widely used for tumor treatment. This technique is called focused ultrasound surgery (FUS surgery). This procedure uses generally lower frequencies than medical diagnostic ultrasound (250–2000 kHz), but significantly higher time-averaged intensities (up to 1000 watts per square centimeter). The treatment is often guided by Magnetic Resonance Imaging (MRI); the combination is referred to as Magnetic resonance-guided focused ultrasound (MRgFUS) [7] [8]. Delivering chemotherapy to brain cancer cells and various drugs to other tissues is called acoustic targeted drug delivery (ATDD). These procedures generally use high frequency ultrasound (1–10 MHz) at a range of intensities (0–20 W/cm²). The acoustic energy is focused on the tissue of interest to agitate its matrix and make it more permeable for therapeutic drugs [9] [10]. Furthermore, researchers have successfully used ultrasound to

regenerate dental material [11], to treat eataract by phacoemulsification [12], to enable non-invasive delivery of epirubicin across the blood–brain barrier in mouse models [13]. High-intensity ultrasound is being tested for use in aiding tissue plasminogen activator treatment in stroke sufferers in the procedure called ultrasound-enhanced systemic thrombolysis [14].

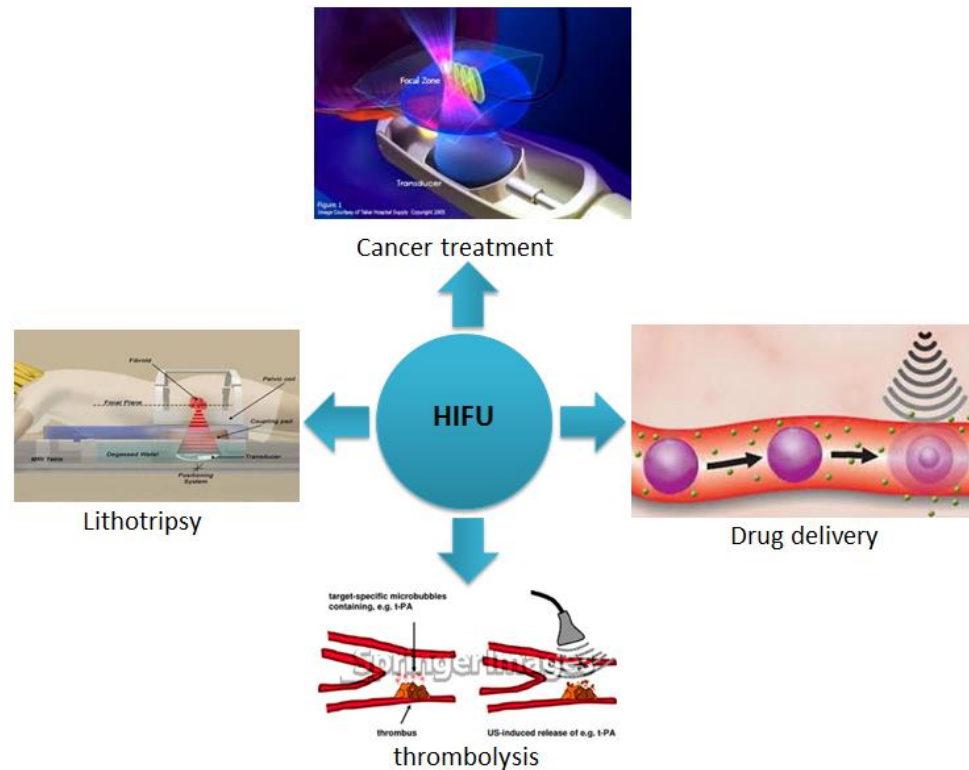


Figure 1-6. Examples for high-intensity focused ultrasound applications.

To understand high-intensity ultrasound in the numerous applications, three major characteristics have been discussed in recent years. The first characteristic of high-intensity ultrasound is thermal effects, which has been described in the definition of ultrasound intensity as the absorption process:

$$q = \alpha \cdot I, \quad (6)$$

where q is the thermal source generated by the absorption of ultrasound. Intense acoustic energy is delivered to a small region of tissue, where the absorption process increases the tissue temperature to a relatively high value and causes thermal coagulation and ablation of cells [15]. Homeostatic mechanisms will tend to counteract the rise in temperature of tissues exposed to heating. The success of homeostasis in restoring normal temperature depends on the balance between heat gain and heat loss. Any alteration in temperature automatically initiates a reaction in an effort to restore normal temperature. However, it is apparent that homeostatic control was unable to prevent the rise in tissue temperature recorded by Draper and colleagues [16]. This is because that those local and general homeostatic mechanisms are only partially successful in quickly reversing the effect of a rise in temperature. The resultant tissue temperature following heating primarily depends on the extent of conduction into surrounding tissues and dissipation by blood perfusion. Dissipation by blood perfusion is highly variable and difficult to estimate, but is known to be poor in fatty tissue and tendon [17].

Second characteristic of high-intensity ultrasound is based on acoustic radiation force, a physical phenomenon resulting from the interaction of an acoustic wave with the media. Generally, the force exerted on the obstacle is evaluated by integrating the acoustic radiation pressure (due to the presence of the ultrasonic wave) over its time-varying surface (Fig. 1-7). In attenuative media, attenuation includes both scattering and absorption of the acoustic wave.

In this case, the induced pressure gradient will generate radiation force. The magnitude of the force (F) exerted by an acoustic plane wave at any given location can be calculated as:

$$F = 2\alpha I/c. \quad (7)$$

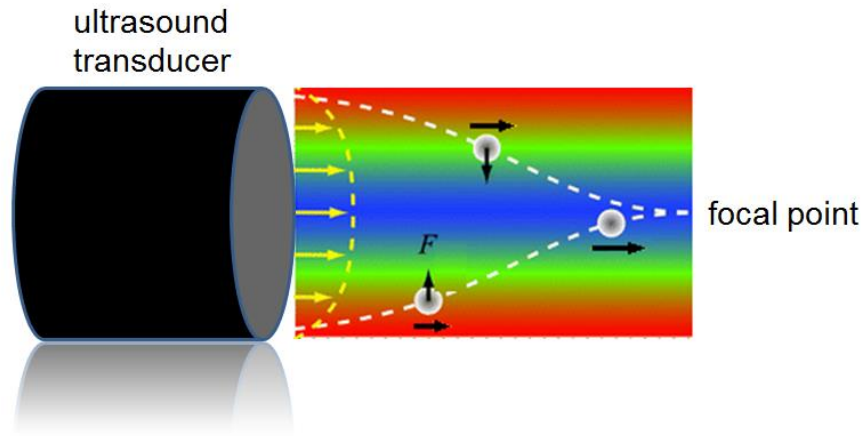


Figure 1-7. Particles within acoustic field will be forced from higher-intensity area to lower-intensity area in the parallel plane of the ultrasound surface, and spontaneously forced along the acoustic transmitting direction by acoustic radiation force.

The third characteristic is cavitation. Cavitation is a process in which mechanical activation destroys the attractive forces of molecules in the liquid phase. Cavitation is usually divided into two classes of behavior: inertial (or transient) cavitation and non-inertial (or stable) cavitation (Fig. 1-8). Microscopic gas bubbles that are generally present in a liquid will be forced to oscillate (non-inertial cavitation) due to an applied acoustic field. If the acoustic intensity is sufficiently high, the bubbles will first grow in size and then rapidly

collapse (inertial cavitation). When these bubbles collapse, it is accompanied by the release of a high concentration of energy which results in high local acoustic pressure and the propagation of shock waves [18]. High-power ultrasound usually utilize the inertial cavitation of microscopic vacuum bubbles for treatment of solid surfaces, liquids, and slurries [19]. More details of these characteristics on different applications will be discussed in the next three chapters.

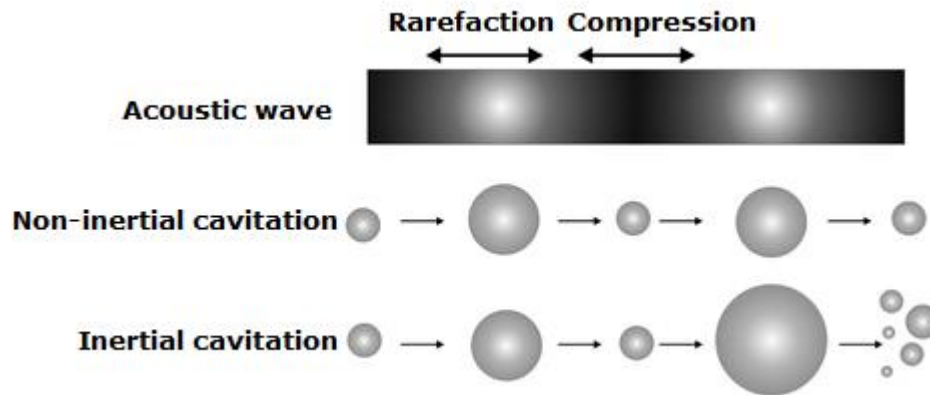


Figure 1-8. The use of ultrasound provides specific activation based on a physical phenomenon: acoustic cavitation [20].

1.2.1 High power ultrasound for thermal ablation

High intensity focused ultrasound (HIFU) is being used today primarily to thermally ablate tissue, where the rate of energy deposition in the tissues produces heat faster than that dissipated. As a result, temperature rise in the exposed tissue can cause thermal ablation of cells [21]. Pulsed-HIFU exposures, however, using low duty, generate energy deposition rates low enough that temperature elevations are well below the threshold for thermal

damage in the tissues [22]. The effects of pulsed-HIFU are more mechanical in nature, such as the creation of acoustic radiation forces. These forces, if high enough, can produce local displacements on the order of cellular dimensions [23] [24]. It has been suggested that repetitive displacements are capable of inducing structural alterations in the tissue, through the creation of locally induced strain. The strain results from shear forces produced between adjacent regions of tissue experiencing non-uniform displacement, and the alterations (i.e. widening of intercellular spaces between both endothelial and parenchymal cells) may increase the tissue's permeability [25]. The ultrasound technology employed for directly inducing thrombolysis has involved procedures that are either invasive (e.g. via catheter based techniques) [26] or rely on ultrasound mechanisms such as acoustic cavitation [27], which is potentially damaging to surrounding tissues [28]. Ultrasound has also been combined with thrombolytic agents in in vitro and in vivo models with improved rates of thrombolysis [29].

1.2.2 High power ultrasound for cell sorting

Focused ultrasonic manipulation has emerged as a simple and powerful tool for trapping, aggregation, and separation of cells. During the last decade, an increasing amount of applications in the microscale format has been demonstrated, of which the most important is acoustophoresis (continuous acoustic cell or particle separation). Traditionally, the technology has proven to be suitable for treatment of high-density cell and particle suspensions, where large cell and particle numbers are handled simultaneously.

Methods for manipulating single cells date back to the early twentieth century when Barber demonstrated how to grasp a cell with suction through a hollow glass micropipette tip [30]. In comparison to electrical or optical cell manipulation, ultrasonic manipulation is generally not associated with the high spatial accuracy needed for single-cell handling. Instead, ultrasound is known as an efficient tool for, e.g., high-throughput cell separation (“acoustophoresis”) [31] or cell aggregation in mL-volume cell suspensions [32] capable of simultaneous handling of cell numbers ranging from thousands to several millions. Nevertheless, ultrasound has recently been demonstrated to be capable of cell manipulation approaching the single-cell level [33] [34].

1.3 Objectives

High-power ultrasound has been proven to have potential in many applications in medicine and biology, and many existing problems and challenges need to be addressed to advance high power ultrasound technology in medicine and biology. The objectives of this research are: 1) enhance tissue ablation efficiency for more power efficient HIFU therapies; 2) explore new high power ultrasound applications in biology. In order to achieve these objectives, several tasks were designed and executed during the past 4 years, and the background, design method and materials, experimental results and conclusions for each task were summarized in the following three chapters.

In Chapter 2, the use of ultrasonic waves to release pellets for isolation of adherent live cells was investigated with high cell survivability. This technique has the potential for use in high-throughput cell sorting. To approach this goal, modeling on possible mechanisms for

ultrasound-based cell sorting was firstly performed, followed by pallet release tests using ultrasound on different pallet samples for feasibility demonstration of this technology. Finally, the tests of live cell release with pallet samples were performed.

In Chapter 3, the combination of modeling and experiments was employed to understand the physics behind the differences in tissue ablation behavior between single- and multi-frequency ultrasound. In specific, we firstly simulated the nonlinear acoustic pressure field of the dual-frequency ultrasound for two different transducer positioning configurations. Temperature rise expected from thermoviscous heating was also calculated for both single- and dual-frequency ultrasound excitations based on a linear acoustic approximation. Experimental results of single- and multi-frequency HIFU for tissue ablation are shown in the form of recorded temperature by both thermocouples and MRI (magnetic resonance imaging), and the possible attribution of accelerated heating by multi-frequency ultrasound is discussed and verified by positive cavitation detection tests and cavitation bubble modeling.

In Chapter 4, the enhanced effect of dual-frequency ultrasonic irradiation on cavitation yield is reported, for the first time, via the cavitation bubble modeling. The cavitation yield was characterized using the PCD (passive cavitation detection) method. Two-frequency (1.5 MHz/3 MHz) orthogonal pulse ultrasound has been used in the tests. It was found that the combined irradiation of dual frequency ultrasound can produce a significant increase in cavitation yield compared with single frequency irradiation. The possible mechanisms of the enhanced effect were briefly discussed and explained by the single-bubble cavitation model, where the calculated radiated pressure generated by acoustic bubble cavitation was found to be greater in dual-frequency cases.

Finally, in Chapter 5, the results obtained in the chapter 2, 3 and 4 are summarized. The remaining challenges and application potential of these high-intensity ultrasound techniques are also discussed.

CHAPTER 2 Ultrasonic cell sorting

2.1 Background

2.1.1 Cell sorting

Separation of selected cells from a mixed population is an important process in many biomedical research areas including genetic engineering, stem cell research and regenerative medicine. For example, to study the function of individual genes and proteins, genetically engineered cells must first be isolated from a mixed cell sample additionally. Cell sorting is applicable in stem cell research since undifferentiated stem cells must be selected from a group that contains more differentiated cells. Finally, to develop human cell lines for personalized medicine, isolation and cloning of desirable cells from a patient's biopsy is required [35]-[37].

There are two basic systems for growing cells in culture, as monolayers on an artificial substrate (i.e., adherent culture) or free-floating in the culture medium (suspension culture). Many cell types, in particular many microorganisms, grow in solution and not attached to a surface. These cell types can be subcultured by simply taking a small volume of the parent culture and diluting it in fresh growth medium. Adherent cells, for example many mammalian cell lines, grow attached to a surface such as the bottom of the culture flask. These cell types have to be detached from the surface before they can be subcultured.

A number of technologies have been developed to separate non-adherent cells. Research progress on stem-cell fate determination, molecular markers, signaling pathways and niche interactions in hematopoietic, neuronal and muscle tissue may provide parallel insight into the biology of mammary epithelial stem cells. Taking advantage of approaches similar to

those employed to isolate and characterize hematopoietic and epidermal stem cells, a mammary epithelial cell population with several stem/progenitor cell qualities have been identified [38]. For individual Natural killer (NK) cells, the relationship between the characteristics of these cell–cell interactions, cytolysis, and secretory activity is not well understood. Arrays of subnanoliter wells were used to monitor individual NK cell–target cell interactions and quantify the resulting catalytic and secretory responses. It showed that NK cells operate independently when lysing a single target cell and that lysis is most probable during an NK cell's first encounter with a target [39]. To measure the effects of the interactions between neutrophils and monocytes migrating in response to various chemoattractants, at single-cell resolution, a microfluidic platform that replicates critical features of focal inflammation sites was developed. It was integrated that a lactase assay into the focal chemotactic chambers (FCCs) of the device to distinguish between phlogistic and nonphlogistic cell recruitment [40].

Many methods have been developed to separate non-adherent cells, but the options are very limited when dealing with adherent cells. Traditionally, adherent cells have been detached from their growth surface mechanically or enzymatically, both of which result in cellular perturbations such as loss of morphology [41]-[42], removal of cell surface markers [43] [44], and alterations in cell physiology [45]-[47].

For adherent cells, fluorescence-activated cell sorting and limited dilution with or without antibiotic selection are the two most common methods in use [48]. In fluorescence-activated cell sorting, the cells are rendered differentially fluorescent and incorporated into a small liquid stream illuminated by a laser beam [49]. Integrase-positive bacterial colonies

from the enrichment cultures were then isolated by using hydrophobic grid membrane filters and integrase-specific gene probes. Bacterial clones isolated by this technique were then confirmed to carry integrons by further testing by PCR and DNA sequencing. Rapid and efficient identification, isolation, and characterization of antibiotic resistance-associated integrons are possible by this protocol. However, both of these strategies suffer from a major drawback. In these techniques cells must be detached from their surface during the sorting process, which can lead to programmed cell death, especially if such cells remain in suspension for more than a few minutes [50].

2.1.2 Microarray technologies for adherent sorting

To avoid these perturbations, a platform for manipulating adherent cells without stripping the cells from their growth surfaces would be of great value in the selection of single live adherent cells with their adhesive state preserved [51]-[52]. By using a micro-machined silicon substrate with moving parts, it was demonstrated the dynamic regulation of cell-cell interactions via direct manipulation of adherent cells with micrometer-scale precision. Thereby mechanical control of both tissue composition and spatial organization could be achieved [53]. A self-folding technique using cells is highly biocompatible and does not involve special material requirements for the microplates and hinges to induce folding [54]. In another way, a parylene-C microstencil was used to develop two methods of creating patterned co-cultures using either static or dynamic conditions. In the static case, embryonic stem (ES) cells were co-cultured with fibroblasts or hepatocytes by using the reversible sealing of the stencil on the substrate. In the dynamic case, ES cells were co-cultured with

NIH-3T3 fibroblasts and AML12 hepatocytes sequentially by engineering the surface properties of the stencil [55].

Microarray technologies were developed to isolate adherent cells by using an array of releasable microfabricated elements that are called "pallets" or "rafts" (Fig. 2-1). The pallets can be fabricated from a biocompatible, transparent, 1002F epoxy photoresist on a microscope slide by standard photolithography [56] [57]. These pallets can be varied in size from tens to hundreds of microns to provide an adequate growth area for single cells or colonies. In addition, the pallet surfaces can be chemically modified with polymers or proteins to enhance cell attachment and growth [58]. To select and sort cells using the pallet arrays, cells are initially placed in suspension and allowed to settle and grow on individual pallets of the array, and the targeted cells are released later together with the pallets. Over the last few years, micro-fabricated mobile platforms enable adherent cells to retain their adhesive properties during manipulation. Allbritton's group proposed the use of micro-sized blocks mounted on a glass substrate as a means to separate live adherent cells individually [59] [60]. Micrafts, an array of microwells possessing detachable concave elements, were manufactured using a polydimethylsiloxane (PDMS) mold combined with a dip-coating process. PDMS-based micraft array is more flexible compared with micropallets on glass substrate. Release of pallets by a laser pulse [61] [62] and release of rafts by a microneedle [63] have been investigated for isolation of adherent live cells.

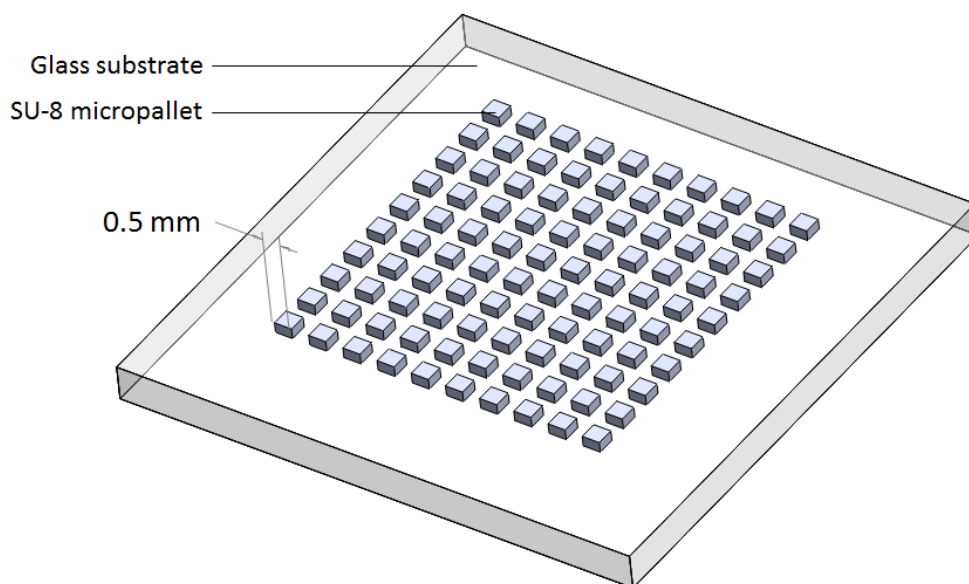


Figure 2-1. Sketch of a 500- μm SU-8 micropallet array on a glass substrate.

The micropallet array system used a pulsed laser to release pallets tens of microns to hundreds of micrometers in size from a larger array, enabling selective isolation of single cells adherent to the pallets (Fig. 2-2). The laser-based release of pallets with respect to pallet array and laser parameters was characterized. The required laser energy for pallet release increases linearly with the area of the single pallet in contact with the glass substrate. The spacing between pallets within an array as well as the thickness and height of the pallets does not affect the energy required to release a pallet. Delivery of multiple laser pulses decreases the energy and pulse number required for pallet release when the pallets were 100 μm or greater on a side. In addition to the square pallets, complex structures such as cantilevers and spirals could also be released without damage using the pulsed laser. Identification of the

pallet-array variables influencing the laser energy as well as strategies to minimize this energy will contribute on optimizing the release of pallets with cells on the arrays [64].

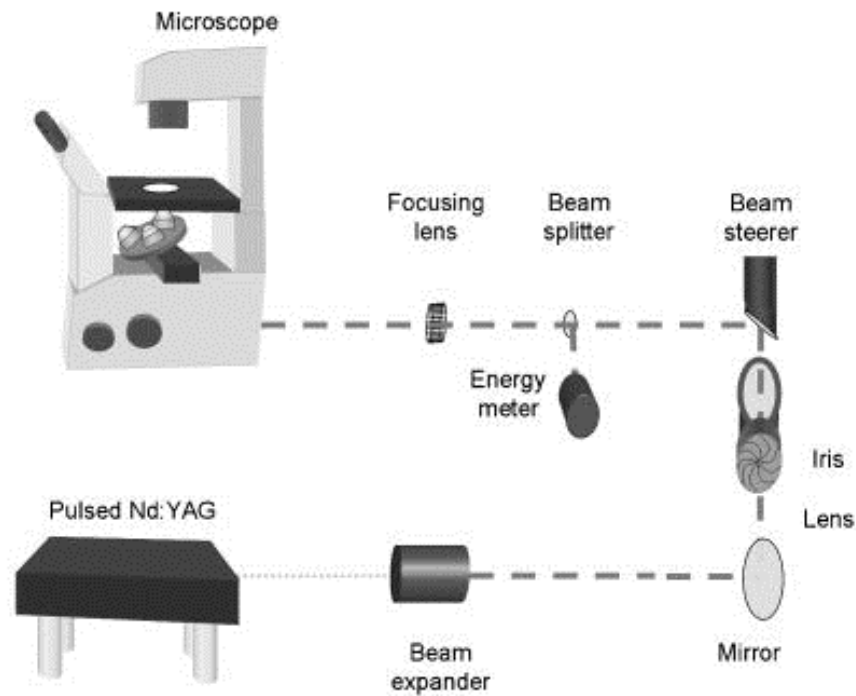


Figure 2-2. Experimental system for laser-based pallet release [64].

Cells plated on the microarray settled at the center of the wells due to the micrafts' concavity. Individual micrafts were readily dislodged by the action of a needle inserted through the compliant polymer substrate. The hard polymer material (polystyrene or epoxy resin) of which the micrafts were composed to protect the cells from damage by the needle. For cell analysis and isolation, cells of interest were identified using a standard inverted microscope and micrafts carrying target cells were dislodged with the needle (Fig. 2-3).

The released cells/micrafts could be efficiently collected, cultured and clonally expanded [65].

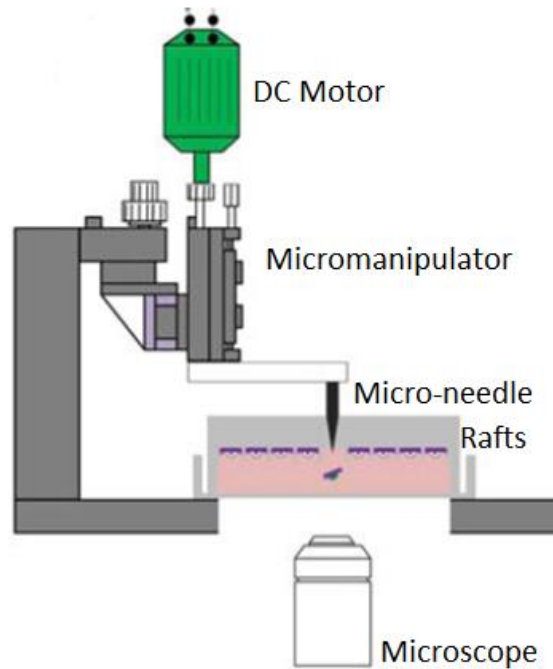


Figure 2-3. Micraft release by a tiny needle [31].

These cell-laden microcarriers have proven beneficial for the separation and collection of various types of specific single adherent cells from a mixed population. However, there is a need to further advance this technology. For example, in pallet release process the laser pulse was unable to detach large micropallets (e.g. $500\text{ }\mu\text{m} \times 500\text{ }\mu\text{m}$) from glass substrates because a high laser energy density is needed, yielding poor cell survival [66]. Furthermore, needle-based mechanical release involved piercing the elastomeric substrate to dislodge the rafts, which may lead to a relatively low releasing rate and cell damages.

2.1.3 Ultrasound for cell manipulation

Focused ultrasonic manipulation has emerged as a simple and powerful tool for trapping, aggregation, and separation of non-adherent cells. During the last decade, an increasing number of microscale applications in cell biology, molecular genetics, biotechnological production, clinical diagnostics and therapeutics have been demonstrated. Traditionally, the technology has proven to be suitable for manipulation of high-density cell and particle suspensions, where large cell and particle numbers are handled simultaneously.

Methods for manipulating single cells date back to the early twentieth century when Barber demonstrated how to grasp a cell with suction through a hollow glass micropipette tip [67]. Today, this method is still the standard technique for handling and manipulation of single cells, although it requires a skillful operator and can easily damage the cell [68]. More recently, methods based on external force fields have emerged as a contactless alternative [69]. In particular in microfluidic devices [70], these techniques provide a simple, powerful, and possibly gentle tool for trapping, aggregation, and alignment of particles or cells [71]. However, in comparison to electrical or optical cell manipulation, ultrasonic manipulation is generally not associated with the high spatial accuracy needed for single-cell handling. Instead, ultrasound is known as an efficient tool for high-throughput cell separation (“acoustophoresis”) [72] or cell aggregation in mL-volume cell suspensions [73]. Using these ultrasonic techniques, it is possible to simultaneously handle cell numbers ranging from thousands to several millions. New state-of-the-art techniques have shown, however, that ultrasound is indeed capable of cell manipulation approaching the single-cell level [74] [75].

An acoustic microfluidic system for miniaturized fluorescence- activated cell sorting (μ FACS) was recently reported [76]. By excitation of a miniaturized piezoelectric transducer at 10 MHz in the microfluidic channel bottom, an acoustic wave is formed in the channel. The acoustic radiation force acting on a density media causes fluidic movement, and the particles or cells on either side of the fluid interface are displaced in a direction perpendicular to the wave direction (Fig. 2-4).

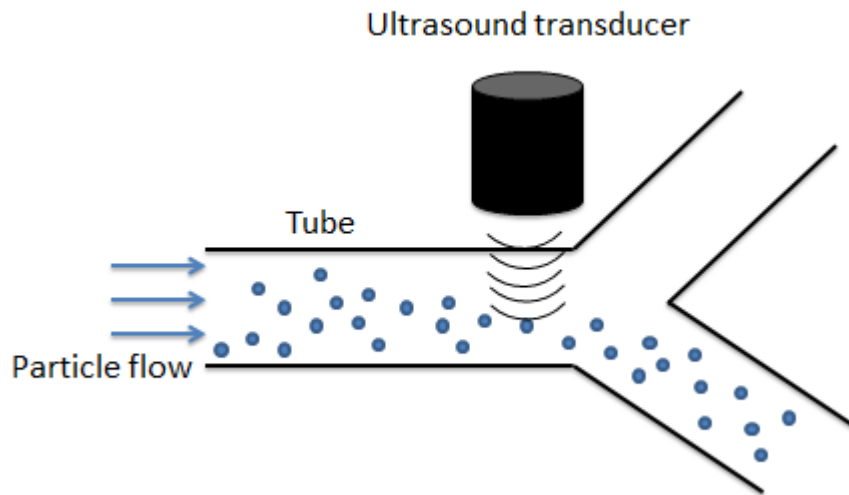


Figure 2-4. A radiation force acting on a density media causes fluidic movement.

A new ultrasonic characterization method of cellular adhesion on substrates was developed in [77]. With this method, longitudinal acoustic waves are applied on cell culture to impose a longitudinal strain on cells. Only the cells subjected to a sufficient level of strain will be detached from the substrate. The idea is to correlate cell detachment rate to the longitudinal strain threshold supported by cells. This global method can be adapted for

different cell types and for different substrates. This method can provide an evaluation of the effect of functionalization on substrates. But the cell viability is always a concern during the cell manipulation, and this method is not selectively.

2.1.4 Motivation and objective

While ultrasound has been demonstrated with promising potential on manipulating individual cells, it has yet to be proven effective in the manipulation of large numbers of adherent cells. To this end, the objective of this work is to investigate the use of ultrasonic waves to release pallets for isolation of adherent live cells with high cell survivability. This technique has the potential for use in high-throughput cell release. To approach this goal, modeling on possible mechanisms for ultrasound-based cell sorting was considered. Initially, the pallet release tests using ultrasound on different pallet samples were done to prove the feasible of this technology, and after all, the tests of live cell release with pallet samples were performed.

2.2 Micro-pallet release modeling

2.2.1 Acoustic radiation force modeling

Acoustic radiation force is one of the important mechanisms of ultrasound. It has been used in global population studies of cells [78] [79]. In this work, ultrasound was used to enable selective release of micropallets with cells, and acoustic radiation force as a possible mechanism in this application is studied. Here, an analytical model for the selective micropallet release using ultrasound is presented. As an ultrasound beam propagates through

an object, acoustic radiation force is transmitted. This force is caused by the acoustic pressure and the momentum transported by the beam [80] [81]. The acoustic radiation force drives objects inside the acoustic field towards the direction of acoustic streaming [82]. In this analytical model, it is assumed that the acoustic radiation force acting on the miropallets is a planar wave propagating along the acoustic axis (Fig. 2-5). This assumption is reasonable because the length of the -6 dB focal zone of the 3.3-MHz transducer is as long as 4.34 mm based on the acoustic field simulation (Fig. 2-6), which is significant thicker than the pallets (a few hundred micrometers).

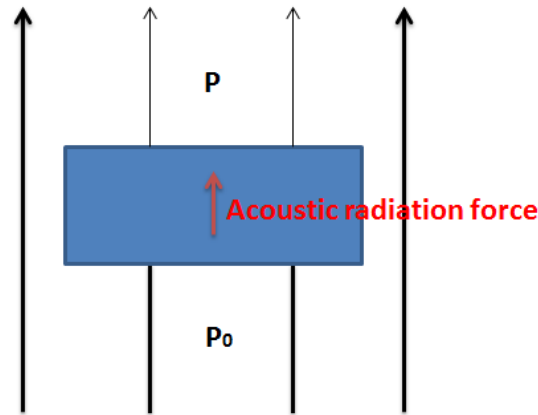


Figure 2-5. Acoustic radiation force on an arbitrary particle generated by a plane wave. P_0 is the acoustic pressure of the plan wave, after the absorption of the particle, the pressure difference cause the acoustic radiation force.

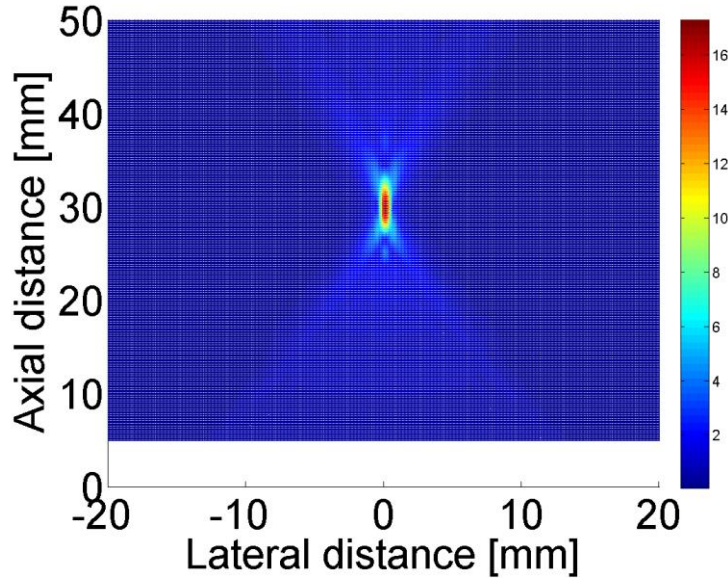


Figure 2-6. Pressure field simulation of the 3.3 MHz transducer used in pallet release tests on 500 μm samples. The output acoustic power is 30 W. (Unit: MPa)

The radiation force is estimated following the formalism derived by Gor'kov [83] [84],

$$F(z) = \frac{\pi}{2\rho_0 c_0^3} \left(f_1 + \frac{3}{2} f_2 \right) \cdot V \cdot p_0^2 \cdot f \cdot \sin \left(2\pi \frac{z}{\gamma_0/2} \right), \quad (8)$$

where z is the distance from the transducer surface along its acoustic axis, f is the frequency, V is the particle volume in the acoustic field, p_0 is the pressure amplitude and γ_0 is the acoustic wavelength in the medium. The dimensionless factors $f_1 = 1 - \frac{\rho_0 c_0^2}{\rho c^2}$ and $f_2 =$

$\frac{2(\rho - \rho_0)}{2\rho + \rho_0}$ are determined by the density and sound velocity of the medium around the pallets

(Fig. 13). It is assumed that the radiation pressure required to release a pallet is the same as the pressure used in our experiments.

2.2.2 Acoustic cavitation modeling

Ultrasound enabled pallet release could also be the result of acoustic cavitation. Since the cell culture medium was not degased and the acoustic pressure in the medium is significant (above 1 MPa) to cause acoustic cavitation (Fig. 2-7), the radiated force generated by cavitation bubble could cause moment of inertia on micropallets. The acoustic cavitation modeling theory is covered in chapter 4.2.

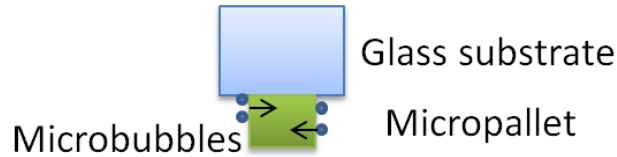


Figure 2-7. Microbubbles generated radiated force (black arrows).

Since radiation force generated by a cavitation bubble could act on any point on the pallet surface, which may cause the rotation of the pallet after release. From a single cavitation bubble, the maximum moment of inertia (I) could be expressed:

$$I_{max} = (RF \cdot W/2)/((WL^4)/12), \quad (9)$$

where W is the thickness of the pallet, and L is the length of a side. From bubble dynamics modeling, the radiated force (RF) generated by cavitation bubbles could be estimated using the generated moment of inertial, which may act on the pallet as shear force.

2.2.3 Attraction force and global force balance

Either acoustic radiation force or microbubbles generated radiated force acts against the attraction force between pallets and the substrate. Once the total external force is larger than the attraction force, the pallet is released. Different theoretical models allow an estimation of the particle adhesion force to the surface resulting from Van der Waals attraction [85]. They all predict that the force F necessary to remove an adsorbed particle from a surface is proportional to its dimension R . For example, the model elaborated by Johnson et al. provides [86]:

$$P = -1.5 w\pi R, \quad (10)$$

where w is the work of adhesion, which is the sum of the surface energy of the two contacting materials minus the interfacial energy. Converting this force into a local pressure P on a square particle gives:

$$P \approx -6w/L, \quad (11)$$

where L is the length of the edge. As we analyzed before, the acoustic radiation force and cavitation generated radiated force could be two primary stresses in the global removal stress.

In order to calculate the attraction force between the micropallets and the substrate, the surface energy and interfacial energy should be estimated. The surface energy density of a solid can be expressed as

$$w \approx TW/2L(W - L), \quad (12)$$

where w the surface energy density of the solid, and T is a constant uniaxial tension. Considering the possible cavitation bubble generated radiation force, the possible final local pressure (P_{total}) can be integrated by:

$$P_{total} = -6W/L - n \cdot I_{max} \cdot (WL^3)/12, \quad (13)$$

where n is the number of cavitation bubbles. In order to remove a particle, the global removal stress must be stronger than the attractive force, in another words, P_{total} is larger than P .

2.3 Experimental method

2.3.1 Micropallet arrays and HeLa cells preparation

Firstly, SU-8 photoresist and developer were used to fabricate SU-8 pallet arrays on glass substrates with four different pallet sizes. The square micropallets in the arrays had the following dimensions: 100 μm side length and 50 μm height, 200 μm side length and 50 μm

height, 200 μm side length and 100 μm in height (Fig. 2-8), and 500 μm side length and 300 μm height. The surfaces of the arrays were modified to cause cell adhesion. Both the pallet array fabrication and surface functionalization of the pallets were performed by Dr. Allbritton's group in the department of chemistry at UNC Chapel Hill.

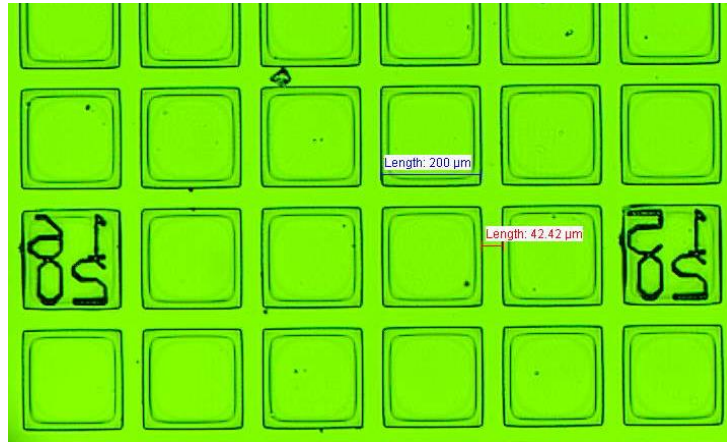


Figure 2-8. Image of SU-8 micropallet array with square pallets having a 200 μm side lengths and 100 μm height taken by a measuring microscope (Olympus STM6, Olympus, Center Valley, PA)

HeLa cells were grown on the array at 37 $^{\circ}\text{C}$ and plated in a volume of 1 mL on each array. Immediately prior to use, the growth media was removed from the cell chamber and replaced with PBS (phosphate buffered saline). The mammalian expression plasmid pegfp-CRKL was transfected into the HeLa cells by electroporation on a gene pulser system.

2.3.2 Experimental setup

A 3.3-MHz ultrasound transducer with a -6dB beam width of 0.51 mm was used to deliver ultrasound waves through the cell substrate. The pallet release process was recorded using a high-speed camera (Phantom 640) which provided 100- μ s-interval resolution for close monitoring of cell release.

To investigate the interaction between the ultrasound waves and microfabricated elements, arrays of pallets were fabricated on glass substrates. The pallet dimensions were 500 μ m \times 500 μ m \times 300 μ m with spacing between two neighboring pallets of 200 μ m. The pallet cassette dish and collection dish were fabricated from polycarbonate by CNC machine, and the micropallets were fabricated on a glass substrate with a thickness of 1 mm. Figure 1 shows the schematic of the experimental setup for pallet release using ultrasound. A 3.3-MHz focused ultrasound transducer was used for pallet release experiments. According to the transducer simulation using Field II [87] (codes in Appendix I), the diameter of a -6 dB focal beam is 0.51 mm. The transducer used has a 29-mm-diameter aperture and 30-mm focal length, and the output power can be adjusted as high as 30 W under a continuous sinusoidal signal. The driving signal was generated from a function generator (AFG3101, Tektronix) and amplified by an RF power amplifier (3700, ENI). The input signal was set to match the center frequency of the transducer. The output acoustic power of the transducer was calibrated using an acoustic power radiation balance (UPM-DT-1AV, Ohmico) under different input electrical powers. To analyze the mechanism of ultrasound-enabled micropallet release, we monitored the process of pallet release at 0.5 ms intervals using a high-speed camera (Fig. 17).

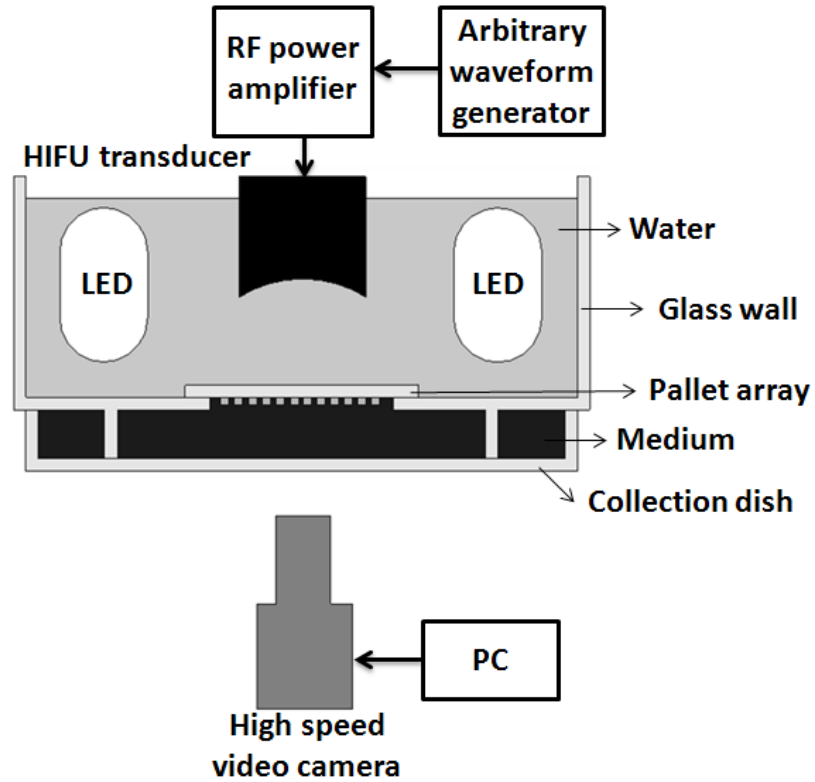


Figure 2-9. Schematic of the experimental setup for pallet release.

For cell release experiments, HeLa cells were grown on the fibronectin-coated pallet array at 37 °C for 24 hours. Two hours prior to the release experiment, HeLa cells were co-stained with 5 μM Calcein acetomethoxy (AM) and 5 μM SYTO 17 (Invitrogen Corporation) for 30 min at 37 °C. SYTO 17, a cell-permeant red fluorescent nucleic acid stain which exhibits bright, red fluorescence upon binding to nucleic acids, was used to facilitate cell counting. Calcein AM is a cell-permeant molecule that is used as a cell-viability indicator. Immediately prior to use, the growth media was removed from the cell chamber and replaced with phosphate buffered saline (PBS). To determine cell viability, released cells co-stained

with calcein AM and SYTO 17 were imaged by a transillumination and fluorescence microscope (Nikon TE200) equipped with FITC and Texas Red filter sets. Viable cells show both calcein AM and SYTO 17 staining, while dead cells show only SYTO 17 staining.

2.4 Results and discussion

2.4.1 Experimental results

We demonstrated, for the first time, that adherent live cells can be safely and rapidly released on pallets using ultrasound waves. Firstly, release experiments on a 200- μm pallet were carried out. The influenced micropallets were observed in each experiment. These observations indicated that in some cases the micropallet was not totally detached, but a position change occurred. Variable power was applied to a variety of pallet sizes for variable duration. The effects of this power application were recorded by a microscope equipped with a digital camera to measure the normalized influenced area of micropallets and obtain the value of threshold power for the release of single micropallet.

No pallet detachment or release was observed on 200- μm -size pallets with 100- μm height under a 60 s application of 10 W input power. When the input power was increased to 15 W, a single pallet was released after 10 seconds, shown in Fig. 2-10(a). Single pallet release also occurred after a 3 second exposure to a 30 W input. The quantity of released pallets increased as the input power and exposure time were increased (Fig. 2-10(b)-(d)).

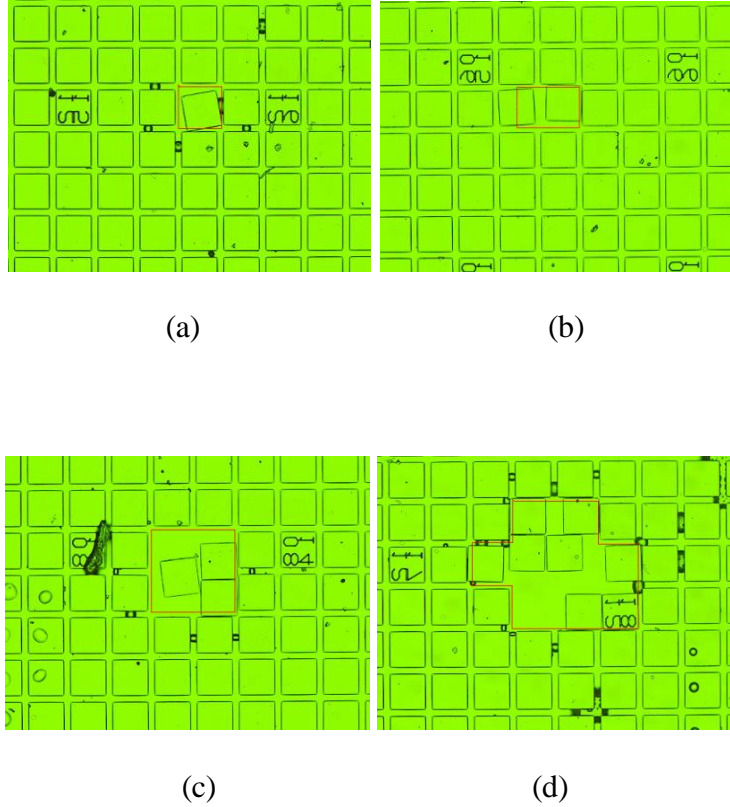


Figure 2-10. (a) Single pallet was released by 15 W input power after 10 seconds. (b) Two pallets were released by 20 W input power after 5 seconds. (c) Four pallets were released by 30 W input power after 5 seconds. (d) Nine pallets were released by 30 W input power after 15 seconds.

Single-pallet release was achieved within short ultrasonic exposure times ranging from 100 ms to 1 s without affecting neighboring pallets. Figures 2-11(a) and (b) show the array of pallets with living cells before and after the single pallet release, respectively. The targeted pallet is indicated by the arrow. To enable cell release, the target pallet was aligned to the acoustic axis of the ultrasound transducer. After the amplified signal to the ultrasound

was triggered on at the output power of 10 W, the selected pallet disappeared in the field of view, indicating a successful release of the pallet. After single-pallet release, the ultrasound had no effect on the surrounding non-targeted pallets and cells.

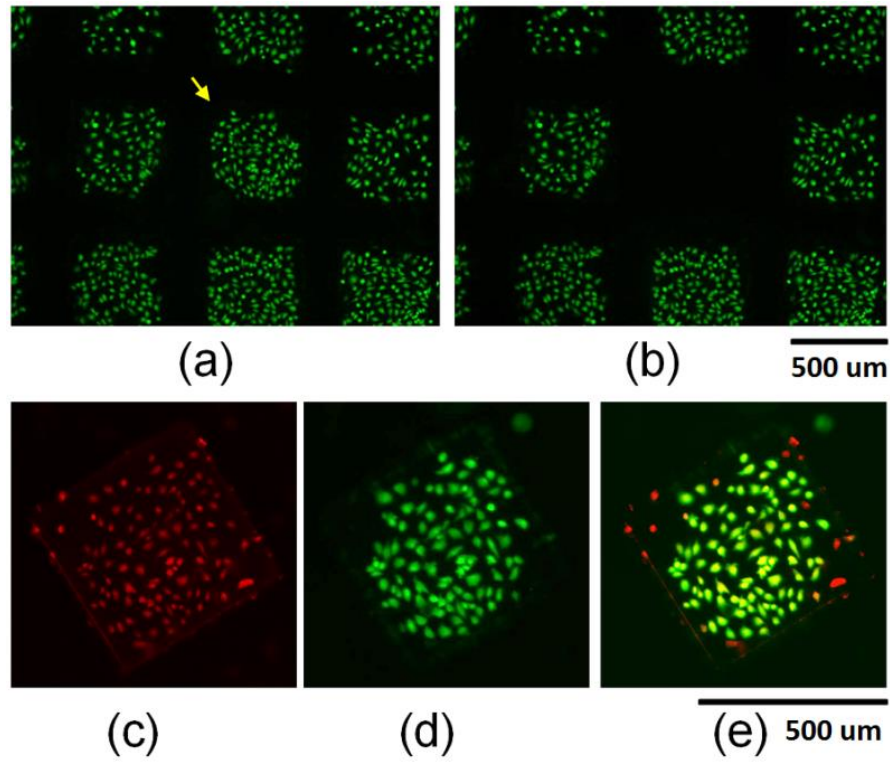


Figure 2-11. Ultrasound induced pallet release with HeLa cells (shown in green). (a)-(b) Selective release of a single 500 μm micropallet with HeLa cells. Pallet array before the single pallet release (arrow points to the pallet to be released) (a), and after released (b). (c)-(e) Collected 500 μm micropallet with HeLa cells. (e) Merged image. 95 cells (stained both green and red) from a total number of 109 were alive. Scale bar = 500 μm .

All released pallets settled down to the collection dish by the force of gravity. The viability of cells attached to targeted pallets after ultrasound release was examined by the fluorescence¹⁴. An Example of a single released pallet with live cells is shown in Figure 2-11(c)-(e), where the pallet had 95 live cells (both green and red colors) and 14 dead cells (red color). 92.2% of the cells remaining on the pallets (number of pallets counted $N = 12$) were found to be viable after release.

According to characterizations of pallet release with different dimensions, 500- μm -size, 300- μm -height pallets with HeLa cells cultured on them were used in these tests. A single large pallet was successfully released within a short ultrasonic exposure time (ms) without affecting neighboring pallets. 92% of the cells remaining on the pallet were still alive after detachment based on six release tests, which is significantly higher than the conventional 30~60% cell viability after fluorescence-activated cell sorting (FACS). Unlike laser-based pallet release [75], no plasma formation was found during the ultrasound-enabled detachment according to the movie recorded by the high-speed camera (Fig. 2-12). It is believed that the pallets were released because of the large-amplitude vibration, together with the ultrasonic radiation force. The releasing velocity of the micropallet was estimated to be less than 1 m/s. This relatively smooth separation contributes to the resulted high survivability of cells.

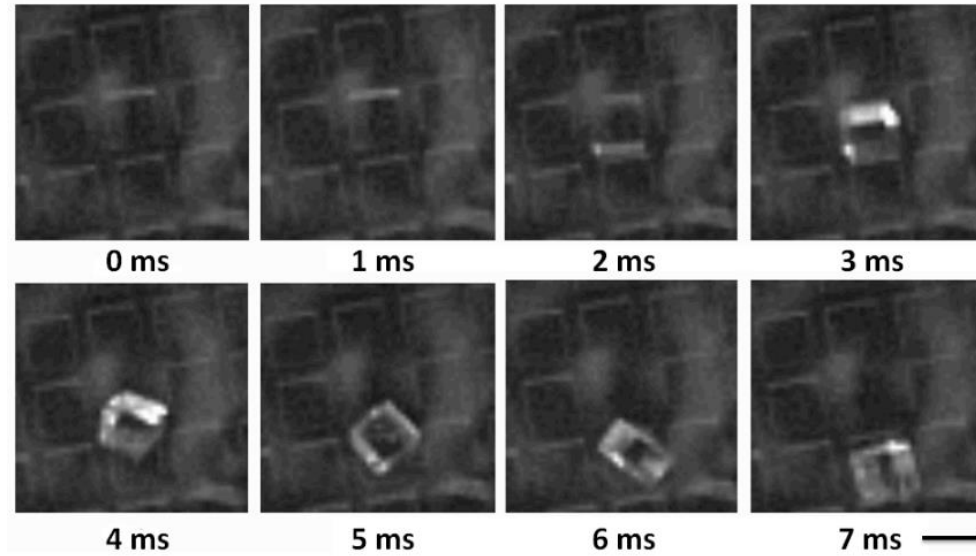


Figure 2-12. Photograph pictures from a movie (7 ms) of pallet release process recorded using a high-speed camera. Scale bar = 500 μm .

Unlike laser-based pallet release [76], no plasma formation was identified during the ultrasound-enabled detachment as observed from the images recorded by the high-speed camera. The releasing velocity of the micropallet was estimated to be 0.5 m/s, considering the length of the focal zone of the high-speed camera and the time needed for the released pallet passing the focal zone. This relatively smooth separation, compared to the release speed of 45~60 m/s in laser-based pallet release, may contribute to the high viability of cells after ultrasonic pallet release. Rotation of the pallets after detachment was observed similar to that found in laser-based pallet release [88].

2.4.2 Modeling results and discussion

Based on those assumptions, the radiation force acting on the 500 μm -size, 300 μm -height pallet at 10 W output power of the transducer is calculated to be 14.9 μN , which has been proved to be safe for HeLa cells attaching on those pallets according to the experimental results. For transducers with similar F-number (e.g. 1.034 which is same as the 3.3 MHz transducer used in the tests), the relationship between the working frequency and -6 dB beam width can be simulated as shown in Fig. 4. Assume that the radiation pressure required to release a pallet is the same ($14.9\mu\text{N}/(\pi \times (0.25\text{mm})^2)$) as the one found in our experiments, the size of a pallet that can be released is similar to the -6dB beam size, and can be estimated as a function of ultrasound frequency (Fig. 2-13). One can find that pallets with larger culture surface require lower-frequency ultrasound, while high frequency ultrasound may be used for micro-pallet release. Pallet height and the total -6 dB beam length may also be considered in ultrasonic pallet release. However, the -6 dB beam length is approximately reciprocal to the working frequency of the ultrasound transducer while the working frequency is higher than 1 MHz according to the simulation results. In this case, while a transducer with high working frequency is designed for micro-pallet release, its -6 dB beam length is 7~8 times larger than the pallet size, which should satisfy the aspect ratio of the pallet dimensions to maximize the radiation force. From equation (8), while the acoustic pressure and frequency is confirmed, the radiation pressure is only related with the height of pallets, which means higher pallet will always help this release process. For example, the radiation pressure under 1 MPa, 3.3 MHz ultrasound wave is calculated (Table. 2-1).

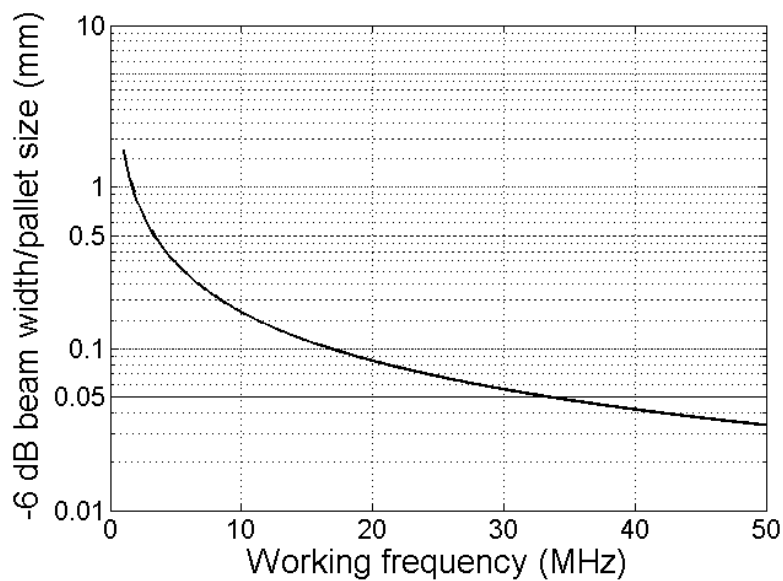


Figure 2-13. The relationship between working frequency and -6 dB ultrasonic beam width at fixed F number (Focal length = 30 mm, diameter of aperture = 29 mm).

Table 2-1. Acoustic radiation pressure under 1 MPa, 3.3 MHz ultrasound wave.

Pallet height	Radiation force
110 μm	0.57 kPa
220 μm	1.26 kPa
300 μm	1.72 kPa

Cavitation bubbles induced by high frequency pressure (sound) waves to agitate a liquid could be generated during high intensity ultrasound exposure. The agitation produces high

forces on contaminants adhering to substrates like metals, plastics, glass, rubber, and ceramics. The intention is to thoroughly remove all traces of contamination tightly adhering or embedded onto solid surfaces. The acoustic pressure around the pallets is above 1 MPa measured by a hydrophone. This pressure value is used as an input for the bubble dynamics modeling. As the result shown in Fig. 2-14, the radiated peak pressure is 300~400 kPa, which may generate considerable shear force during pallet release.

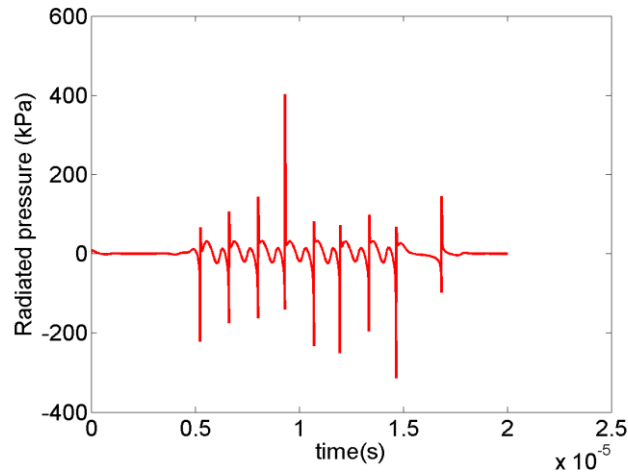


Figure 2-14. Acoustic cavitation modeling. The radiated pressure is calculated under 1 MPa, 3.3 MHz ultrasonic sonication.

In equation (12), T is a constant uniaxial tension which is measured by a force balance as about 0.46×10^{-3} N, W is the thickness of the glass substrate (1 mm)/pallet (300 μm), L is the length of the edge (500 μm). Interfacial energy is assumed to be zero because there isn't any other particle between the substrate and the pallet. In this case, the total γ is calculated to be 0.23×10^{-3} N/mm, and the attraction pressure is 1.41 kPa, which is smaller than the

calculated acoustic radiation force (1.72 kPa) on 300 μm -thick pallets. Here the radiated force generated by cavitation bubble is not integrated because the number of cavitation bubbles is difficult to be estimated. With the possible involved cavitation induced radiated pressure, the global force could be stronger than the attraction force, which leads to the pallet release.

2.5 Summary

In summary, ultrasound-enabled microfabricated pallet release with adherent cells has been demonstrated. This highly selective pallet/cell release method yields significantly higher cell viability after single-pallet release, comparing with other existing methods, largely resulting from the relatively slow release speed and low radiation forces. The mechanisms behind the ultrasound-induced pallet release are considered: acoustic radiation force and acoustic cavitation. The parameters of the ultrasound transducer are optimized based on different pallet samples, and also the design of the microarray is proposed to reduce the required release energy. The demonstrated selection, separation, and collection of specific cells from a mixed cell population using the ultrasonic method holds great potential for biomedical research, including genetic cell engineering and stem cell engineering toward new drug discovery and therapy exploration.

CHAPTER 3 Tissue ablation using multi-frequency ultrasound

3.1 Background

3.1.1 Tissue ablation using high-intensity focused ultrasound (HIFU)

Scientific studies involving high-intensity focused ultrasound (HIFU) as a possible therapy option for several types of tumors have been published for about half a century (Fig. 3-1). Ultrasound has the potential to provide a truly non-invasive target treatment option, which is not limited to the direct treatment of cancers, but may also be used in palliative setting for relief of chronic pain of malignant origin, for hemostasis, or even for the treatment of cardiac conduction or congenital anomalies [89].

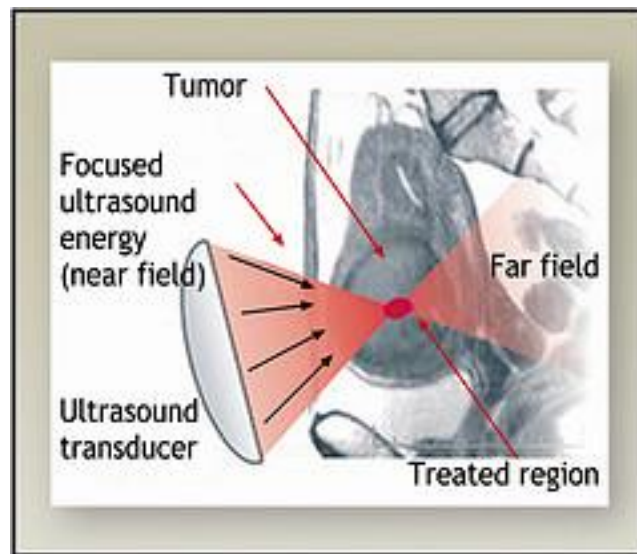


Figure 3-1. Focused ultrasound on tumor treatment [89].

Mechanisms of HIFU-induced tissue ablation

The thermal effects of HIFU in cancer treatments have been widely studied. The first mechanism behind the thermal effect is bio-heat effect [90]. Intense acoustic energy is delivered to a small region of tissue, where the absorption process results in the tissue temperature rise to a relatively high value and causes thermal coagulation and ablation of cells (e.g. over 60°C for more than 1 second [91]). The second thermal mechanism is ultrasound-induced cavitation. The pressure rarefactions due to the ultrasound propagation can cause gas to be drawn out of solution in tissue to form bubbles. When these bubbles are further driven to oscillate and/or collapse by successive pressure oscillations, resulting in high mechanical stresses and shock waves which are further absorbed within the tissue [92]. These processes manifest as high temperatures within the insonated area. Although there are still many on-going discussions on other possible HIFU ablation mechanisms, the broadly accepted hypothesis is that tissue ablation results from a combination of both thermal and cavitation effects [93]. A magnetic resonance imaging (MRI)-guided ultrasound therapy tool for cancer treatment has been adopted due to its ability of temperature mapping [94].

Dual-frequency HIFU induced tissue ablation and cavitation

Despite the success of HIFU for many tumor ablations, unwanted lesion volume has hindered the full realization of the benefits of HIFU as a therapy option. In order to obtain tissue ablation with steeper temperature rise and enlarged lesion volume, dual-frequency HIFU has been studied in recent years by a few groups [95]-[100]. The dual-frequency experiments were carried out by simultaneously irradiating porcine liver regions of interest

with confocal ultrasound transducers at 1.563 MHz and 1.573 MHz (Fig. 3-2 and 3-3) [95]. It was found that dual-frequency FUS induces larger lesions than conventional single frequency FUS under the same power density. It was believed that the cavitation effect is more pronounced in the multi-frequency mode, which was well presented in the work done by Tatake et al [96]. Another possible explanation offered by Iernetti et al is the production of larger number of air bubbles by the introduction of the low-frequency (20 kHz) stimulating field, which aids in the cavitation effect [97]. Carpendo et al correlated the effect of dual-frequency excitation and the increase in heating effects to the combination resonance of the two ultrasonic fields [98]. It has been observed that using dual frequency, same amplitude waves can achieve a preferential cavitation threshold field where cavitation threshold at and near the focus is preferentially lower than that in the near-side, using a phased-array transducer [99]. It is noticed that these reported dual-frequency ablation experiments either used dual frequency with the lower frequency transducer in the 10-500 kHz range, or with the frequency difference less than 50 kHz. In cavitation detection experiments, frequency difference above 250 kHz (Fig. 3-4 and 3-5) and working frequency above 1 MHz [100] could still enhance the cavitation effect.

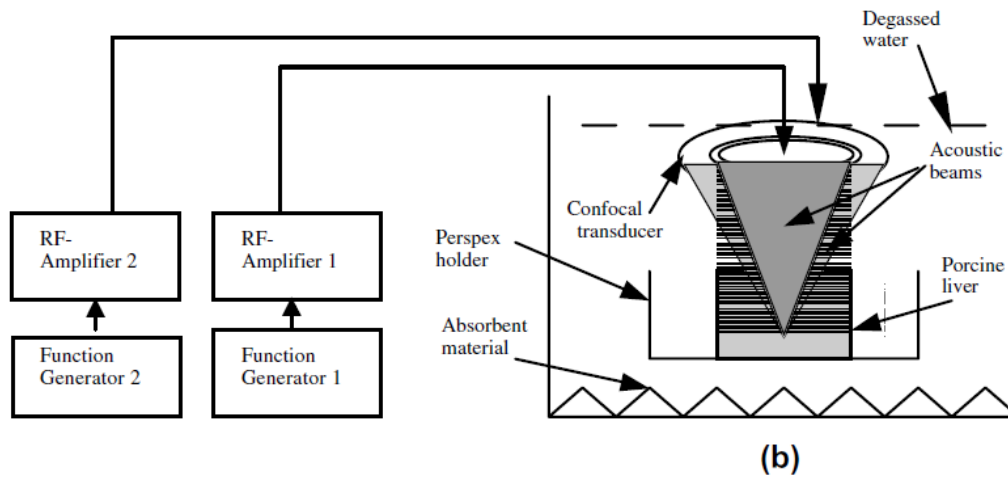


Figure 3-2. Schematic diagram of dual-frequency HIFU lesioning apparatus [9].

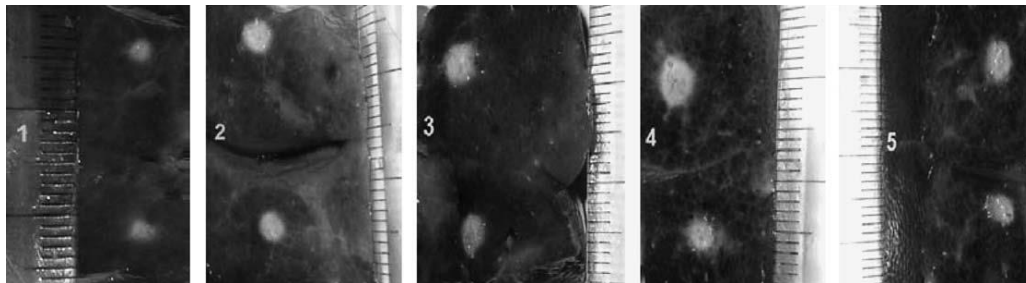


Figure 3-3. Photographs of lesions in the degassed liver samples induced by dual-frequency HIFU and conventional single-frequency HIFU (from 1 to 5, the exposure times are 10, 15, 20, 25 and 30 s, respectively) [9].

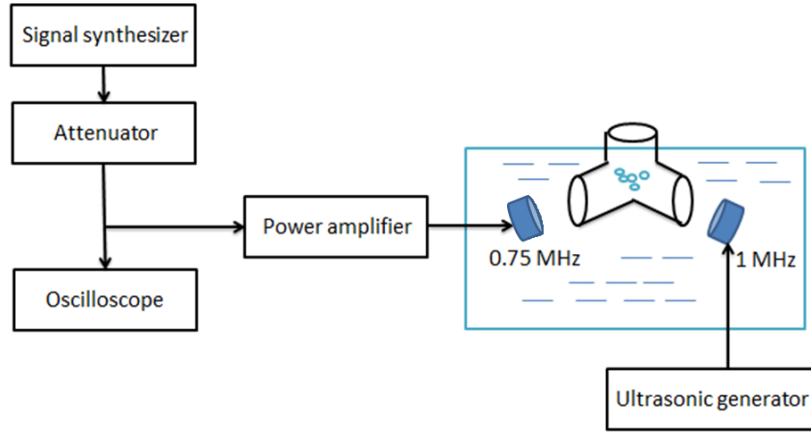


Figure 3-4. Experimental setup of dual-beam orthogonal low MHz sonication.

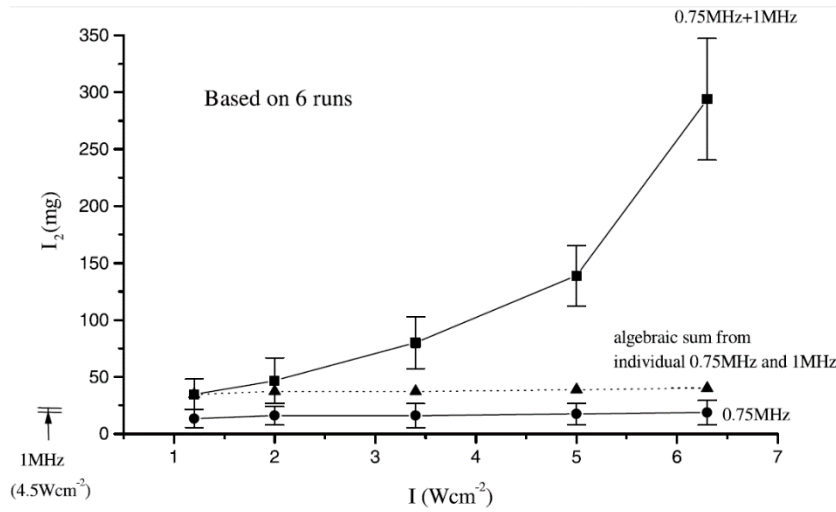


Figure 3-5. The amount of I_2 released (represent the cavitation efficiency) under dual-beam orthogonal low MHz ultrasound [100].

Furthermore, ultrasound imaging guided HIFU has drawn research interests in using multi-frequency ultrasound to enhance the ablating rate [101]. Tissue ablation using multi-frequency ultrasound with both high frequency (e.g., > 3 MHz) and low frequency (1-1.5

MHz) can be of interest because the high-frequency component can be used for imaging guidance of subsurface structures with a high resolution [102], while the effective tissue ablation can still be expected using the multi-frequency HIFU. However, there is no report about experimental results of temperature rise in tissue ablation with multi-frequency ultrasound in a MR imaging environment. In this work, we first conducted ablation tests on tissue-mimicking phantoms using single- and dual-frequency HIFU, while temperature mapping was obtained by using a MR scanner. For the first time, cavitation detection tests and theoretical models were also proposed to quantify the differences between single- and dual-frequency ultrasound induced cavitation yields.

3.1.2 Objective and approach

From the above background information, one can conclude that it is of the interest to investigate tissue ablation using multi-frequency HIFU (950 kHz~3.3 MHz) with frequency differences greater than 500 kHz and to analyze the effects of different governing parameters on the temperature rise during controlled therapeutic insonation. These parameters include the transmission frequency and the acoustic power exposure. In this case, our objective is to investigate multi-frequency HIFU-induced tissue ablation with frequency difference greater than 500 kHz. This work initiated with ablation on chicken breast using single- and dual-frequency HIFU and temperature measured by a needle thermocouple. Furthermore, we also conducted ablation tests on tissue-mimicking phantoms, while temperature mapping was obtained using a MR (magnetic resonance) scanner, which will help us further verify the efficiency of multi-frequency HIFU.

The combination of modeling and experiments was employed to understand the physics behind the differences in tissue ablation behavior between single- and multi-frequency ultrasound. In specific, we firstly simulated the nonlinear acoustic pressure field of the dual-frequency ultrasound for two different transducer positioning configurations. Temperature rise expected from thermoviscous heating was also calculated for both single- and dual-frequency ultrasound excitations based on a linear acoustic approximation. Experiments using single- and multi-frequency HIFU for tissue ablation were conducted with temperature recorded using both thermocouples and MRI (magnetic resonance imaging). The possible attribution of accelerated heating by multi-frequency ultrasound was discussed.

3.2 Tissue ablation modeling

3.2.1 Acoustic field modeling

To reveal the mechanism of multi-frequency HIFU ablation, it is critically important to understand the pressure field generated by such ultrasound excitations. In a nonlinear acoustic system, the wave travels faster during the high pressure phase of the oscillation than during the lower pressure phase, which can be explained by the fact that the local speed of sound will increase with the temperature rise caused by the absorption process in compressible materials. In this case with acoustic waveform changing, other frequency components will be introduced, rather than a linear system which only responses to the driving frequency. Non-linear acoustic simulation could provide more information in the frequency spectrum, which will help us analyze the differences between single- and multi-frequency acoustic fields. A k-space time-domain method was employed to simulate the

nonlinear acoustic field. Its accuracy has been extensively verified. This algorithm aims to solve the full Westervelt equation as shown below [103]

$$\rho_0 \nabla \cdot \left(\frac{1}{\rho_0} \nabla p \right) - \frac{1}{c_0^2} \frac{\partial^2 p}{\partial t^2} + \frac{\delta}{c_0^4} \frac{\partial^3 p}{\partial t^3} + \frac{\beta}{\rho_0 c_0^4} \frac{\partial^2 p}{\partial t^2} = 0, \quad (13)$$

where p is the acoustic pressure; c_0 is the speed of sound; ρ_0 is the density; β is the acoustic nonlinearity coefficient; δ is the sound diffusivity. It has been proven that this k-space method is significantly more accurate and efficient than the conventional finite-difference time-domain (FDTD) method for weakly inhomogeneous media, which is the case in this study [103]. The pressure amplitude on the transducer surface was estimated based on the measured output power by an acoustic power radiation balance (UPM-DT-1AV, Ohmic Instruments, Easton, MD), which serves as the acoustic source to our algorithm. The Matlab (MathWorks Inc, Natick, MA) code to solve this Westervelt equation was provided by Dr. Yun Jing.

By using the normalized wave field $f = p/\sqrt{\rho}$ and defining an auxiliary field $w = f + v$, where $v = \left(\frac{c_0^2}{c^2} - 1 \right) f$, Equation (13) can be reduced to

$$-\frac{1}{c_0^2} \frac{\partial^2 w}{\partial t^2} = \nabla^2 v - \nabla^2 w + \frac{q - h - d}{c_0^2}, \quad (14)$$

where

$$q = c_0^2 f \sqrt{\rho} \nabla^2 \frac{1}{\sqrt{\rho}}, \quad h = c_0^2 \frac{\beta}{\sqrt{\rho} c^4} \frac{\partial^2 f^2}{\partial t^2}, \quad d = c_0^2 \frac{\delta}{c^4} \frac{\partial^3 f^2}{\partial t^3}, \quad (15)$$

Fourier transformation of Equation (15) in the spatial domain yields the k-space equation

$$\frac{\partial^2 W}{\partial t^2} = c_0^2 k^2 (V - W) - (Q - H - D), \quad (16)$$

where $k = \sqrt{k_x^2 + k_y^2 + k_z^2}$, and W, V, Q, H and D are the sparial Fourier transforms of w, v, q, h and d, respectively, which can be calculated using a fast Fourier transform (FFT).

Equation (16) can be solved in a nonstandard finite difference approach to achieve the complete time stepping algorithm as

$$\begin{aligned} & W(t + \Delta t) - 2W(t) + W(t - \Delta t) \\ &= 4\sin^2\left(\frac{c_0 k \Delta t}{2}\right) \left[V - W - \frac{1}{c_0^2 k^2} (Q - H - D + M) \right], \quad (17) \end{aligned}$$

Nonlinear acoustic simulations were carried out in two conditions for dual-frequency ultrasound, which were used to analyze the difference between single- and dual-frequency ultrasound fields. In the first case it is assumed that dual-frequency ultrasonic beams were emitted from the same source and had an incidence angle of 45 ° to the tissue surface (Fig. 3-6(a)). In the other condition, the two beams were emitted from two different sources with 90 ° between their acoustic beam axes and both of them had the incidence angle of 45 ° to the tissue surface (Fig. 3-6(b)). While the former case has been extensively studied in recent

research [104], the latter configuration is the focus of this study and we show that it could shed light on the mechanism of multi-frequency HIFU for tissue ablations.

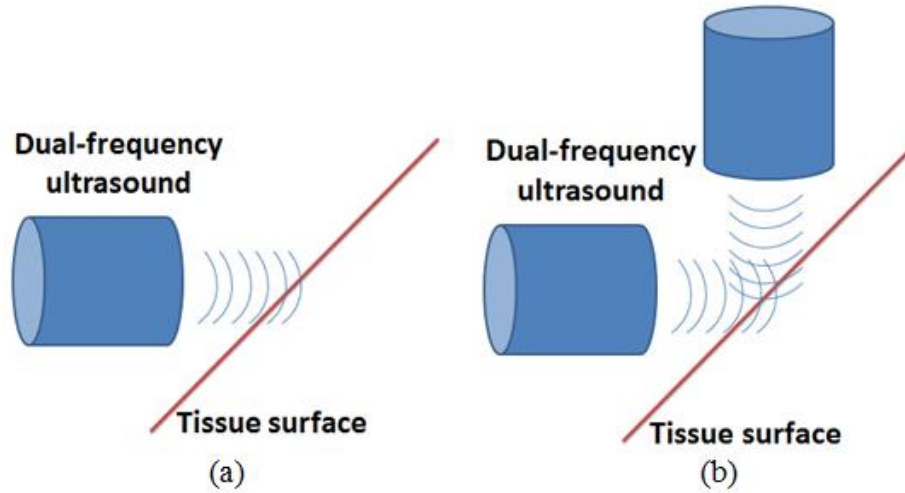


Figure 3-6. Schematic diagrams of tissue ablation using different HIFU configurations in simulations. (a) con-focal dual-frequency configuration; (b) separated dual-frequency configuration.

3.2.2 Temperature rise modeling

For the temperature rise simulation, linear acoustics was assumed in both single- and dual-frequency cases. This assumption is considered to be valid as it is shown that the amplitudes of harmonics are low compared with the fundamental frequency (see Fig. 3-11, the amplitude at the second harmonics is about 10 dB below that at the fundamental frequency), therefore contributing insignificantly to the temperature rises. The simulations of the linear intensity field of HIFU transducers were implemented in the Field II program [105], and a concave model was used with the input parameters (aperture radius, focal length

and focal pressure). Because the transducer is axially symmetric, so the emitted field was simulated on the y-z plane, in which the z direction is the acoustic axis. Temperature rise was estimated by solving the inhomogeneous Pennes equation of heat conduction in y-z plane [106], [107]

$$\frac{\partial T}{\partial t} = k\Delta(T) - \frac{T - T_0}{\tau} + \frac{q_v}{c_v}, \quad (18)$$

where T is the tissue temperature; T_0 is the room temperature, C_v is the heat capacity of a unit volume; k is the thermal diffusivity; Δ is the Laplace operator; τ is the characteristic time of the blood perfusion, which is not considered and is set to infinite in this simulation for chicken breast tissue. Equation (18) can be then rewritten as

$$\frac{\partial T}{\partial t} = k\Delta(T) + \frac{q_v}{c_v}, \quad (19)$$

where q_v describes the field of thermal sources generated by the ultrasonic wave absorption and is evaluated by the following equation

$$q_v = 2 \sum \alpha(f_n) I_n, \quad (20)$$

where n is the number of transducers used in the ablation, I_n represents the acoustic intensity field of each transducer, and $\alpha(f_n)$ is the acoustic absorption coefficient at the center frequency of each transducer. By solving this bio-heat equation with the calculated acoustic intensity field as an input, tissue temperature rise versus exposure time can be acquired.

3.3 Experimental method

3.3.1 Ultrasound transducers

Three single-frequency HIFU transducers and a dual-frequency one produced by Blatek (State College, PA) were used in experiments. The center frequencies of these transducers are 950 kHz, 1.5 MHz, 3.3 MHz, and combined 1.5 MHz/3 MHz, respectively. The aperture diameter and focal length of these transducers are shown in Table 3-1. They have the same dimensions which made it easier to build the fixture to hold them for ablation experiments. Fig. 3-7 describes the schematic geometry of the focal zone, where ablation is expected to occur in the experiments. The focal zone of the dual-frequency transducer is very similar to the single 1.5 MHz and 3.3 MHz transducer at each working frequencies. Prepared tissue samples were chosen to be much larger (length > 5 cm, width > 5 cm, height > 5 cm) than these focal zones, which means the sample lateral dimension is larger than the focal beam width, and the sample thickness should be larger than the focal length.

Table 3-1. Characteristics of ultrasound transducers used in tissue ablation experiments.

Center	Aperture	Focal
Frequency	Diameter	Length
950 kHz	29.5 mm	28 mm
1.5 MHz	29.5 mm	30 mm
3.3 MHz	29.5 mm	30 mm
1.5 and 3 MHz	29.5 mm	28 mm

Ultrasound transducer probes

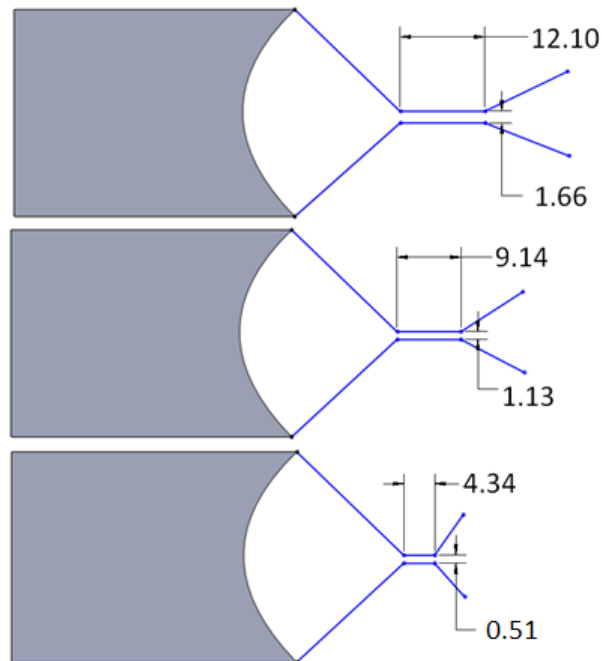


Figure 3-7. Schematic of the acoustic beam focal zone length and diameter (units of mm) of ultrasound transducers: 950 kHz transducer (top), 1.5 MHz transducer (middle) and 3.3 MHz transducer (bottom).

More details about the dual-layer, dual-frequency and single-aperture transducer could be found in [108] (Fig. 3-8). In such a dual-layer design, the dual frequency transducer could work at 3 MHz mode or 1.5 MHz mode, or combined frequencies. Dual-frequency ultrasound could be generated with one dual-frequency single input from an arbitrary waveform generator (Agilent Technologies Inc., Santa Clara, CA). Impulse spectrum clearly showed two strong resonant frequencies at about 1.5 MHz and 3 MHz with almost identical amplitudes. Relative to the fundamental frequency (1.5 MHz), high order of harmonics of the transducer at 4.5 MHz, 6 MHz and 7.5 MHz are very low, with amplitudes of -12.61 dB, -28.39 dB and -49.29 dB, respectively. Beam profile of the acoustic field was measured with a high power hydrophone (HYP-0, Omega Engineering Inc., Stamford, CT). Because of stronger focusing, the 3 MHz ultrasound shows smaller focal zone than the 1.5 MHz ultrasound. With the same voltage input (300 V), the pressure of 3 MHz ultrasound at focal point is 8.39 MPa compared to 6.64 MPa for 1.5 MHz ultrasound, corresponding to a power density of 2.35 kW/cm^2 for 3 MHz ultrasound beam and 1.47 kW/cm^2 for 1.5 MHz ultrasound beam, respectively. The pressure of the dual frequency ultrasound is 8.30 MPa and the power intensity is 1.48 kW/cm^2 at the same voltage input as single-frequency signals. Such power density is high enough to cause cavitation and hyperthermia effect, and thus resulting in lesion in bio-tissue [109].

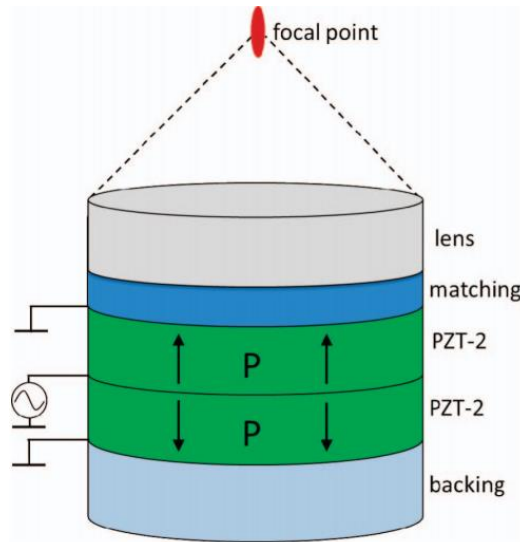


Figure 3-8. Configuration of the dual frequency transducer. Arrows on the transducer around “P” indicate the polarization direction [109].

In tissue ablation experiments, each transducer was driven by an amplified sinusoidal wave signal generated by function generators (SRS PS355, Sunnyvale, CA; Tektronix AFG3101, Beaverton, OR; Agilent 33250A, Santa Clara, CA), and amplified by RF power amplifiers (ENI AP400B, ENI 3700 and ENI 3100L, Lake Mary, FL). The input signal was set to match the center frequency of each corresponding transducer. Its input voltage was then selected to adjust the output acoustic power designed for these experiments.

Output acoustic power of each transducer was measured under different input electrical power using the acoustic power radiation balance. The results showed the relationship between input electrical power and output acoustic power of those transducers, so the output acoustic power could be controlled by adjusting the input electrical signals. In the tests, 25 W

output acoustic power was employed, and the corresponding input voltages are listed in Table 3-2.

Table 3-2. Input voltages for 25 W input power under different frequencies and the corresponding output acoustic powers.

Transducer type	Working frequencies (amplitude ratio)	Input peak-to- peak voltage	Output acoustic power
single- frequency transducers	Single 950 kHz	310 V	7.4 W
	Single 1.5 MHz	310 V	12.1 W
	Single 3.3 MHz	310 V	6.6 W
dual-frequency transducer	1.5 MHz	314 V	12.75 W
	3 MHz	350 V	7.00 W
	1.5 MHz : 3MHz = 1 : 1	319 V	9.87 W
	1.5 MHz : 3MHz = 3 : 1	329 V	11.31 W
	1.5 MHz : 3MHz = 5 : 1	340 V	11.79 W
	1.5 MHz : 3MHz = 10 : 1	348 V	12.22 W

Note: The first three rows describe the power measurements of the single-frequency transducers, and the rest rows show the output under various inputs for the dual-frequency transducer.

3.3.2 Tissue ablation monitoring using a thermocouple

The experimental setup for single-frequency and multi-frequency tissue ablation is

schematically shown in Fig. 3-9. Packaged frozen chicken breast tissue was brought to room temperature and left in open air for more than 30 minutes before being used for experiments. The tissue was cut to obtain a clean, flat surface from a bulk piece, and then mounted into a cylindrical PVC end cap with a diameter of 1.5 inches. 1 mm-thickness steel needles were used to hold the tissue in the designed position relative to the housing. In single-frequency tests, one transducer was set 45° to the tissue surface and focused on a certain depth (e.g., 5mm) into the tissue sample. A depth of 5mm was chosen to avoid significant heat dissipation into water. In multi-frequency tests, HIFU transducers with significantly different center frequencies (0.95 MHz, 1.5 MHz and 3 MHz) were mounted using fixtures to ensure that all transducers were focused on the same area inside the tissue.

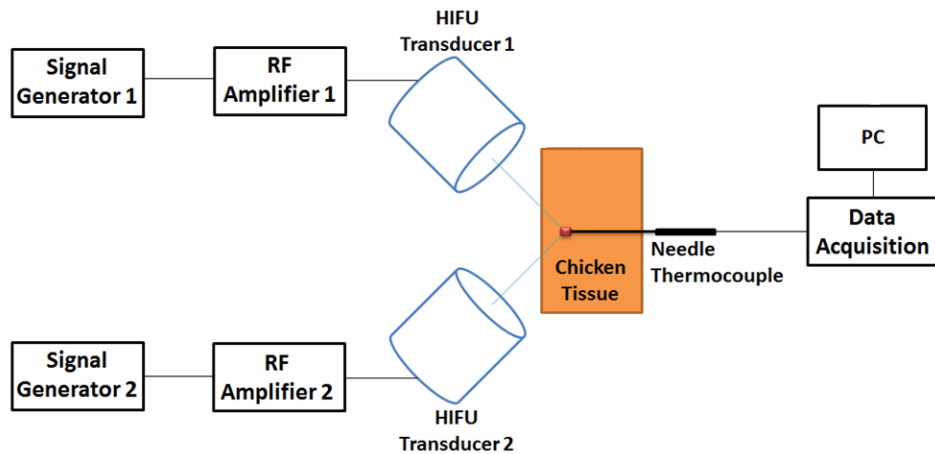


Figure 3-9. Schematic diagram of the experimental setup of dual-frequency tissue ablation tests using a thermocouple for temperature measurement.

A needle thermocouple probe (Omega HYP0, Stamford, CT) with diameter of 0.2 mm

was positioned inside tissue at the focal zone to measure the local tissue temperature. A needle thermocouple with the diameter smaller than the wavelength was chosen to reduce the acoustic field interference in tissue [110]. This T-type (Copper-Constantan) thermocouple probe is enclosed in a long hypodermic needle, and also has a fast response with a continuous temperature rating below 200 °C. The thermocouple signal was acquired via data acquisition system (USB-6361, NI, Austin, TX) for signal recording and processing.

The chicken tissue sample and HIFU transducers were aligned to let the transducers focus at 5 mm below the tissue surface. The ultrasound transducers and the data acquisition system for temperature recording were triggered at the same time. Each measurement consisted of a 30 seconds ultrasound exposure. Signals from thermocouple were simultaneously sampled at a rate of 100 samples per second. The total input electrical power of 15 W was introduced for both single- and multi-frequency ablations to compare the rises in temperature. In this case, the acoustic pressure at the focal point is calculated to be greater than 6 MPa under each frequency, which is found to be above the cavitation threshold through the analyses in ref. [111]. Each test was conducted four times to obtain the average value and standard deviation of the temperature rise.

3.3.3 Tissue-mimicking phantom ablation in a magnetic resonance imaging (MRI) environment

Magnetic resonance imaging is a medical imaging technique used in radiology to investigate the anatomy and function of the body in both health and disease. MRI scanners use strong magnetic fields and radiowaves to form images of the body. Most medical

applications rely on detecting a radio frequency signal emitted by excited hydrogen atoms in the body (present in any tissue containing water molecules) using energy from an oscillating magnetic field applied at the appropriate resonant frequency. The orientation of the image is controlled by varying the main magnetic field using gradient coils. As these coils are rapidly switched on and off they create the characteristic repetitive noises of an MRI scan. The contrast between different tissues is determined by the rate at which excited atoms return to the equilibrium state.

There are several different types of contrast agent. Image contrast may be weighted to demonstrate different anatomical structures or pathologies. T1 weighted image is one of the basic pulse sequences in MRI and demonstrates the differences in the T1 relaxation time of tissues. T1-weighted image is generated through different amounts of magnetization by changing the repetition time. This image weighting is useful for assessing the cerebral cortex, identifying fatty tissue, characterizing focal liver lesions and for post-contrast imaging. We produced T1-weighted images on a Siemens Trio 3T MR scanner (Siemens, Erlangen, Germany). Two objectives were taken into consideration while choosing the imaging parameters: 1) The resolution of the images had to be high enough to clearly show the focal region targeted by the HIFU transducer; 2) The volume of interest (VOI) had to be acquired in a sufficiently fast manner so that the sample would not cool down, losing the temperature contrast across the VOI. In order to achieve these two goals, the parameters for the 3D T1-MPRAGE sequence were chosen as follows: Number of slices = 52, Slice thickness = 1 mm, FOV = 58 mm x 141 mm, Matrix size = 29 x 128 (yielding an in-plane resolution of 2 mm x 1.1 mm). TE/TR = 3.28 ms/1130 ms, TI = 900 ms, Flip angle = 8°, GRAPPA acceleration

factor = 4, Phase partial Fourier factor = 6/8 and Slice partial Fourier factor = 6/8. Temperature calibration was done by imaging a gelatin phantom at various temperatures and recording the normalized image intensities. The normalization was done by dividing the intensity at the focal area by that at a region of interest in the non-focal area.

Gelatin phantom was prepared for ablation. 80% water and 20% beef gelatin (Kosher, Grayslake, IL) were mixed and heated to 80 °C, and then cooled down to room temperature. The HIFU transducer and phantom were placed in the head coil of the MRI scanner, as shown in Fig. 3-10. The phantom was filled into the bottom of a glass tube, and the transducer is stuck at the top of the tube by a movable holder in the vertical direction. Water was filled between the transducer and the phantom. The RF power amplifier and waveform generator sat outside the MRI room to avoid magnetic interference. For hyperthermia ablation comparison between single frequency and dual frequency ultrasound, acoustic power transmitted into tissue should be remained constant. For example, if 25 W was decided to be used in the ablation, the total input power of all frequency combinations was adjusted so that the output acoustic power is 25 W. In each test, 25% duty cycle burst was applied to excite the transducer for 30 seconds, and after that, the T1 weight of the phantom was imaged to estimate the target temperature. Various input powers and dual-frequency waveforms were tested to compare the efficiencies on temperature rise, and under each condition, more than three groups of results were collected to obtain the average values.

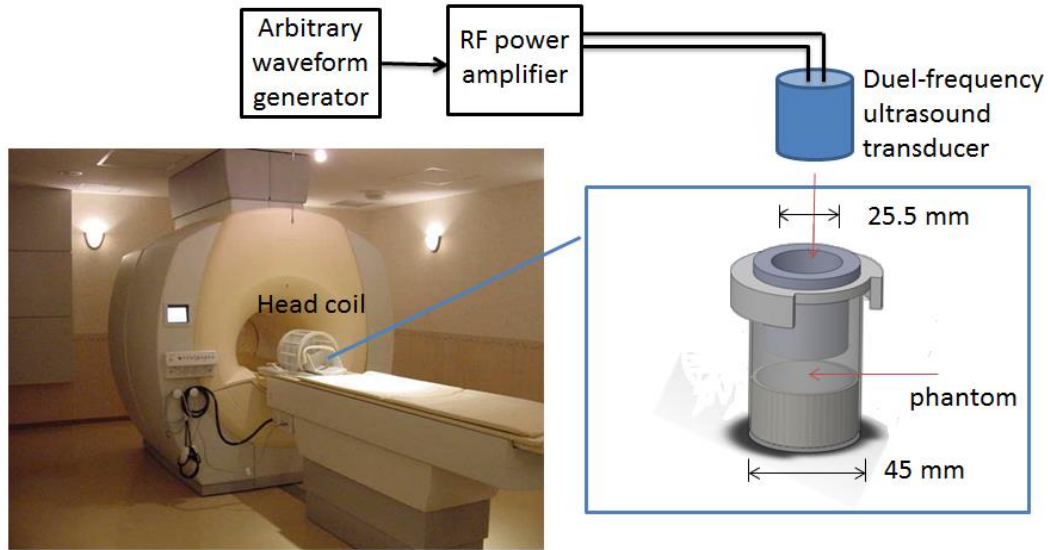


Figure 3-10. Schematic diagram of the tissue-mimicking phantom ablation tests in a MR scanner using a dual-frequency HIFU transducer. The HIFU transducer could be plugged into the fixture through the upper red arrow, and the gelatin phantom is placed at the bottom

3.4 Results and discussion

3.4.1 Modeling results

By solving the nonlinear acoustic equation and bio-heat transfer equation, the acoustic and temperature fields could be achieved. In nonlinear acoustic simulation, the frequency spectrums of pressure at the focal point are presented. In temperature simulation, the linear acoustic fields and induced temperature rise at the focal point are presented. Fig. 3-11 and 3-12 show the simulated nonlinear acoustic pressure (normalized frequency spectrum) at the focal point under the two conditions discussed in the section 3.2.1. 1.5 MHz and 3 MHz transducers were used, and the input pressure value in the simulation is the same as that in the transducer characterizations. Some parameters used in the simulation are listed here for

reference: $c_0 = 1500 \text{ m/s}$ in the water and $c_0 = 1550 \text{ m/s}$ in the tissue [112]; $\rho_0 = 1000 \text{ kg/m}^3$ for the water and $\rho_0 = 1060 \text{ kg/m}^3$ for the tissue; $\beta = 3.5$ for the water and $\beta = 3.9$ for the tissue; the sound diffusivity δ was calculated through the equation $\alpha = \delta \omega^2 / 2c_0^3$, where $\alpha = 4.28 \text{ m}^{-1}$ is the attenuation coefficient and ω is the angular frequency of ultrasounds [113]. The k-space algorithm currently considers an attenuation that is proportional to the frequency squared.

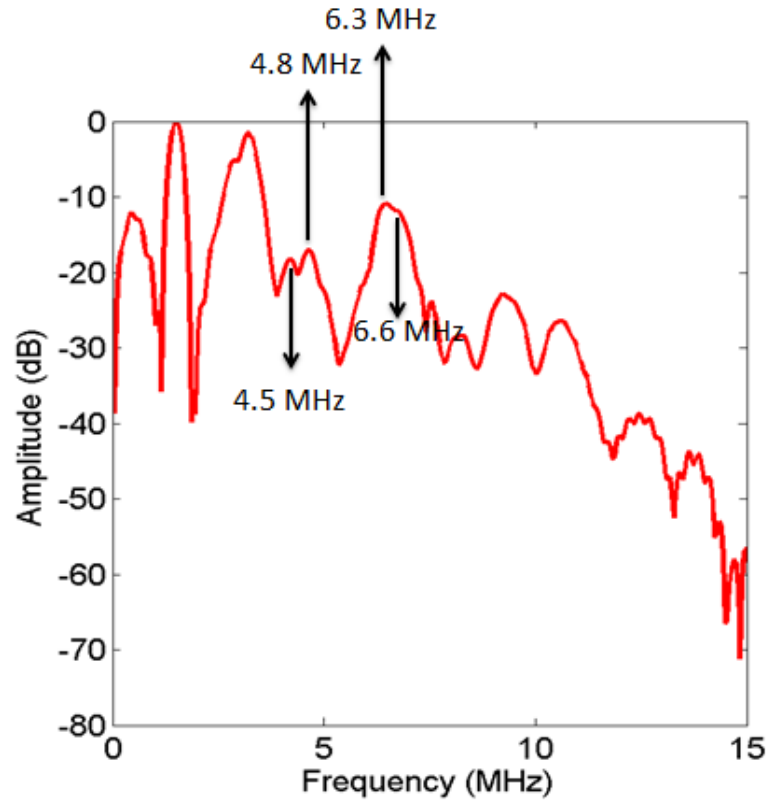


Figure 3-11. Simulation of acoustic pressure spectrum at the focal point while assuming dual-frequency ultrasound beams were emitted from a dual-frequency source as shown in Fig. 2(a).

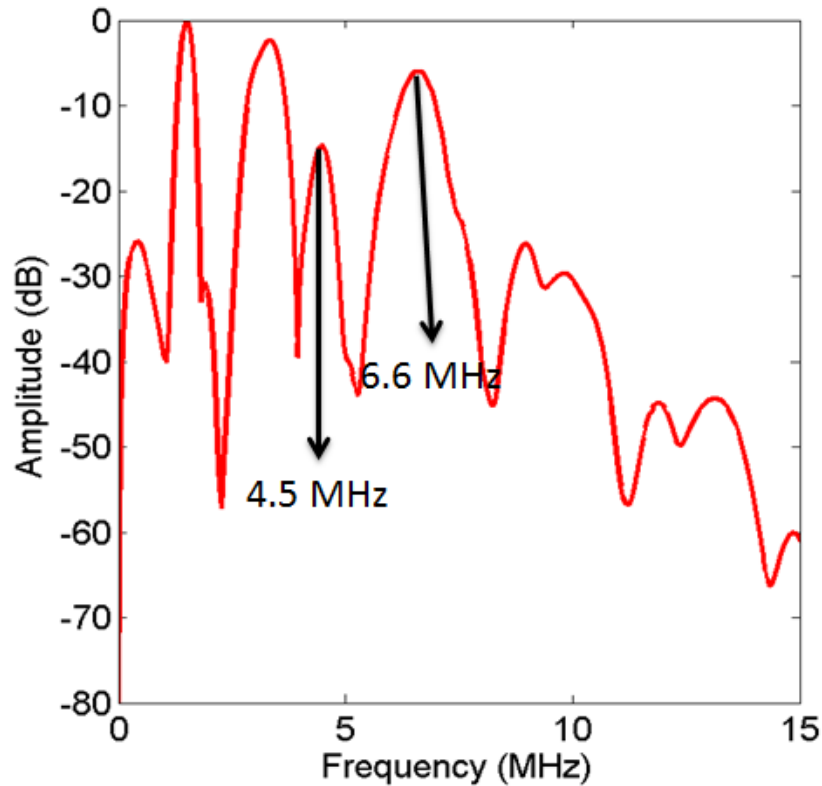


Figure 3-12. Simulation of acoustic pressure spectrum at the focal point while assuming dual-frequency ultrasound beams were emitted from two separated transducers as shown in Fig. 2(b).

Harmonic waves of the two center frequencies are clearly shown in both conditions. The amplitudes of those harmonic waves (3 MHz, 4.5 MHz and 6.6 MHz) are similar between the two configurations discussed in section 3.2.1. A. In addition, more components in the frequency domain are generated with significant amplitudes in the first confocal condition (Fig. 10), which indicates that the interactive effect is potentially greater. This is due to the fact that the ultrasound with multiple frequencies is emitted from the same transducer, so they will have interactions from the initial transducer plane all the way to the focal area. In

this case, more frequency components are shown in the acoustic field simulation results, e.g., 4.8 MHz (1.5 MHz + 3.3 MHz), 6.3 MHz (1.5 MHz \times 2 + 3.3 MHz), and etc. For the second non-confocal case, significant nonlinear interactions between the two different center-frequencies only occur near the focal point.

For the acoustic simulation with the Field II program (codes in Appendix II), we used the same dimensions and input pressure values from the transducer characterizations (Fig. 3-13). The acoustic simulation results were used to solve Equation (18). The parameters used include: $T_0 = 20\text{ }^{\circ}\text{C}$ is the room temperature, $C_v = 3.81 \times 10^6\text{ J/kg/}^{\circ}\text{C}$ is the heat capacity of a unit volume, $k = 1.3 \times 10^{-7}\text{ m}^2/\text{s}$ is the thermal diffusivity [114], and $\alpha = 4.28\text{ m}^{-1}$ at 950 kHz and 6.75 m^{-1} at 1.5 MHz. Temperature simulations were implemented for single-frequency modes (1.5 MHz, 3.3 MHz) as well as dual-frequency mode (1.5 MHz and 3.3 MHz combination) (see Fig. 3-14).

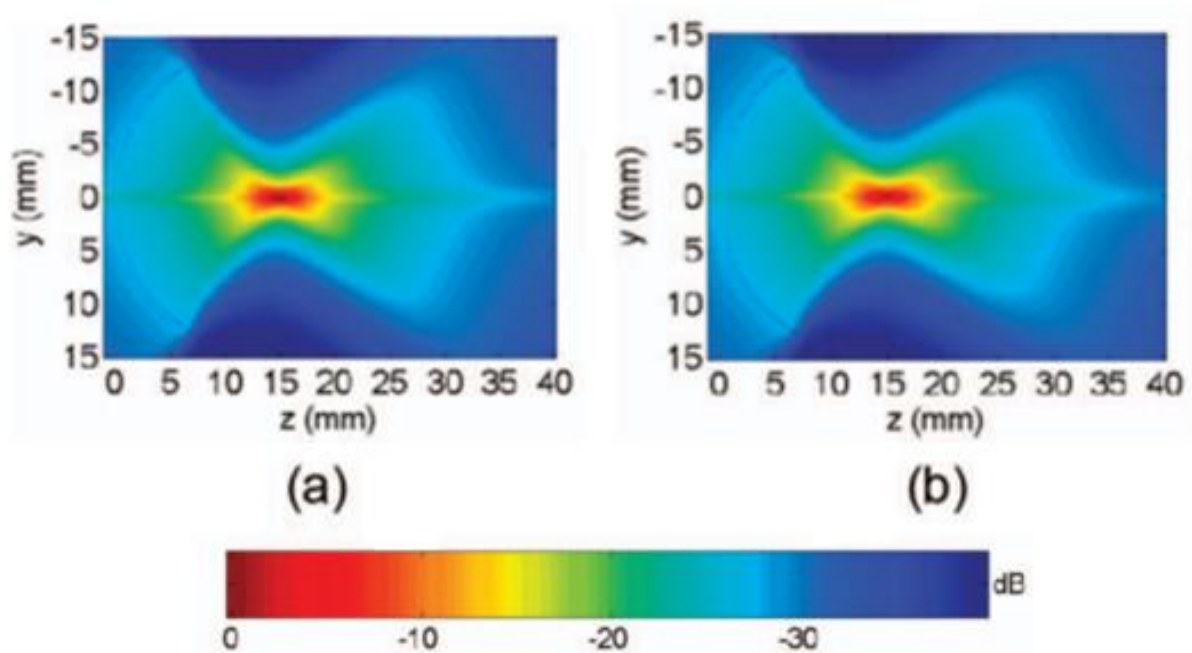


Figure 3-13. Simulated acoustic pressure field of (a) 950 kHz transducer, (b) 1.5 MHz transducer.

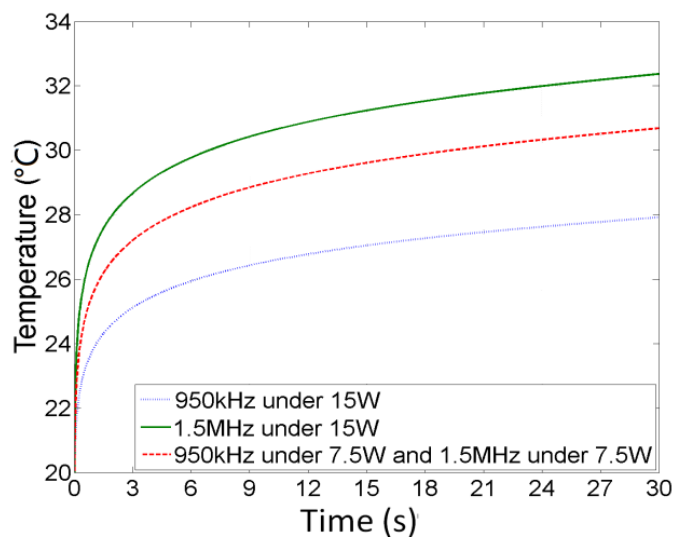


Figure 3-14. Simulated temperature vs. time of single- and dual-frequency tests between 950 kHz and 1.5 MHz under 15 W total input power for 30 seconds.

In the simulation where the cavitation effect was not considered, the dual-frequency ultrasound induced temperature rise is close to the algebraic average of single-frequency results. This also occurs in the simulation of tri-frequency ultrasound induced tissue ablation. This is due to the fact that in the solution to the bio-heat transfer function, the temperature is approximately proportional to the total input energy [115], or linearly related to the output intensity field of the ultrasound transducers. Therefore, tissue ablation using multi-frequency ultrasound does not lead to increased temperature rise compared to single-frequency ultrasound according to Pennes bio-heating theory. In other words, Pennes bio-heating theory considers acoustic absorption and heat transfer inside tissue without the involvement of cavitation.

3.4.2 Experimental results

Thermocouple measurement results

Tissue temperature (measured by a needle thermocouple) with respect to time using single- and dual-frequency tissue ablation are shown in Fig. 3-15 to Fig. 3-19. The average of the two single-frequency tests is also estimated against the exposure time. The total input electrical power is kept constant (e.g., 15 W) for all measurements, with an initial temperature of 20 °C for all tests as well. As an example, in Fig. 3-15, the total input power is maintained at 15 W. The input power of each transducer was 15 W for single-frequency tests. For dual-frequency tests, each transducer was supplied an electrical power of 7.5 W so that the total input power remained at 15 W. Fig. 3-16 and Fig. 3-17 presents the results using various groups of transducers (950 kHz and 3.3 MHz, 1.5 MHz and 3.3 MHz combinations).

For all the above measurements, the depth of focus was maintained at 5 mm below the tissue surface, as mentioned in the experimental setup. As can be seen in Fig. 3-15 to Fig. 3-17, higher temperatures and faster temperature rises can be obtained by using a dual-frequency mode HIFU ablation under the same total input power, indicating a more effective tissue ablation approach.

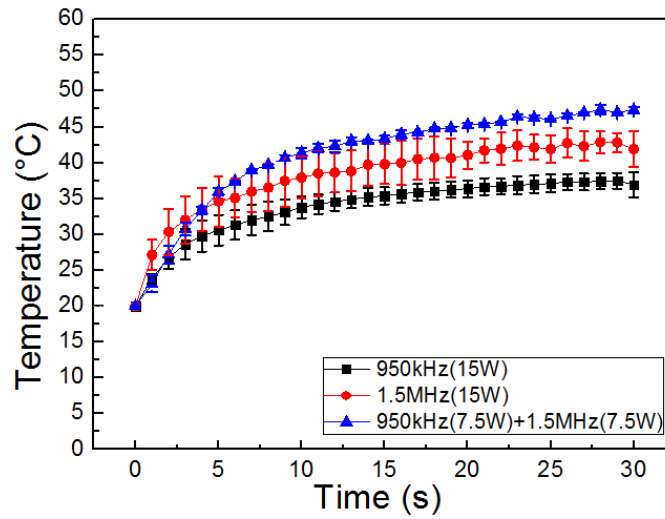


Figure 3-15. Measured change in chicken tissue temperature with exposure time for single frequency and dual-frequency (950 kHz and 1.5 MHz) tests under 15 W total input power, and 5 mm depth below the tissue surface.

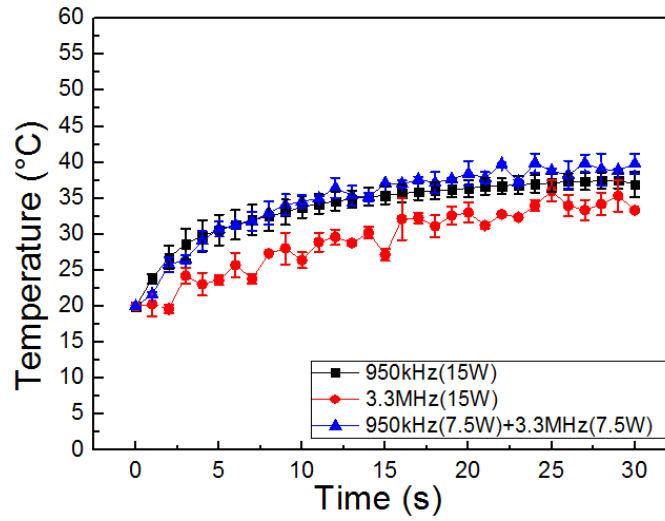


Figure 3-16. Measured change in chicken tissue temperature with exposure time for single-frequency and dual-frequency (950 kHz and 3.3 MHz) tests under 15 W total input power, and 5 mm depth below the tissue surface.

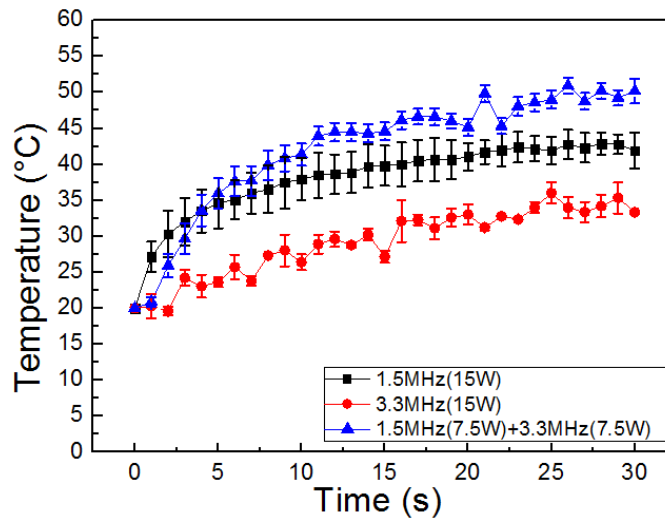


Figure 3-17. Measured change in chicken tissue temperature with exposure time for single-frequency and dual-frequency (1.5 MHz and 3.3 MHz) tests under 15 W total input power, and 5 mm depth below the tissue surface.

Tissue ablation tests with tri-frequency HIFU were also carried out with the total input power set at 15 W. Each transducer was supplied a power of 5 W. As shown in Fig. 3-18, the tissue temperature rise at 30 seconds in tri-frequency test is higher than those of single-frequency tests under the same input power. Although the results of tri-frequency tests are almost the same as those in two groups of dual-frequency tests, it is higher (about 4 °C at 30 seconds) than the algebraic average of dual-frequency results under the same power (see Fig. 3-19).

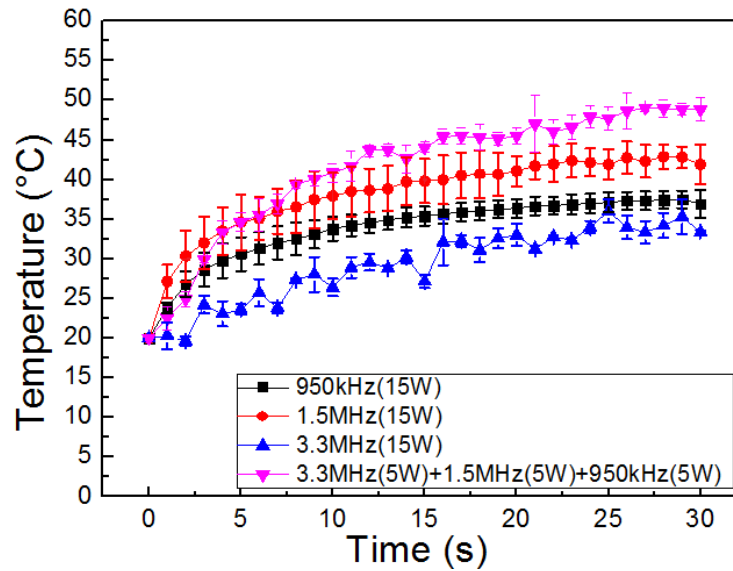


Figure 3-18. Measured change in chicken tissue temperature with exposure time for single-frequency and tri-frequency tests under 15 W total input power, and 5 mm depth below the tissue surface.

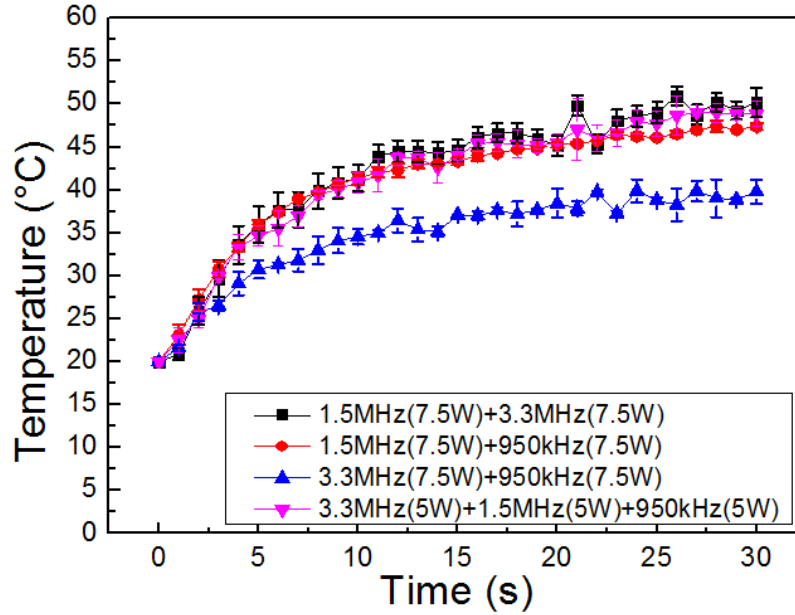


Figure 3-19. Measured change in chicken tissue temperature with exposure time for dual-frequency and tri-frequency tests under 15 W total input power, and 5 mm depth below the tissue surface.

Table 3-3 summarizes the average tissue temperature rise rate for the first and second 10 seconds of ablation and the temperature at the end of 30 seconds of ablation. Among single-frequency tests, we found that the results were different among the three transducers used in tests under the same power. The 1.5 MHz transducer could generate a higher temperature because of its higher power transfer efficiency, as shown in Table 3-3. Hence dual-frequency tests with the 1.5 MHz transducer lead to higher temperatures than the groups of 950 kHz and 3.3 MHz transducers. It was also noted that temperature rises in multi-frequency modes are always higher than that in single-frequency modes, and the temperature rise in tri-frequency mode is higher than the algebraic average of those in dual-frequency modes.

Table 3-3. Measured temperature rise (°C) at 10 seconds, 20 seconds and 30 seconds during the ablation experiments under different HIFU configurations.

Ultrasonic frequency	Temperature rise (°C)		
	10s	20s	30s
950kHz	13.8	16.4	16.9
1.5MHz	17.9	21.1	21.9
3.3MHz	6.4	13.0	15.3
950kHz and 1.5MHz	21.4	25.3	27.4
950kHz and 3.3MHz	14.6	18.4	19.8
1.5MHz and 3.3MHz	21.4	25.2	30.2
950kHz, 1.5MHz, 3.3MHz	20.8	25.5	28.8

MRI for ablation temperature measurement

In the ablation tests using MRI, the ultrasound was focused at 5 mm below the phantom surface. Burst ultrasonic waves were excited for 30 seconds, and after that, the T1 weight of the phantom was imaged to estimate the target temperature rise. The luminance change is proportional to the temperature rise in T1 weight imaging. Before testing, phantoms with different temperature were imaged before ultrasound exposure to calibrate the temperature mapping from T1 mode. The luminance of the phantom image was acquired and associated with the initial temperature (Fig. 3-20).

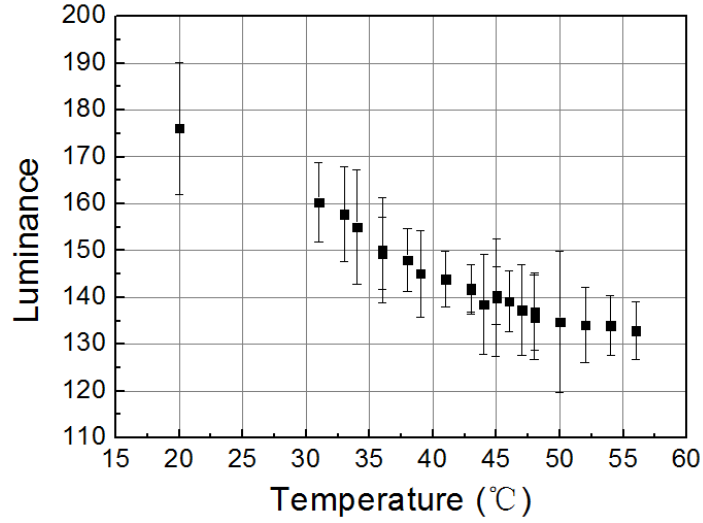


Figure 3-20. Temperature vs. imaging luminance in T1-MPRage mode on gelatin phantom.

The luminance at the focal area was then obtained from these images to estimate temperatures under different ultrasound exposures, where single frequency, various dual-frequency combinations of amplitude ratio between 1.5 MHz and 3 MHz were tested. Fig. 14 shows the MR images of phantom before (Fig. 3-21(a)) and after (Fig. 3-21(b) and (c)) sonications. One can see that the target area of dual-frequency induced ablation is darker and larger, indicating higher temperature within that area. Fig. 3-22 summarizes the temperature rise results under single-frequency ultrasound and several dual-frequency cases. In dual-frequency tests, the amplitude rate between 1.5 MHz and 3MHz was modified for efficiency comparison. It was found that dual-frequency ultrasound could generate about 20% more temperature rise, which in general agrees with our previous finding in chicken tissue ablation tests in non-MRI environment [28]. The slightly more temperature rise might be attributed to the fact that MRI avoids heat loss compared with thermocouple, and the dual-frequency

signal was modified from 1:1 mixture of 1.5 MHz and 3 MHz signals to 10:1. We introduced higher amplitude on 1.5 MHz because of its greater performance on temperature rise in single-frequency cases.

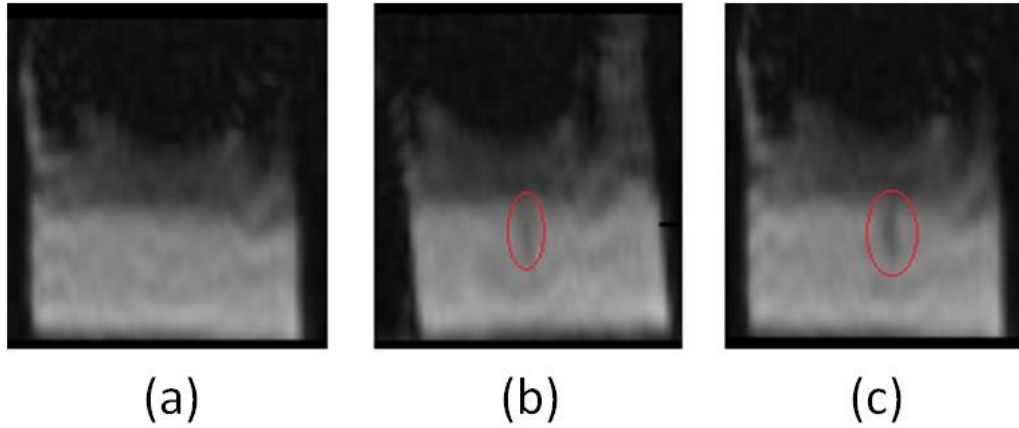


Figure 3-21. MR imaging of the phantom before and after HIFU exposure. The target areas of HIFU transducer are shown in the red circle (a) before ultrasonic exposure; (b) after 25 W single-frequency (1.5 MHz) exposure; and (c) after 25 W dual-frequency (1.5 MHz:3 MHz = 5:1) exposure.

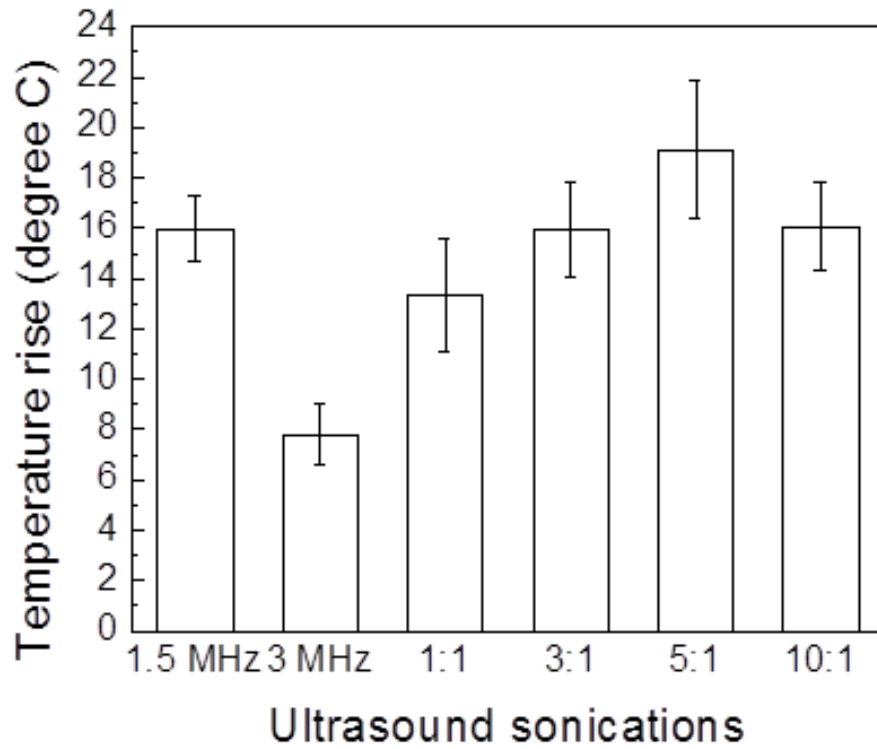


Figure 3-22. Temperature rises in single- and dual-frequency tests. The amplitude ratio shown is 1.5 MHz:3 MHz.

3.4.3 Discussion

The rate of temperature rise in HIFU treatment is an important characteristic, because it is directly related to the HIFU cancer treatment time. From our study using both thermocouple and MRI in tissue ablation, it was found that multi-frequency HIFU can yield up to 37.9 % (Table 3-4) improvement in temperature rise rate comparing with single-frequency ones, which can help shorten the duration of each current 2-3 hour HIFU treatment by about 0.5 hour for now, but further advancement could lead to a significant reduction in treatment time [116], [117].

Table 3-4. Summarized enhancement on temperature rise by multi-frequency ultrasound.

Temperature measure tools	Multi-frequency combinations	Temperature rise enhancement
Thermocouple	950 kHz and 1.5 MHz	25.1 %
	950 kHz and 3.3 MHz	17.1 %
	1.5 MHz and 3.3 MHz	37.9 %
	950 kHz, 1.5 MHz and 3.3 MHz	31.5 %
MRI	1.5 MHz and 3 MHz	18.75 %

From the nonlinear acoustic simulation results shown in Fig. 3-11 and Fig. 3-12, it is noted that the pressure amplitude at 1.8 MHz (the frequency difference of two primary working frequencies, $3.3 \text{ MHz} - 1.5 \text{ MHz} = 1.8 \text{ MHz}$) is lower in the case of non-confocal configuration (Fig. 3-12) than that in confocal configuration (Fig. 3-11). However, multi-frequency ultrasound with non-confocal configuration still showed promising and consistent enhancement on temperature rise in our tissue ablation tests (Fig. 3-8~3-12). According to the results shown in ref. [100], where a dual frequency ablation with 20 kHz frequency difference was adopted, it was believed that a multi-frequency wave will lead to a decrease in the cavitation threshold if a low frequency wave (e.g. 20 kHz) was introduced. Nevertheless, according to our findings, cavitation may still be triggered more efficiently in multi-frequency ablation, even though the frequency difference is as high as 1.8 MHz.

Dual-frequency ultrasound can generate higher temperatures under the same exposure conditions, which may be attributed to the cavitation field enhancement by nonlinear mixing of the primary frequencies. The nonlinearity of acoustic propagation results in waves with a wider range of frequencies. In other words, a combination of two or more different frequencies may even result in the formation of constructive and destructive interference patterns that are composed of waves with a wide range of frequencies and pressure amplitudes [118]. It is known that cavitation is a random frequency and pressure dependent phenomenon [119], and thus the generation of waves with a wide range of different frequencies increases the chance of more efficient energy dissipation during cavitation. Hence, more efficient tissue ablation can be achieved. Furthermore, nonlinear frequency mixing of multi-frequency ultrasound may locally reduce the cavitation threshold sufficiently [120] [121]. Another possible reason for this increase in efficiency may be that the radiation force inside the tissue contributes to the cavitation. When an incident wave is absorbed or scattered, a non-zero mean radiation force is exerted, which is proportional to the intensity of the wave and the local absorption or scattering properties of the tissue. With multi-frequency ultrasound, tissue is subject to the radiation force at different wave frequencies at the focal point of the transducers, which may trigger cavitation more efficiently [122].

In this project, we varied the working frequencies of the ultrasound and maintained other characteristics (total power, exposure time and the same focal area) of HIFU transducers to study the efficiencies of single- and dual-frequency ultrasound. There are other characteristics of HIFU treatment that are also important and may be affected when switching to multi-frequency. The size of the focal zone changing with time is one important

aspect in target therapy. We did not present the results in this chapter; since two separated transducers were used with a certain angle between them, which resulted in lesions not in typical shapes. The edge of the focal zone would also be essential in case to protect healthy tissue. We could either observe the size of the lesion or estimate the size from temperature field simulation results by solving the bio-heat transfer equation.

3.5 Summary

In this chapter, we combined modeling and experiments to study HIFU-induced tissue ablation behavior using single- and multi-frequency ultrasound. In specific, we firstly simulated the nonlinear acoustic pressure field of the dual-frequency ultrasound to achieve the frequency spectrums. Temperature rise expected from viscous heating was also calculated for both single- and dual-frequency ultrasound excitations based on a linear acoustic approximation. Experiments using single- and multi-frequency HIFU for tissue ablation were conducted with temperature recorded using both thermocouples and MRI (magnetic resonance imaging), in which, the results didn't agree with the temperature modeling without considering cavitation effect. The possible attribution of accelerated heating by multi-frequency ultrasound was discussed based on the simulated frequency spectrums.

Tissue ablation using multi-frequency HIFU yielded a up to 37.9 % higher temperature rise rate compared to ablation using single-frequency HIFU under the same exposure power and time. This finding has been varied by both thermocouple and MRI, but cannot be explained well by the Pennes bio-heating theory, which does not consider cavitation. It is believed that more effective tissue ablation using multi-frequency HIFU is attributed to the

enhanced cavitation effect based on the cavitation detection results. The non-linear acoustic simulation results suggest that acoustic waves with a wide range of frequencies may result in a more efficient cavitation than that by their single frequency counterparts. Finally, the multi-frequency HIFU with a relatively large frequency difference (more than 500 kHz) may lead to promising ultrasound imaging guided therapy.

CHAPTER 4 Multi-frequency cavitation study

4.1 Background

4.1.1 Cavitation effect and physics

Cavitation is the formation of vapor cavities in liquid, i.e. small liquid-free zones called "bubbles" or "voids". It usually occurs when a liquid is subjected to rapid changes of pressure which cause the formation of cavities. Cavitation was first studied by Lord Rayleigh in the late 19th century, when he considered the collapse of a spherical bubble within a liquid. It was found that when a volume of liquid is subjected to a sufficiently low pressure, it may rupture and form a cavity. When subjected to higher pressure, the cavities implode and generate an intense shockwave with significant radiated pressure [123]. Therefore cavitation is usually divided into two classes of behavior: inertial (or transient) cavitation and non-inertial (or stable) cavitation.

Inertial cavitation is the process where a bubble in a liquid rapidly collapses, producing a shock wave. In nature, inertial cavitation occurs in the vascular tissues of plants, as well as in the strikes of mantis shrimps and pistol shrimps. In man-made objects, it can occur in control valves, pumps, propellers and impellers. Non-inertial cavitation is the process in which a bubble in a fluid is forced to oscillate in size or shape due to some form of energy input, such as an acoustic field (Fig. 4-1). Such cavitation is often employed in ultrasonic cleaning baths and can also be observed in pumps, propellers, etc. [124]

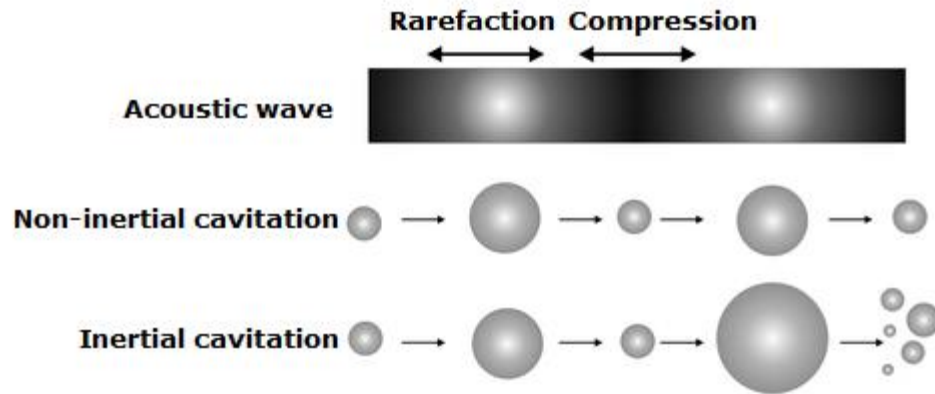


Figure 4-1. Non-inertial and inertial acoustic cavitation.

Ways of generating cavitation voids involve the local deposition of energy, such as high-intensity focused ultrasound [125]-[126], intensely focused laser (optic cavitation) [127] or with an electrical discharge through a spark [128]. Gas evaporates into the cavity from the surrounding medium. This cavity has a relatively low gas pressure because it is not a perfect vacuum. Such a low-pressure cavitation bubble in liquid begins to collapse due to the higher pressure of the surrounding medium. As the bubble collapses, the pressure and temperature within the cavity increase. The bubble eventually collapses to a minute fraction of its original size, at which point the gas dissipates into the surrounding liquid and a significant amount of energy is released in the form of an acoustic shock wave and as visible light. At the point of total collapse, the temperature within the bubble may be several thousand kelvin, and the pressure can be several hundred atmospheres [128].

Cavitation is a significant cause in some engineering applications. In biomedical engineering, cavitation plays an important role for the destruction of kidney stones in shock wave lithotripsy [129]; tests are being conducted as to whether cavitation can be used to

transfer large molecules into biological cells [130]; cavitation plays a key role in non-thermal non-invasive fractionation of tissue for treatment of a variety of diseases [131]; cavitation also probably plays a role in HIFU, a thermal noninvasive treatment methodology for cancer [132]-[133]. In chemical engineering, cavitation is often used to homogenize, or mix and break down, suspended particles in a colloidal liquid compound such as paint mixtures or milk [134]; the drastic decrease in pressure as the liquid accelerates into a larger volume induces cavitation. This method can be controlled with hydraulic devices that control inlet orifice size, allowing for dynamic adjustment during the process, or modification for different substances [135]. For some cleaning applications, cavitation has sufficient power to overcome the particle-to-substrate adhesion forces, loosening contaminants [136]-[137].

4.1.2 Multi-frequency ultrasound for cavitation enhancement

In engineering applications, most of cavitation effects are generated through acoustic waves. As described in the chapter 1, 2 and 3, we draw research interest in ultrasound in medicine and biology, so we look into the proper ways to enhance acoustic cavitation, which will benefit cavitation-involved ultrasound applications. In current years, multi-frequency ultrasound for enhancement of cavitation yields have been studied and demonstrated by a few research groups. It was demonstrated by Tatake that the cavitation effect is more efficient in the dual-frequency mode [138]. A cavitation zone with a higher bubble volume fraction [139] and larger number of bubbles [140] were noticed in a dual-frequency sonoreactor, compared to mono-frequency sonoreactors. It was also found that a three-beam configuration could further increase cavitation yield [141]. A possible explanation offered by

ternetti is the production of a larger number of air bubbles by the introduction of the low-frequency (20 kHz) stimulating field into a 700 kHz field, which aids the cavitation effect [142]. It was also observed that using a dual-frequency transducer, the same amplitude waves can achieve a preferential cavitation threshold field, cavitation threshold at and near the focus is preferentially lower than that in the nearside [143]. The dual-frequency tissue ablation experiments were carried out by simultaneously irradiating porcine liver regions of interest with confocal ultrasound transducers at 1.563 MHz and 1.573 MHz, where the frequency difference is 10 kHz, and in this work, it is demonstrated that the improved From published results on multi-frequency exceeding acoustic cavitation, it was found that by using a multi-frequency approach, the cavitation yield could be enhanced gradually. However, these multi-frequency approaches have not been verified theoretically, and thus the mechanism of multi-frequency ultrasound enhanced cavitation has not been understood very well.

4.1.3 Motivation, objective and approach

Recent research suggests that multiple-frequency ultrasound is capable of effectively enhancing the acoustic cavitation effect over single-frequency ultrasound. Potential applications of this cavitation enhancement can be widely applied for sonochemistry, and transdermal drug release. In this chapter, the enhanced effects of dual-frequency sonication on cavitation via a combined approach of experiments and multi-frequency cavitation bubble modeling are reported.

Cavitation was characterized using the PCD (passive cavitation detection) method. A dual-frequency focused ultrasound transducer (operating at 1.5 MHz, 3MHz, or a

combination thereof) was focused on tissue-mimicking phantom to generate cavitation. A 10 MHz confocally aligned transducer was focused at the target of the dual-frequency transducer to receive the broadband cavitation signals during the exposures. The model used for single-bubble dynamics was the Gilmore–Akulichev formulation, with gas diffusion included. The radiated pressure was calculated using the Akulichev formulation and correlated with received cavitation signals. The experimental results and the modeling results were then analyzed to understand the mechanism of dual-frequency ultrasonic cavitation.

4.2 Bubble cavitation modeling

4.2.1 Bubble dynamics modeling

The problem of how a bubble behaves in a liquid was first studied by Rayleigh [144]. Since then, many models have been developed, including the Gilmore equation [145]-[146] and the Rayleigh-Plesset Equation [147], [148], which were developed from Rayleigh’s work and were applied to the problem of traveling cavitation bubbles by Plesset [149]. In this work we use a form of the Gilmore equation, with gas diffusion included. This model was proposed and solved numerically for lithotripsy by Church [150]. We have reproduced Church’s numerical solution and briefly review the model here. Further details can be found in Chol et al. [151]. The Gilmore equation describes the oscillations of a single spherical bubble driven by an acoustic excitation and can be written in the following form:

$$R\dot{R}\left(1 - \frac{\dot{R}}{c}\right) + \frac{3}{2}\dot{R}^2\left(1 - \frac{\dot{R}}{3c}\right) = H\left(1 + \frac{\dot{R}}{c}\right) + H\frac{R}{c}\left(1 - \frac{\dot{R}}{c}\right), \quad (21)$$

where R is the bubble radius, a dot indicates a time derivative, c is the sound speed of the liquid at the bubble wall, and H is the difference in the liquid enthalpy between the bubble wall and infinity. The variable H can be represented as

$$H = \int_{P_{\infty}}^{p(R)} \frac{1}{\rho} dp, \quad (22)$$

here,

$$p(R) = p_g - \frac{2\sigma}{R} - \frac{4\mu}{R} \dot{R}, \quad (23)$$

$$p = p_0 + \frac{c_0^2 \rho_0}{n} \left[\left(\frac{\rho}{\rho_0} \right)^n - 1 \right], \quad (24)$$

The upper limit of the enthalpy integral is the pressure at the water–gas interface, where p_g is the pressure in the gas bubble, σ is the coefficient of surface tension, and μ is the coefficient of viscosity. The lower limit is $p_{\infty} = p_0 + P(t)$, the pressure at infinity, where $P(t)$ is acoustic pressure associated with the introduced ultrasound wave. Equation (24) is the Tait equation and n is the Tait parameter, p_0 is ambient pressure, ρ is the density of the liquid, ρ_0 is ambient density, and c_0 is small-signal sound speed.

To solve Equation (21), it is assumed that

$$y_1 = \frac{R}{R_0}, y_2 = \frac{R}{R_0 \omega}, \quad (25)$$

so Equation (21) could be rewritten as

$$\dot{R} \cdot y_1 R_0 \left(1 - \frac{y_2 R_0 \omega}{c}\right) + \frac{3}{2} (y_2 R_0 \omega)^2 \left(1 - \frac{y_2 R_0 \omega}{3c}\right) = H \left(1 + \frac{y_2 R_0 \omega}{c}\right) + \frac{(P-P_0)}{\rho c} \left(1 - \frac{y_2 R_0 \omega}{c}\right), \quad (26)$$

here H could be estimated as

$$H \approx \left(p_g - \frac{2\sigma}{R} - \frac{4\mu}{R} \dot{R}\right) \left(1 - \frac{V_m}{V_g}\right), \quad (27)$$

where V_m is the volume of a gas molecule and V_g is gas constant, therefore Equation (21) could be written as an ordinary differential equation as

$$\dot{R} = \left[\left(p_g - \frac{2\sigma}{R} - \frac{4\mu}{R} \dot{R}\right) \left(1 - \frac{V_m}{V_g}\right) \left(1 + \frac{y_2 R_0 \omega}{c}\right) + \frac{(P-P_0)}{\rho c} \left(1 - \frac{y_2 R_0 \omega}{c}\right) - \frac{3}{2} (y_2 R_0 \omega)^2 \left(1 - \frac{y_2 R_0 \omega}{3c}\right) \right] / y_1 R_0 \left(1 - \frac{y_2 R_0 \omega}{c}\right), \quad (28)$$

Equation (28) could be solved using the Matlab toolbox ode(23) (see Appendix III) to achieve y_2 , hence, y_1 R vs. time could be obtained. This model assumes that a bubble already exists. Most studies to date primarily covered experiments where dual-frequency ultrasound was used to induce the formation of microbubbles. After cavitation bubbles are formed, this model can estimate single bubble activity under different sonications.

4.2.2 Radiated force modeling

After computing the bubble activity under acoustic sonications, the radiated pressure correlated with received cavitation signals was performed. This generated pressure by bubble oscillation correlates with the received cavitation signal in PCD tests, and indicates the cavitation intensity. Radiated pressure is also used to estimate the global pressure acting on micropallets in ultrasound-induced cell sorting. The radiated pressure was calculated using the Akulichev formulation [158]

$$RF = p_0 + \frac{\rho_0 c_0^2}{n} \left[\left(\frac{2}{n+1} + \frac{n-1}{n+1} \times \sqrt{1 + \frac{n+1}{rc_0^2} G} \right)^{2n/n-1} - 1 \right], \quad (29)$$

where $G = \dot{R}H$ is an invariant of the bubble motion evaluated at the bubble wall and r is the distance from the bubble.

4.3 Experimental method

The dual-frequency, single-aperture MR-compatible transducer was used to generate acoustic cavitation in water, and this transducer was designed and fabricated as reported in chapter 3. The transducer was characterized through a pulse-echo test and the acoustic pressure and power was calibrated with a hydrophone (Onda HNA-0400, Onda Co., CA) and an acoustic power radiation balance (UPM-DT-1AV, Ohmic Instruments, Easton, MD). The dual frequency transducer can be operated to produce HIFU at 3 MHz, 1.5 MHz, or both simultaneously. The transducer was driven by an arbitrary waveform generator (Tektronix

AFG3101, Beaverton, OR) and amplified by a RF power amplifier (ENI 3100L, Rochester, NY).

A 10 MHz transducer (Panametrics V309, Olympus NDT Inc., Waltham, MA) with 50.8 mm focal length was focused at the target of the dual-frequency HIFU transducer to receive the broadband cavitation signals during the exposures (Fig. 46). The cavitation detection transducer was connected to a pulser/receiver (5900PR, Olympus, Center Valley, PA) with a 26 dB gain setting, and the received signals were processed through a 9.5 MHz high pass filter and converted to the frequency domain using a fast Fourier transform (FFT) coded in Matlab (The MathWorks Inc, Natick, MA). The cavitation signals were recorded during ultrasonic exposures with single frequency and dual frequency excitation, respectively. After 5 seconds of ultrasonic exposure, the received signals from the 10 MHz transducer became stable. The broadband acoustic cavitation signal was about 20 times lower in amplitude than the original signal at the primary frequencies without 9.5 MHz filtering. Through the use of the 9.5 MHz high-pass filter, the signal of the fundamental frequencies and low-order harmonics of the transducer were suppressed. After this post-processing, cavitation signals without major harmonics from the primary exciting frequencies were presented for comparison of the wideband cavitation pressures induced by single- and multi-frequencies.

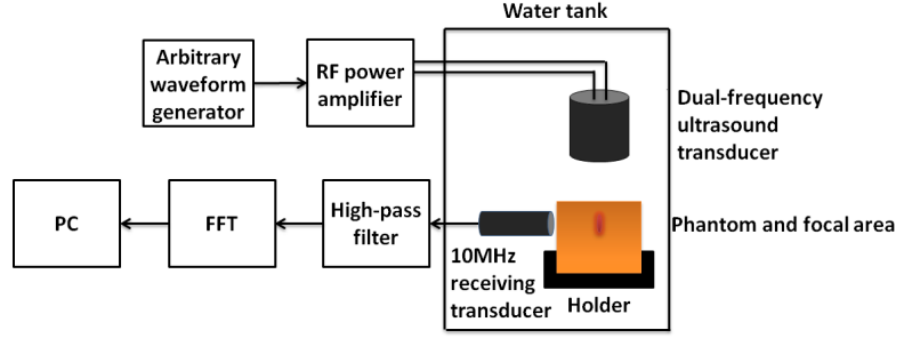


Figure 4-2. Schematic diagram of the experimental setup for cavitation detection by a 10 MHz receiving transducer.

4.4 Results and discussion

4.4.1 Bubble cavitation modeling results

Cavitation bubble model validation

The validity of the Matlab code for bubble dynamics modeling was first checked against others' results using signal-frequency excitations, especially Church's results. The input pressure function used by Church [150] was

$$P(t) = 2P_A e^{-\alpha t} \cos\left(\omega t + \frac{\pi}{3}\right) K(1 - e^{-\beta t}), \quad (30)$$

where $\alpha = 9.1 \times 10^5$ s, $K = 1.03$ (a constant), $\beta = 9.21 \times 10^7$ Hz. Also, $\omega = 2\pi f$ (with $f = 83.3$ kHz) was the radial frequency. The $K(1 - e^{-\beta t})$ part was added to account for a nonzero rise time. The resulting pressure function is plotted in Fig. 4-3(a) by Church, and in Fig. 4-3(b) by this work. The pressure pulse does indeed rise immediately and then fall

below zero, as described in the introduction. The bubble dynamics modeling results in Church's paper (Fig. 4-3(c)) was repeated; the modeled plot of normalized bubble radius vs normalized time is shown in Fig. 4-3(d). Here $P_A = 10^7$ Pascals. It can be seen that the time between the first minimum and the second minimum is less than 4.8×10^{-6} seconds, whereas in Figure 7 the difference is over 2.4×10^{-4} seconds. Also, the maximum normalized bubble radius reached is between 10 and 100. While Fig. 8 does show a little of the aftershocks, the aftershocks are not as pronounced as in Fig. 3a of Church. In fact, in Figure 8 here it appears as if there is a flat line between $\frac{t}{T_A} = 4$ and $\frac{t}{T_A} = 16$. In such a case, I think my model is nearly accurate compared with Church's results.

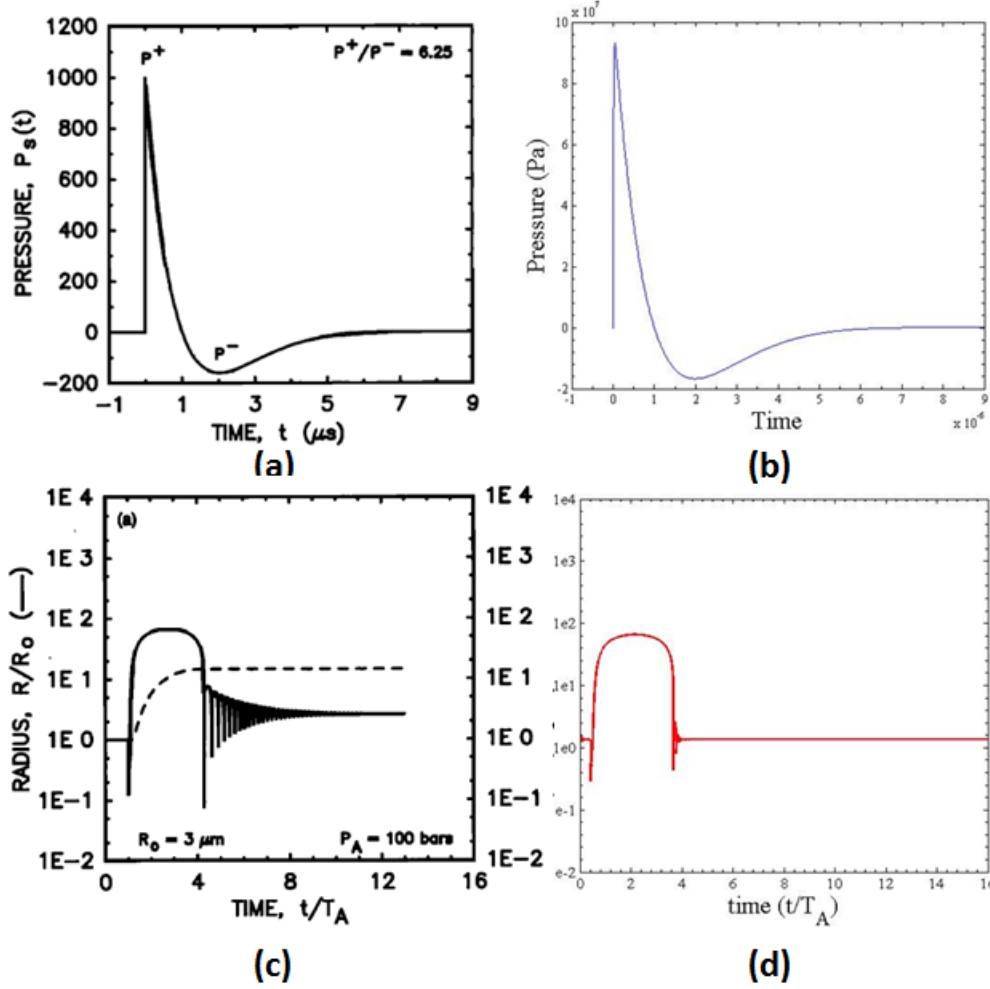


Figure 4-3. (a) Input pressure function used by Church [151]. (b) The pressure pulse as a function of time with the function in Church's paper. (c) The bubble dynamics modeling results in Church's paper. (d) Normalized bubble radius is plotted against normalized time, which corresponds to Fig. 47(a).

For the bubble dynamics modeling the following parameters were assumed: $p_0 = 1.05 \times 10^5 \text{ Pa}$, $c_0 = 1500 \text{ m/s}$, $\rho_0 = 1000 \text{ kg/m}^3$, $n = 10$, $\sigma = 0.0725 \text{ N/m}$, $\mu = 18.27 \mu\text{Pa}\cdot\text{s}$ [159]. Bubble dynamics modeling was performed assuming 10 μs pulsed 1.5MHz and 3MHz

sinusoids with amplitude of 2 MPa, which is similar to the pressure at the focal area in experimental studies in chapter 3 (Fig. 4-4).

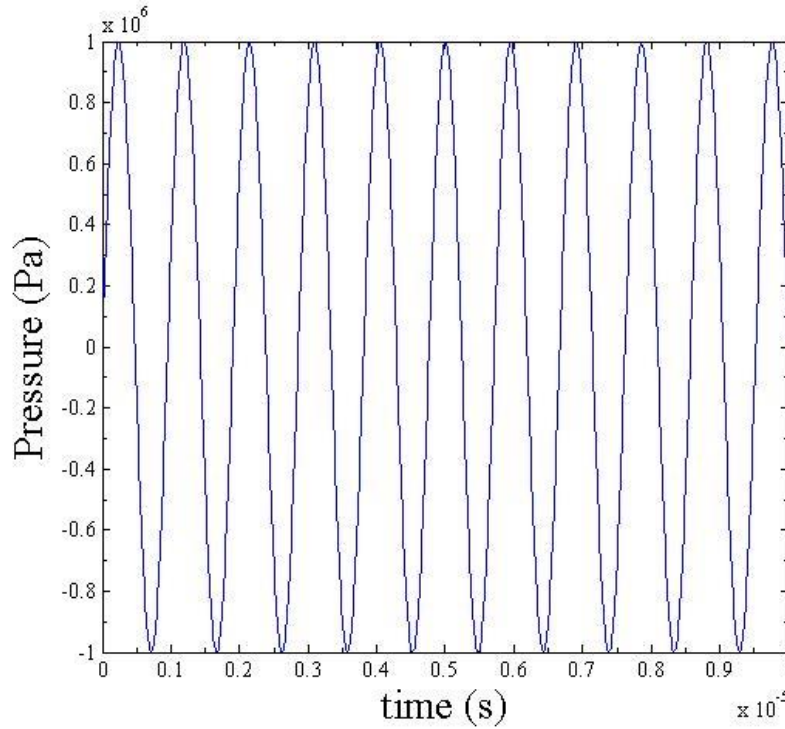
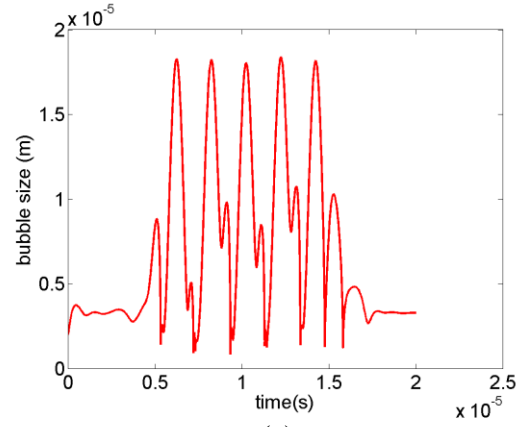


Figure 4-4. The pressure vs. time graph for the input acoustic excitation.

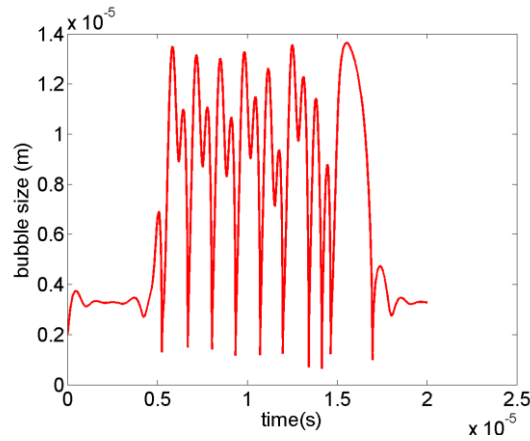
Cavitation bubble model results

Bubble dynamics modeling was performed assuming 10 μ s pulsed 1.5MHz and 3MHz sinusoids with amplitude of 2 MPa, which is similar to the measured pressure at the focal area in the experimental studies. The induced radiation pressure was calculated from the bubble radius-time curve. Fig. 49 shows the bubble diameter vs. time during each ultrasound excitation. The bubble diameter changes under dual-frequency excitation are less periodical

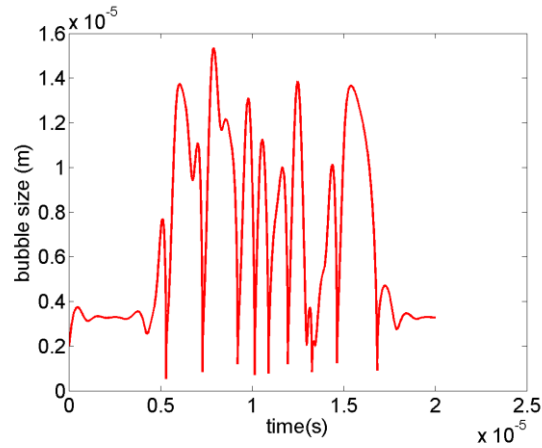
than in single-frequency ones, which is likely caused by the additional frequency differences from input waveforms. In Fig. 4-5, single-frequency ultrasound generated cavitation was compared to the dual-frequency case. It was found that, in the dual-frequency mode, the high-amplitude radiated pressure produced a higher root-mean-square of the received cavitation signal than in the single frequency cases (Fig. 4-6). The largest radiated pressure was generated with the amplitude ratio of 1.5 MHz : 3 MHz = 5:1 (Fig. 4-7). The radiated pressure may be correlated with the cavitation energy [159], which contributes to improving the cavitation effect. Since multi-bubble modeling is difficult, here the total radiated pressure is assumed to be proportional to the acoustic power in each case. Although the output acoustic power of 1.5 MHz is slightly higher than dual-frequency cases under the same input power, the radiated pressure enhanced by dual-frequency ultrasound is still significant.



(a)

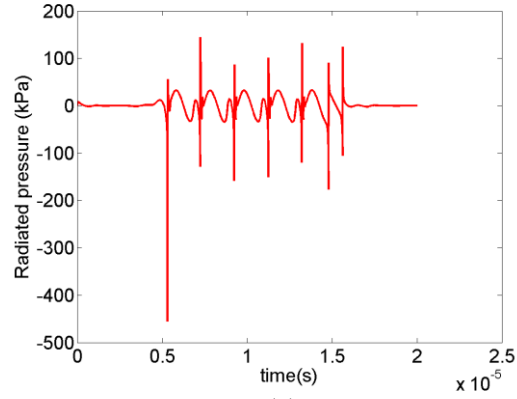


(b)

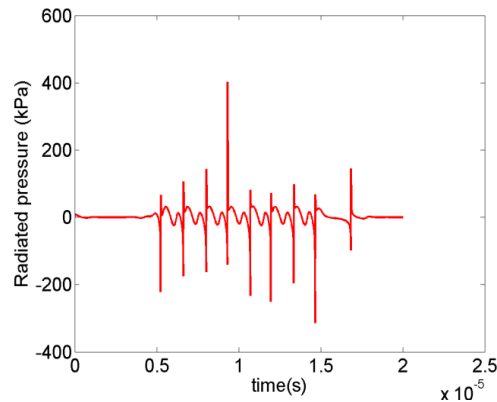


(c)

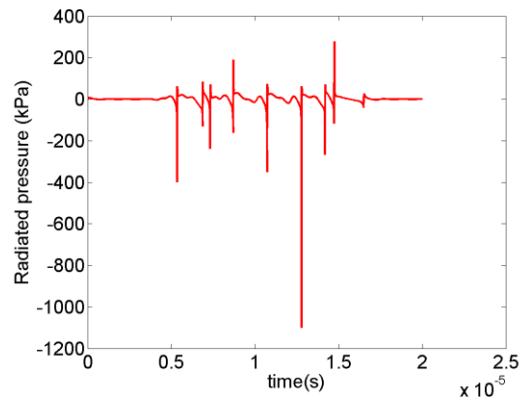
Figure 4-5. Bubble dynamics modeling shows the bubble diameter vs. time during 10- μ s excitations (a) under a 1.5 MHz ultrasonic excitation. (b) under a 3 MHz excitation. (c) under a dual-frequency (amplitude ratio of 3 MHz : 1.5 MHz is 1:5) excitation.



(a)



(b)



(c)

Figure 4-6. The generated cavitation pressure during the 10-ms bubble oscillation from the radiated pressure modeling. (a) in response to 1.5 MHz ultrasonic excitation. (b) in response to 3 MHz excitation. (c) in response to dual-frequency excitation (amplitude ratio of 3 MHz : 1.5 MHz is 1:5) excitation.

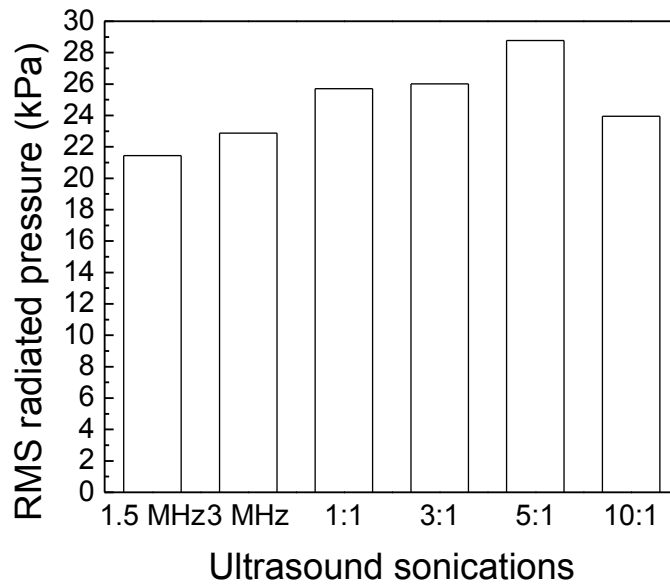


Figure 4-7. The calculated root-mean-square radiated pressure under different ultrasound sonications (the amplitude ratio shown is the value of 1.5 MHz : 3 MHz).

In order to verify the dual-frequency enhancement on cavitation, another important parameter – acoustic pressure is considered. It was found that in lower pressure excitation ($< 2\text{MPa}$), the dual-frequency ultrasound can increase the radiated pressure with particular amplitude ratio of 1.5 MHz : 3 MHz, like 20% of 3 MHz at 0.5 MPa and 1 MPa, 20% and 80% of 3 MHz at 1.5 MPa; but at higher pressure level ($\geq 2\text{ MPa}$), the generated radiated pressure by dual frequency is always above signal frequency (Fig.4-8).

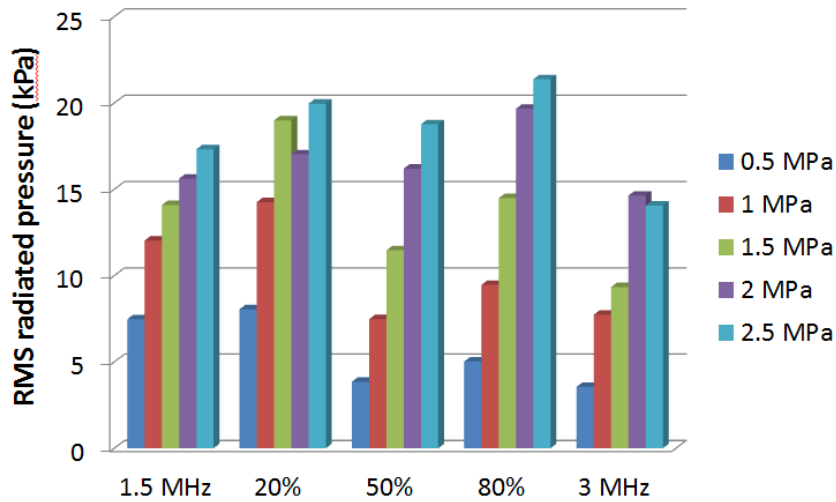


Figure 4-8. The calculated root-mean-square radiated pressure under ultrasound sonications with different acoustic pressure (the percentage shown is the amplitude rate of 3 MHz).

This model assumes that a bubble already exists. Most studies to date primarily covered experiments where dual-frequency ultrasound was used to induce the formation of microbubbles. After cavitation bubbles are formed, this model can estimate single bubble activity under different sonications. These simulation findings suggest that dual-frequency ultrasound may be used to enhance cavitation in tissue ablation.

4.4.2 Experimental results

The cavitation signals were recorded during ultrasonic exposures with single frequency and dual frequency excitation, respectively. After 5 seconds of ultrasonic exposure, the received signals from the 10 MHz transducer became stable. The broadband acoustic

cavitation signal was about 20 times lower in amplitude than the original signal at the primary frequencies without 9.5 MHz filtering.

From the filtered signals, the time average values of cavitation were calculated and compared (Fig. 4-9). For both single- and dual-frequency ultrasound, cavitation signals were detected while the acoustic powers were above 10 W. Significant enhancement on cavitation effect by dual-frequency was observed at relative high power levels (e.g. 25 W power level). The frequency spectra generated from dual frequency cavitation illustrated wider bandwidth and higher pressure peaks (Fig. 4-10) compared to signal-frequency induced cavitation. This finding was supported by the cavitation modeling results, and can be used to explain the findings in tissue mimicking phantom ablation tests (presented in Chapter 3) using this MR compatible dual frequency HIFU transducer.

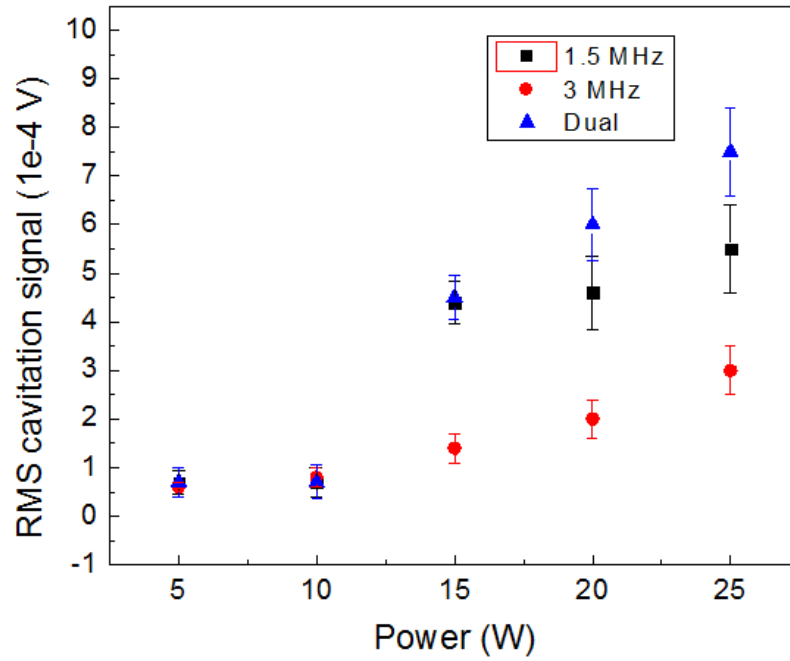


Figure 4-9. PCD signals from single-frequency ultrasound and dual-frequency ultrasound at 5 second after starting the ultrasound exposure.

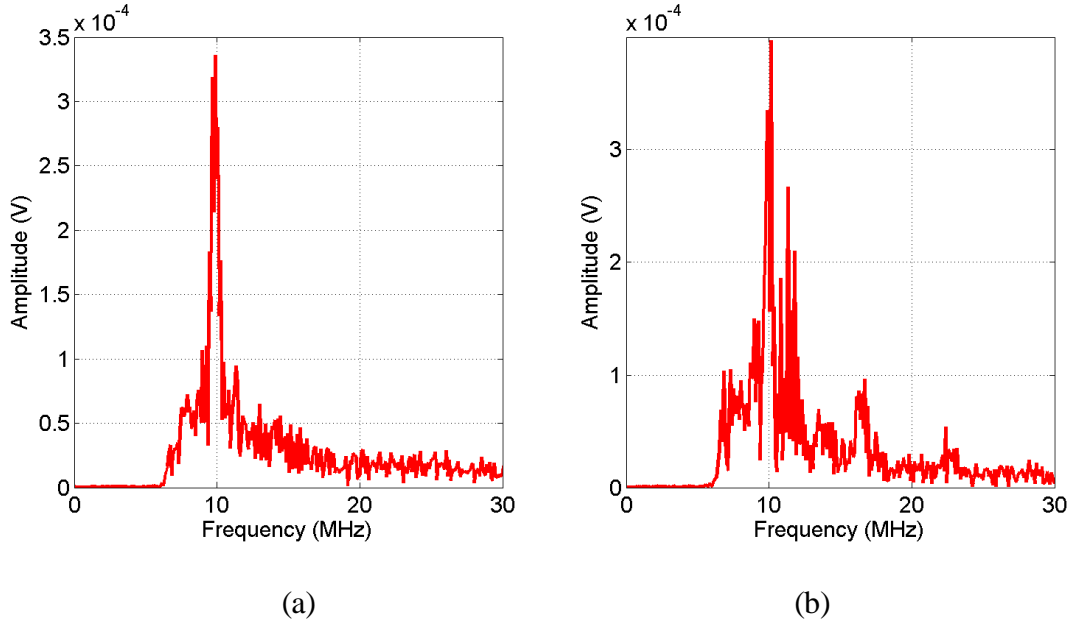


Figure 4-10. Frequency spectrum of single- and dual-frequency ultrasound. (a) single-frequency case with 1.5 MHz under 25 W acoustic power. (b) dual-frequency case with the amplitude rate of 1.5 MHz:3 MHz = 5:1 under 25 W.

4.5 Summary

It was found that the combination of dual-frequency ultrasound can produce a significant increase in cavitation yield compared with single-frequency sonication. 36% increase on the cavitation signal of dual-frequency ultrasound occurred at the highest employed acoustic power (25 W). The possible mechanisms of the enhanced effect may be explained by the bubble cavitation model, wherein the calculated radiated pressure generated from simulated bubble dynamics was greater (26%) under dual-frequency sonication at the same power level. The results from these studies are promising for the design of a multi-frequency ultrasound

system with enhanced cavitation for a number of biomedical, biological and chemical processing applications.

CHAPTER 5 Conclusions

High-power ultrasound has been proven to be promising in this dissertation in the two aspects: (1) multi-frequency HIFU-enhanced tissue ablation efficiency for more efficient HIFU therapies; (2) new high-intensity ultrasound technique for adherent cell sorting. Models for ultrasound induced different types of phenomenon including acoustic field, thermal transfer, acoustic radiation and acoustic cavitation were carried out to understand these techniques better, in combination with the experimental study. Based on the presented work in the previous chapters, the following conclusion can be drawn:

(1) High-power ultrasound has been proven to be able to induce microfabricated pallet release with adherent cells. This highly selective pallet/cell release method yielded significantly higher cell viability after selectively large single-pallet release, comparing with other existing methods, largely resulting from the relatively slow release speed and low radiation forces. The mechanisms behind the ultrasound-induced pallet release can be understood by looking into the combination of acoustic radiation force and acoustic cavitation against the attraction force between the pallets and the substrate. The parameters of the ultrasound transducer were optimized based on different pallet samples, and the design of the microarray was proposed to reduce the required release energy.

(2) Tissue ablation using multi-frequency HIFU with frequency difference of more than 500 kHz, yielded an up to 37.9 % higher temperature rise rate compared to ablations using single-frequency HIFU under the same exposure power and time. This finding has been validated by temperature measurements using both thermocouple and MRI, but cannot be explained well by the Pennes bio-heating theory, which does not consider

cavitation. It is believed that more effective tissue ablation using multi-frequency HIFU is attributed to the enhanced cavitation effect based on the cavitation detection results. The non-linear acoustic simulation results suggest that acoustic waves with a wide range of frequencies may result in a more efficient cavitation than that by their single frequency counterparts.

(3) The combination of dual-frequency ultrasound can produce a significant increase in cavitation yield compared with single-frequency sonication. 36% increase on the cavitation signal of dual-frequency ultrasound occurred at the highest employed acoustic power (25 W). The possible mechanisms of the enhanced effect may be explained by the bubble cavitation model. Multi-frequency acoustic cavitation model was carried out for the first time, wherein the calculated radiated pressure generated from simulated bubble dynamics was greater (26%) under dual-frequency sonication at the same power level.

Effectiveness of these techniques have been demonstrated in the previous chapters, however, it is believed that optimizing these techniques for either clinical or biological applications is still challenging in hardware design or pursuing a more efficient approach. For multi-frequency tissue ablation, the design for high-intensity multi-frequency ultrasound transducers with proposed working frequencies is critical and challenging, and more efficient therapy is a pursuit; for ultrasound induced pallet release, a phased-array ultrasound transducer is a need for an efficient cell sorting, because beam streaming can realize fast localization of the focus.

REFERENCES

- [1]. R. Novelline, Squire's fundamentals of radiology (5th ed.), *Harvard University Press*, pp. 34–35, 1997.
- [2]. B. Pollet, Power ultrasound in electrochemistry: from versatile laboratory tool to engineering, *Solution John Wiley & Sons*, chapter 1, 2012.
- [3]. J. F. Corso, “Bone-conduction thresholds for sonic and ultrasonic frequencies”, *Journal of the Acoustical Society of America*, vol. 35 (11), pp. 1738–1743, 1963.
- [4]. S. Takeda, I. Morioka, K. Miyashita, A. Okumura, Y. Yoshida and K. Matsumoto, "Age variation in the upper limit of hearing", *European Journal of Applied Physiology*, vol. 65 (5), pp. 403–408, 1992.
- [5]. "A ring tone meant to fall on deaf ears", *New York Times*, 2006.
- [6]. A. Popper and R. R. Fay, Hearing by bats (Springer Handbook of Auditory Research), *Springer*, vol. 5, 1995.
- [7]. L. A. Miller and A. Surlykke, “How some insects detect and avoid being eaten by bats. The tactics and counter tactics of prey and predator”, *BioScience*, vol. 51, pp. 570–581, 2001.
- [8]. G. Jones and D. A. Waters, "Moth hearing in response to bat echolocation calls manipulated independently in time and frequency", *Proceedings of the Royal Society B, Biological Sciences*, vol. 267 (1453), pp. 1627–1632, 2000.
- [9]. M. Kaplan, “Moths jam Bat Sonar, throw the predators off course”, *National Geographic News*, 2009.

- [10]. A. Surlykke and L. A. Miller, "The influence of arctiid moth clicks on bat echolocation; jamming or warning?" *Journal of Comparative Physiology A*, vol. 156 (6), pp. 831–843, 1985.
- [11]. J. Tougaard, L. A. Miller and J. A. Simmons, Advances in the study of echolocation in bats and dolphins, *Chicago University Press*, pp. 365–372, 2003.
- [12]. W. L. Whitlow, The sonar of dolphins, *Springer*, 2011.
- [13]. R. A. Kastelein, P. Bunscoek, M. Hagedoorn, W. L. Au and D. D. Haan, "Audiogram of a harbor porpoise (*Phocoena phocoena*) measured with narrow-band frequency modulated signals", *The Journal of the Acoustical Society of America*, vol. 112 (1), pp. 334–344, 2002.
- [14]. D. A. Mann; D. M. Higgs, W. N. Tavolga, M. J. Souza, A. N. Popper, "Ultrasound detection by clupeiform fishes", *The Journal of the Acoustical Society of America*, vol. 109 (6), pp. 3048–3054, 2001.
- [15]. Y. Hui, Food plant sanitation, *CRC Press*, p. 289, 2003.
- [16]. Vertebrate pests: problems and control, *National Academies*, vol. 5(1697), p. 92, 1970.
- [17]. ASTM; K. A. Fagerstone, R. D. Curnow, ASTM Committee E-35 on Pesticides, ASTM Committee E-35 on Pesticides, Subcommittee E35.17 on Vertebrate Pest Control Agents, Vertebrate pest control and management materials, *ASTM International*, vol. 6(1055), pp. 8, 1989.
- [18]. K. H. Buschow, Encyclopedia of Materials, *Elsevier*, pp. 5990, 2001.
- [19]. E. P. Papadakis, Ultrasonic instruments & devices, *Academic Press*, pp. 752, 1999.

- [20]. G. D. Betts, Inactivation of food-borne microorganisms using power ultrasound in encyclopedia of food microbiology, *Academic Press*, pp. 2202, 2000.
- [21]. N. J. Hangiandreou, "Physics tutorial for residents: topics in US: B-mode US: basic concepts and new technology – Hangiandreou". *Radiographics*, vol. 23 (4), pp. 1019, 2003.
- [22]. FDA radiological health – ultrasound imaging, *Fda.gov*, 2011.
- [23]. DistanceDoc and MedRecorder: new approach to remote ultrasound imaging| solutions | epiphan systems, *Epiphan.com*, 2011.
- [24]. "Ultrasound imaging of the pelvis", *radiologyinfo.org*, 2013.
- [25]. Ultrasound characteristics of the uterus in the cycling mare and their correlation with steroid hormones and timing of ovulation, *Equine-reproduction.com*, 2011.
- [26]. McKinnon and Voss, Equine reproduction, *Lea & Febiger*, 1993.
- [27]. D. Bennett, Subiaco abbey's angus herd, *Delta Farm Press*, 2010.
- [28]. W. Wagner, "Extension Effort in Beef Cattle Breeding & Selection", *West Virginia University Extension Service*, 2010.
- [29]. M. H. Rapacholi, Essentials of medical ultrasound: a practical introduction to the principles, techniques and biomedical applications, *Humana Press*, 1982
- [30]. "UIT solutions video", *appliedultrasonics.com*, 2012.
- [31]. "Tools of the trade", *appliedultrasonics.com*, 2012.
- [32]. A. S. Peshkovsky, S. L. Peshkovsky and S. Bystryak, "Scalable high-power ultrasonic technology for the production of translucent nanoemulsions", *Chemical Engineering and Processing: Process Intensification*, vol. 69, pp. 77–62, 2013.

- [33]. S. L. Peshkovsky, and A. S. Peshkovsky, "Matching a transducer to water at cavitation: acoustic horn design principles", *Ultrason. Sonochem.*, vol. 14, pp. 314–322, 2007.
- [34]. A. S. Peshkovsky and S. L. Peshkovsky, "Industrial-scale processing of liquids by high-intensity acoustic cavitation - the underlying theory and ultrasonic equipment design principles", *NY: Nova Science Publishers*, 2010.
- [35]. A. S. Peshkovsky, S. L. Peshkovsky "Acoustic cavitation theory and equipment design principles for industrial applications of high-intensity ultrasound", *NY: Nova Science Publishers*; 2010.
- [36]. J. L. Dion, A. Malutta and P. Cielo, "Ultrasonic inspection of fiber suspensions", *Journal of the Acoustical Society of America*, vol. 72 (5), pp. 1524–1526, 1982.
- [37]. H. J. Van Leeuwen, B. Akin, S. K. Khanal, S. Sung and D. Grewell, "Ultrasound pre-treatment of waste activated sludge", *Water Science & Technology: Water Supply*, vol. 6(6), p. 35, 2006.
- [38]. U. Neis, K. Nickel and A. Tiehm, "Enhancement of anaerobic sludge digestion by ultrasonic disintegration", *Water Science & Technology*, vol. 42 (9), pp. 73, 2000.
- [39]. S. Oie, N. Masumoto, K. Hironaga, A. Koshiro and A. Kamiya, "Microbial contamination by ultrasonic humidifier", *Microbios*, vol. 72 (292–293), pp. 161–166, 1992.
- [40]. A. Kumar and R. A. Maurya. Efficient synthesis of hantzsch esters and polyhydroquinoline derivatives in aqueous micelles, *Synlett*, pp. 883–885, 2008.
- [41]. J. G. Butler, *Television: critical methods and applications*, *Routledge*, pp. 276, 2006.
- [42]. Guidelines for the safe use of ultrasound Part II – industrial & commercial applications – safety code 24, *Health Canada*, 1991.

- [43]. AGNIR, Health effects of exposure to ultrasound and infrasound, *Health Protection Agency*, pp. 167–170, 2010.
- [44]. <http://www.fusfoundation.org/Funded-Projects/robust-mr-thermometry-for-mrghifu-in-breast-and-liver>
- [45]. http://www.accessdata.fda.gov/cdrh_docs/pdf10/K100874.pdf
- [46]. S. A. Sapareto and W. C. Dewey, "Thermal dose determination in cancer therapy", *International journal of radiation oncology, biology, physics*, vol. 10 (6), pp. 787–800, 1984.
- [47]. Food and drug administration approval, *ExAblate*, 2000.
- [48]. E. A. Stewart, B. Gostout, J. Rabinovici, H. S. Kim, L. Regan and M. C. Tempany, "Sustained Relief of Leiomyoma Symptoms by Using Focused Ultrasound Surgery", *Obstetrics & Gynecology*, vol. 110 (2), pp. 279–287, 2007.
- [49]. <http://www.insightec.com/>
- [50]. [http://www.wvtf.org/index.php?option=com_content&view=article&id=573:uva-pioneers-a-way-to-stop-tremors&catid=48:wvtf-news&Itemid=.](http://www.wvtf.org/index.php?option=com_content&view=article&id=573:uva-pioneers-a-way-to-stop-tremors&catid=48:wvtf-news&Itemid=)
- [51]. G. Suarez, Medical Director Emeritus at International HIFU, <http://www.hifumedicalexpert.com/faq.html>.
- [52]. K. Ahrar, S. Matin, C. G. Wood, M. J. Wallace, S. Gupta, D. C. Madoff, S. Rao, N. M. Tannir, E. Jonasch, L. L. Pisters, M. A. Rozner, D. L. Kennamer and M. E. Hicks, "Percutaneous Radiofrequency Ablation of Renal Tumors: Technique, Complications, and Outcomes", *Journal of Vascular and Interventional Radiology*, vol. 16 (5), pp. 679–688, 2005.

- [53]. V. Margulis, E. D. Matsumoto, G. Lindberg, L. Tunc, G. Taylor, A. I. Sagalowsky and J. A. Cadeddu, "Acute histologic effects of temperature-based radiofrequency ablation on renal tumor pathologic interpretation", *Urology*, vol. 64(4), pp. 660–663, 2004.
- [54]. A. H. Mahnken and J. Mahnken, "Perkutane radiofrequenzablation von Nierentumoren", *Der Radiologe*, vol. 44 (4), pp. 358–363, 2004.
- [55]. F. Wu, Z. Wang, Y. Cao, W. Chen, J. Bai, J. Zou, H. Zhu, "A randomised clinical trial of high-intensity focused ultrasound ablation for the treatment of patients with localised breast cancer", *British Journal of Cancer*, vol. 89 (12), pp. 2227–2233, 2003.
- [56]. "Philips sonalleve receives CE mark for MR-guided focused ultrasound ablation of metastatic bone cancer", *Philips Healthcare*, 2013.
- [57]. <http://www.fda.gov/downloads/AboutFDA/.../CDRH/.../UCM279434.pdf>
- [58]. A. Gelet, F. Murat and L. Poissonier, "Recurrent prostate cancer after radiotherapy – salvage treatment by high-intensity focused ultrasound", *European Oncological Disease1*, vol. 1, pp. 60–62, 2007.
- [59]. USHIFU, "Clinical information about HIFU in the U.S.", 2012.
- [60]. K. Hynynen, C. Damianou, A. Darkazanli, E. Unger, M. Levy and J. F. Schenck, "On-line MRI monitored noninvasive ultrasound surgery", *Proceedings of the Annual International Conference of the IEEE Engineering in Medicine and Biology Society*, 1992.
- [61]. A. Wolff, I. R. Perch-Nielsen, U. D. Larsen, P. Friis, G. Goranovic, C. R. Poulsen, J. P. Kutter and P. Telleman, "Integrating advanced functionality in a microfabricated high-throughput fluorescent-activated cell sorter", *Lab Chip* 3, pp. 22-27, 2003.

- [62]. S. M. Young, M. S. Curry, J. T. Ransom, J. A. Ballesteros, E. R. Prossnitz, L. A. Sklar and B. S. Edwards, "High-throughput microfluidic mixing and multiparametric cell sorting for bioactive compound screening", *Biomol. Screening*, vol. 9, pp. 103-111, 2004.
- [63]. B. Welm, F. Behbod, M. A. Goodell and J. M. Rosen, "Isolation and characterization of functional mammary gland stem cells", *Cell Proliferation*, vol. 36, pp. 17-32, 2003.
- [64]. E. J. Mackie, C. N. Pagel, R. Smith, M. R. de Niese, S. J. Song and R. N. Pike, "Protease-activated receptors: a means of converting extracellular proteolysis into intracellular signals", *IUBMB Life*, vol. 53, pp. 277-281, 2002.
- [65]. M. Mike, Y. Nakamura, A. Takahashi, Y. Nakaya, H. Eguchi, T. Masegi, K. Yoneda, S. Yasouka, S. J. Sone, "Effect of human airway trypsin-like protease on intracellular free Ca^{2+} concentration in human bronchial epithelial cells", *Med. Invest.*, vol. 50, pp. 95-107, 2003.
- [66]. D. Patel, *Separating Cells*, Springer-Verlag, 2001.
- [67]. J. Crossman, "Molecular mechanisms of "detachment-induced apoptosis—Anoikis", *Apoptosis*, vol. 7, pp. 247-260, 2002.
- [68]. R. J. Hay, "Human cells and cell cultures: availability, authentication and future prospects." *Cell*, vol. 9, pp. 143-152, 1996.
- [69]. P. Reddig R. Juliano, "Clinging to life: cell to matrix adhesion and cell survival", *Cancer Metastasis Rev.*, vol. 24, pp. 425-439, 2005.
- [70]. G. T. Salazar, Y. Wang, G. Young, M. Bachman, C. E. Sims, G. P. Li and N. L. Allbritton, "Micropallet Arrays for the Separation of Single, Adherent Cells", *Anal. Chem.*, vol. 79, pp. 682-687, 2007.

- [71]. Y. Wang, G. Young, M. Bachman, C. E. Sims, G. P. Li and N. L. Allbritton, "Collection and Expansion of Single Cells and Colonies Released from a Micropallet Array", *Anal. Chem.*, vol. 79, pp. 2359-2366, 2007.
- [72]. G. T. Salazar, Y. Wang, C. E. Sims, M. Bachman, G. P. Li and N. L. Allbritton, "Characterization of the laser-based release of micropallets from arrays", *Journal of Biomedical Optics*, vol. 13(3), 034007, 2008.
- [73]. Y. Wang, G. Young, P. C. Aoto, J. H. Pai, M. Bachman, G. P. Li, C. E. Sims and N. L. Allbritton, "Broadening cell selection criteria with micropallet arrays of adherent cells", *Cytometry*, vol. 71A, pp. 886-874, 2007.
- [74]. Y. Wang, C. Phillips, W. Xu, J. H. Pai, R. Dhopeswarkar, C. E. Sims and N. Allbritton, "Micromolded arrays for separation of adherent cells", *Lab Chip*, vol. 10, pp.2917-2924, 2010.
- [75]. N. M. Gunn, R. Chang, T. Westerhof, G. P. Li, M. Bachman and E. L. Nelson, "Ferromagnetic Micropallets for Magnetic Capture of Single Adherent Cells", *Langmuir*, vol. 26(22), pp. 17703-17711, 2010.
- [76]. J. A. Jensen, N. B. Svendsen, "Calculation of pressure fields from arbitrarily shaped, apodized, and excited ultrasound transducers", *IEEE Transactions on, Ultrasonics, Ferroelectrics and Frequency Control*, vol. 39, pp. 262-267, 1992.
- [77]. P. A. Quinto-Su, G. T. Salazar, C. E. Sims, N. L. Allbritton and V. Venugopalan, "Mechanisms of Pulsed Laser Microbeam Release of SU-8 Polymer "Micropallets" for the Collection and Separation of Adherent Cells", *Anal. Chem.*, vol. 80, pp. 4675-4679, 2008.

- [78]. H. J. Griffiths, J. G. Harvey, J. Dean, J. Curran, A. E. Markaki and T. W. Clyne, "Characterisation of cell adhesion to substrate materials and the resistance to enzymatic and mechanical cell-removal", *MRS conf. proc., Symposium GG: Mechanical Behavior of Biological Materials and Biomaterials*, vol. 1097, Epaper 08_GG3-5, 2008.
- [79]. D. Debavelaere-Callens, L. Peyre, P. Campistron and H. F. Hildebrand, "On the use of ultrasounds to quantify the longitudinal threshold force to detach osteoblastic cells from a conditioned glass substrate", *Biomolecular Engineering*, vol. 24, pp. 521-525, 2007.
- [80]. O. V. Rudenko, A. P. Sarvazyan and S. Y. Emelianov, "Acoustic radiation force and streaming induced by focused nonlinear ultrasound in a dissipative medium", *Journal of the Acoustical Society of America*, vol. 99(5), pp. 2791-2798, 1996.
- [81]. L. A. Kuznetsova and W. T. Coakley, "Applications of ultrasound streaming and radiation force in biosensors", *Biosensors and Bioelectronics*, vol. 22, pp. 1567-1577, 2007.
- [82]. G. R. Torr, "The acoustic radiation force", *Am. J. Phys*, vol. 52(5), pp. 402-408, 1984.
- [83]. L. P. Gor'kov, *Soc. Phys. Dokl.* vol. 6, pp. 773-775, 1962.
- [84]. J. Hultstom, O. Manneberg, K. Dopf, H. M. Hertz, H. Brismar and M. Wiklund, "Proliferation and viability of adherent cells manipulated by standing-wave ultrasound in a microfluidic chip", *Ultrasound in Medicine & Biology*, vol. 33(1), pp. 145-151, 2007.
- [85]. J. G. Lynn, R. L. Zwemer, A. J. Chick, and A. E. Miller, "A new method for the generation and use of focused ultrasound in experimental biology," *J. Gen. Physiol.*, pp. 179-193, 1942.

- [86]. W. J. Fry, W. H. Mosberg, J. W., and F. J. Fry, "Production of focal destructive lesions in the central nervous system with ultrasound," *J. Neurosurg.*, vol. 336, pp. 471-478, 1954.
- [87]. Z. B. Wang, F. Wu, Z. L. Wang, Z. Zhang, J. Z. Zou, C. Liu, Y. G. Liu, X. Cheng, Y. H. Du, Z. C. He, M. L. Gu, Z. G. Wang and R. Feng, "Targeted damage effects of high intensity focused ultrasound (HIFU) on liver tissues of Guizhou Province miniswine", *Ultrason. Sonochem.*, vol. 4, pp. 181-182, 1997.
- [88]. A. Arefiev, F. Prat, J. Y. Chapelon, J. Tavakkoli, and D. Cathignol, "Ultrasound-induced tissue ablation: studies on isolated, perfused porcine liver", *Ultrasound in Medicine & Biology*, vol. 24, pp. 1033-1043, 1998.
- [89]. J. E. Kennedy, "High intensity focused ultrasound: surgery of the future?" *Brit. J. Radiol.*, vol. 76, pp. 590-599, 2003.
- [90]. N. McDannold, G. Clement, P. Black, F. Jolesz, and K. Hynynen, "Transcranial MRI-guided focused ultrasound surgery of brain tumors: Initial findings in three patients", *Neurosurgery*, vol. 66, pp. 323-332, 2011.
- [91]. C. J. Diederich and K. Hynynen, "Ultrasound technology for hyperthermia", *Ultrasound in Medicine & Biology*, vol. 25, pp. 871-887, 1999.
- [92]. M. L. Guzman, "The sesquiterpene lactone parthenolide induces apoptosis of human acute myelogenous leukemia stem and progenitor cells", *Blood*, vol. 105, pp. 4163-4169, 2005.
- [93]. E. Kennedy, "High-intensity focused ultrasound in the treatment of solid tumours", *Med. Ultrasound*, vol. 5, pp. 1-7, 2005.

- [94]. P. He, W. Shou, S. Duan and R. Xia, "Dual-frequency high intensity focused ultrasound (HIFU) accelerating therapy", *Conf. Proc. IEEE Eng. Med. Biol. Soc.*, vol. 1, pp. 213-216, 2005.
- [95]. F. Marquet, M. Pernot, J. F. Aubry, G. Montaldo, L. Marsac, M. Tanter and M. Fink, "Non-invasive transcranial ultrasound therapy based on a 3D CT scan: protocol validation and in vitro results", *Phys. Med. Biol.*, vol. 54, pp. 2597-2613, 2009.
- [96]. C. D. Herickhoff, G. A. Grant, G. W. Britz and s. W. Smith, "Dual-mode IVUS catheter for intracranial image-guided hyperthermia: feasibility study", *IEEE Transactions on, Ultrasonics, Ferroelectrics and Frequency Control*, vol. 57, pp. 2572 - 2584, 2010.
- [97]. A. Blana, B. Walter, S. Rogenhofer and W. F. Wieland, "High-intensity focused ultrasound for the treatment of localized prostate cancer: 5-year experience", *Urology*, vol. 63, pp. 297-300, 2004.
- [98]. P. He, W. Shou, S. Duan and R. M. Xia, "Dual-frequency high intensity focused ultrasound (HIFU) accelerating therapy", *IEEE Engineering in Medicine and Biology Society*, pp. 213-216, 2005.
- [99]. P. A. Tatake and A. B. Pandit, "Modelling and experimental investigation into cavity dynamics and cavitation yield : influence of dual frequency ultrasound sources", *Chem. Eng. Sci.*, vol. 57, pp. 4987-4995, 2002.
- [100]. L. Zhang, H. Zhu, C. Jin, K. Zhou, K. Li, H. Su, W. Chen, J. Bai and Z. Wang, "High-intensity focused ultrasound (HIFU): effective and safe therapy for hepatocellular carcinoma adjacent to major hepatic veins", *Eur. Radiol.*, vol. 19, pp. 437-445, 2009.

- [101]. A. Rybyanets, A. Nasedkin, A. Rybyanets, M. Lugovaya, and T. Domashenkina, "Multi-frequency harmonics technique for HIFU tissue treatment", *IEEE International Ultrasonics Symposium*, pp. 1765-1768, 2009.
- [102]. G. Lerneti, P. Ciuti, N. V. Dezhkunov, M. Reali, A. Francescutto and G. K. Johri, "Enhancement of high-frequency acoustic cavitation effects by a low-frequency stimulation", *Ultrason. Sonochem.*, vol. 4, pp. 263-268, 1997.
- [103]. C. C. Coussios, C. H. Farny, G. Ter Haar and R. A. Roy, "Role of acoustic cavitation in the delivery and monitoring of cancer treatment by high-intensity focused ultrasound (HIFU)", *Int. J. Hyperthermia*, vol. 23, pp. 105-120, 2007.
- [104]. C. H. Farny, R. G. Holt and R. A. Roy, "The correlation between bubble-enhanced HIFU heating and cavitation power", *IEEE T. Bio-Med. Eng.*, vol. 57, pp. 175-184, 2010.
- [105]. L. Carpendo, P. Ciuti, A. Francescutto, G. Lerneti and G. K. Johri, "Space-time interaction of two ultrasonic fields and sonoluminescence during transient cavitation in distilled water", *Acoust. Lett.*, vol. 11, pp. 178-181, 1987.
- [106]. R. Feng, Y. Zhao, C. Zhu and T. J. Mason, "Enhancement of ultrasonic cavitation yield by multi-frequency sonication", *Ultrason. Sonochem.*, vol. 9, pp. 231-236, 2002.
- [107]. S. Guo, X. Jiang and W. Lin, "Tissue Ablation Using Multi-frequency Focused Ultrasound", *IEEE Conference Publications*, pp. 2177-2180, 2011
- [108]. M. Alamolhoda, M. Mokhtari-Dizaji, A. H. Barati and H. Hasanzadeh, "Comparing the in vivo sonodynamic effects of dual- and single-frequency ultrasound in breast adenocarcinoma", *J. Med. Ultrason.*, vol. 39, pp. 115-125, 2012.

- [109]. P. Z. He, R. M. Xia, S. M. Duan, W. D. Shou and D. C. Qian, "The affection on the tissue lesions of difference frequency in dual-frequency high-intensity focused ultrasound (HIFU)", *Ultrason. Sonochem.*, vol. 13, pp. 339-344, 2006.
- [110]. R. Chopra, C. Luginbuhl, F. S. Foster and M. J. Bronskill, "Multifrequency ultrasound transducers for conformal interstitial thermal therapy", *IEEE Transactions on, Ultrasonics, Ferroelectrics and Frequency Control*, vol. 50, pp. 881-889, 2003.
- [111]. R. Krimholtz, D. A. Leedom and G. L. Mattaei, "New equivalent circuits for elementary piezoelectric transducers", *Electron. Lett*, vol. 41, pp. 398-399, 1970.
- [112]. A. Jensen, "Calculation of pressure fields from arbitrarily shaped, apodized, and excited ultrasound transducers", *IEEE Transactions on, Ultrasonics, Ferroelectrics and Frequency Control*, vol. 39, pp. 262-267, 1992.
- [113]. C. Wang, J. Li and M. Zhao, *Piezoelectric & ferroelectric Physical. Beijing: Science Press*, 2009.
- [114]. J. Ma, S. Guo, D. Wu, X. Geng and X. Jiang, "Design, fabrication, and characterization of a single-aperture 1.5-MHz/3-MHz dual-frequency HIFU transducer", *IEEE Transactions on, Ultrasonics, Ferroelectrics and Frequency Control*, vol. 60(7), 2013.
- [115]. S. Guo, Y. Jing and X. Jiang, "Temperature rise in tissue ablation using multi-frequency ultrasound", *IEEE Transactions on, Ultrasonics, Ferroelectrics and Frequency Control*, vol. 60(8), 2013.
- [116]. . R. Bailey, J. A. Reed, B. W. Cunitz, P. J. Kaczowski and L. A. Crum, "Effects of nonlinear propagation, cavitation, and boiling in lesion formation by high intensity focused

ultrasound in a gel phantom", *Journal of the Acoustical Society of America*, vol. 119, pp. 1834 - 1848, 2005.

[117]. G. T. Haar and C. Coussios, "High intensity focused ultrasound: Physical principles and devices", *Int. J. Hyperthermia*, vol. 23, pp. 89 - 104, 2007.

[118]. W. H. Press, S. A. Teukolsky, W. T. Vetterling and B. P. Flannery, *Numerical Recipes*, 3rd ed, pp. 899-946, 2007.

[119]. R. O. Cleveland, O. A. Sapozhnikov, M. R. Bailey and L. A. Crum, "A dual passive cavitation detector for localized detection of lithotripsy-induced cavitation in vitro", *Journal of the Acoustical Society of America*, vol. 107(3), 2000.

[120]. N. McDannold, N. Vykhodtseva and K. Hynynen, "Target disruption of the blood-brain barrier with focused ultrasound: association with cavitation activity", *Phys. Med. Biol.*, vol. 51(4), pp. 793-807, 2006.

[121]. H. Liu, W. Chen, J. Chen, T. Shih, Y. Chen and W. Lin, "Cavitation-enhanced ultrasound thermal therapy by combined low- and high-frequency ultrasound exposure", *Ultrasound in Medicine & Biology*, vol. 32(5), pp. 759-767, 2006.

[122]. C. R. Hill, and G. R. Harr, " High intensity focused ultrasound—potential for cancer treatment", *British Journal of Radiology*, vol. 68, pp. 1296-1303, 1995.

[123]. T. Yu, Z. Wang, and T. J. Mason, " A review of research into the uses of low level ultrasound in cancer therapy", *Ultrason. Sonochem.*, vol. 11, pp. 95-103, 2004.

[124]. J. E. Kennedy, "High-intensity focused ultrasound in the treatment of solid tumours", *Nature Reviews Cancer*, vol. 5, pp. 321-327, 2005.

- [125]. . Xu, T. A. Bigelow, and G. M. Riesberg, "Impact of preconditioning pulse on lesion formation during high-intensity focused ultrasound histotripsy", *Ultrasound in Medicine & Biology*, vol. 38, pp. 1918-1929, 2012.
- [126]. A. Partanen, M. Tillander, P. S. Yarmolenko, B. J. Wood, M. R. Dreher, and M. O. Köhler, "Reduction of peak acoustic pressure and shaping of heated region by use of multifoci sonications in MR-guided high-intensity focused ultrasound mediated mild hyperthermia," *Medical Physics*, vol. 40, pp. 013301, 2013.
- [127]. S. Umemura, K. Kawabata, K. Sasaki, N. Yumita, K. Umemura and R. Nishigaki, "Recent advances in sonodynamic approach to cancer therapy", *Ultrason. Sonochem.*, vol. 3, pp. S187-S191, 1995.
- [128]. H. Shibaguchi, H. Tsuru, M. Kuroki and M. Kuroki, "Sonodynamic cancer therapy: a non-invasive and repeatable approach using low-intensity ultrasound with a sonosensitizer," *Anticancer Research*, vol. 31, pp. 2425–2429, 2011.
- [129]. J. E. Kennedy, G. R. Haar and D. Cranston, "High intensity focused ultrasound: surgery of the future?" *The British Journal of Radiology*, vol. 76, pp. 590-599, 2003.
- [130]. F. P. Curra, D. Mourad and R. O. Cleveland, "Numerical simulations of heating patterns and tissue temperature response due to high-intensity focused ultrasound", *IEEE Transactions on Ultrasonics, Ferroelectrics, and Frequency Control*, vol. 47(4), 2000.
- [131]. P. A. Tatake and A. B. Pandit, "Modeling and experimental investigation into cavity dynamics and cavitation yield: influence of dual frequency ultrasound sources", *Chemical Engineering Science*, vol. 57(22-23), pp. 4987-4995, 2002.

- [132]. L. Zhang, H. Zhu, C. B. Jin, K. Zhou, K. Q. Li, H. B. Su, W. Z. Chen, J. Bai and Z. B. Wang, "High-intensity focused ultrasound (HIFU): effective and safe therapy for hepatocellular carcinoma adjacent to major hepatic veins", *European Radiology*, vol. 19(2), pp. 437-445, 2009.
- [133]. A. N. Rybyanets, M. A. Lugovaya and A. A. Rybyanets, "Multi-Frequency Harmonics Technique for HIFU Tissue Treatment", *9th International Symposium on Therapeutic Ultrasound*, vol. 1215, pp. 291-294, 2010.
- [134]. R. Feng, Y. Y. Zhao, C. P. Zhu and T. J. Mason, "Enhancement of ultrasonic cavitation yield by multi-frequency sonication", *Ultrason. Sonochem.*, vol. 9(5), pp. 231-236, 2002.
- [135]. G. Iernetti, P. Ciuti, N. V. Dezhkunov, M. Reali and A. Francescutto, "Enhancement of high-frequency acoustic cavitation effects by a low-frequency stimulation", *Ultrason. Sonochem.*, vol. 4(3), pp. 263-268, 1997.
- [136]. S. Sokka, T. Gauthier, and K. Hynynen, "Theoretical and experimental validation of a dual-frequency excitation method for spatial control of cavitation", *Physics in Medicine & Biology*, vol. 50(9), pp. 2167-2179, 2005.
- [137]. P. Z. He, R. M. Xia, S. M. Duan, W. D. Shou and D. C. Qian, "The affection on the tissue lesions of difference frequency in dual-frequency high-intensity focused ultrasound (HIFU)," *Ultrason. Sonochem.*, vol. 13, pp. 339-344, 2006.
- [138]. S. Guo, Y. Jing and X. Jiang, "Temperature rise in tissue ablation using multi-frequency ultrasound", *IEEE Transactions on Ultrasonics, Ferroelectrics and Frequency Control*, vol. 60(8), pp. 1699-1707, 2013.

- [139]. M. S. Plesset, A. Prosperetti, "Bubble Dynamics and Cavitation", *Annu. Rev. Fluid Mech.*, vol. 9, pp. 145-185, 1977.
- [140]. F. R. Gilmore, "The growth or collapse of a spherical bubble in a viscous compressible liquid," unpublished.
- [141]. M. R. Bailey, J. A. Reed, B. W. Cunitz, P. J. Kaczkowski and L. A. Crum, "Effects of nonlinear propagation, cavitation, and boiling in lesion formation by high intensity focused ultrasound in a gel phantom", *Journal of the Acoustical Society of America*, vol. 119, pp. 1834 - 1848, 2005.
- [142]. A. Prosperetti, "A generalization of the Rayleigh-Plesset equation of bubble dynamics", *Phys. Fluids*, vol. 25(3), pp. 409-410, 1982.
- [143]. C. Brennen, "Spherical Bubble Dynamics", *Oxford University Press*, 1995.
- [144]. C. C. Church, "A theoretical study of cavitation generated by an extracorporal shock wave lithotripter", *Journal of the Acoustical Society of America*, vol. 86, pp. 215-227, 1989.
- [145]. M. J. Choi, A. J. Coleman and J. E. Saunders, "The influence of fluid properties and pulse amplitude on bubble dynamics in the field of a shock wave lithotripter", *Physics in Medicine & Biology*, vol. 38, pp. 1561-1573, 1993.
- [146]. R. O. Cleveland, O. A. Sapozhnikov, M. R. Bailey and L. A. Crum, "A dual passive cavitation detector for localized detection of lithotripsy-induced cavitation in vitro," *Journal of the Acoustical Society of America*, vol. 107(3), 2000.
- [147]. J. Ma, S. Guo, D. Wu, X. Geng and X. Jiang, "Design, fabrication, and characterization of a single-aperture 1.5-MHz/3-MHz dual-frequency HIFU

transducer", *IEEE Transactions on Ultrasonics, Ferroelectrics and Frequency Control*, vol. 60(7), 2013.

[148]. W. H. Press, S. A. Teukolsky, W. T. Vetterling, and B. P. Flannery, *Numerical Recipes*, 3rd edition, pp 899-946, 2007.

[149]. Y. T. Didenko and K. S. Suslick, "The energy efficiency of formation of photons, radicals and ions during single-bubble cavitation", *Nature*, vol. 418, pp. 394-397, 2002.

APPENDICES

Appendix I

% Appendix I is a Matlab code using Field II toolbox to simulate the linear acoustic field of a piston ultrasound transducer. Input parameters of this transducer are 30 mm-focal length and 29 mm aperture.

fetal=1; % Whether to use cardiac or fetal intensities

% Set values for the intensity

P0 = 10e3; % surface pressure

a1 = 30; a2 = 0; a3 = 0; % focal length

b1 = 50; % total graph length

c1 = 0; % 1 for pressure (MPa), 0 for dB

d1 = 25; % total width

e1 = 2; % 1 for width, 2 for height

f0 = 1.5e6;

if (fetal==1)

% For fetal

```

Z=1.480e6;      % Characteristic acoustic impedance [kg/(m^2 s)]

                % Transducer center frequency [Hz]

M=3;

Tprf=1/100;     % Pulse repetition frequency [s]

Tp=M/f0;       % Pulse duration [s]


Ispta=P0^2/2/Z*Tp/Tprf;    % Fetal intensity: Ispta [w/m^2]

%Ispta=0.046*100^2;    % Fetal intensity In Situ: Ispta [w/m^2]

Itype='Fetal';      % Intensity type used


else


% For cardiac

M=8;              % Number of cycles in pulse

Ispta=0.730*100^2;    % Cardiac intensity: Ispta [w/m^2]

Itype='Cardiac';     % Intensity type used

end


% Generate the transducer apertures for send and receive


fs=200*f0;        % Sampling frequency [Hz]

```

```

c=1540;           % Speed of sound [m/s]

lambda=c/f0;      % Wavelength

% Set initial parameters

elefocus = 0;

Rconvex = 29/1000;

no_sub_x = 2;

no_sub_y = 12;

height=12/1000; % Height of element [m]

width=(0.54/4-0.035)/1000; % Width of element [m]

kerf=0.035/1000; % Distance between transducer elements [m]

no_elements=1; % Number of elements

focus=[a2 a3 a1]/1000; % Initial electronic focus

R=14/1000; % Radius of transducer

ele_size=1/1000; % Size of mathematical elements

focal_radius=30/1000;

% f0 and use this:

```

```

set_field ('att',2.5*100);

set_field ('Freq_att',0.5*100/1e6);

set_field ('att_f0',f0);

set_field ('use_att',0);      % Set this flag to one when including attenuation


% Set the sampling frequency


set_sampling(fs);


% Make the aperture for the rectangles


if (elefocus == 0)

    ape = xdc_concave (R, focal_radius, ele_size);

    ape = xdc_convex_array (no_elements, width, height, kerf, Rconvex, no_sub_x, no_sub_y,
focus);

end


% Set the excitation of the aperture


excitation=sin(2*pi*f0*(0:1/fs:M/f0));

excitation=excitation.*hanning(length(excitation));

xdc_excitation (ape, excitation);

```

```

% Set the impulse response of the aperture

impulse=sin(2*pi*f0*(0:1/fs:1/f0));

impulse=impulse.*hanning(length(impulse))';

xdc_impulse (ape, impulse);


% Find the scaling factor from the peak value


point=[0 0 0]/1000;

zvalues=(1:0.1:10)/1000;

index=1;

I=0;

P=0;

disp('Finding calibration...')

for z=zvalues

    point(3)=z;

    [y,t] = calc_hp(ape,point);

    I(index)=sum(y.*y)/(2*Z)/fs/Tprf;

    P(index)=max(y);

    index=index+1;

end

I_factor=Ispta/I(1);

```

```

% Set the correct scale factor

scale_factor=sqrt(I_factor);

excitation=scale_factor*excitation;

xdc_excitation (ape, excitation);


% Make the calculation in elevation


disp('Finding pressure and intensity.. ')

point=[0 0 0]/1000;

zvalues=(5:0.1:b1)/1000;

avalues=(-d1:0.1:d1)/1000;

index=1;

I=0;

II=zeros(b1*10-9,20*d1+1);

Ppeak=0;

PPpeak=zeros(b1*10-49,20*d1+1);

for z=zvalues

    if rem(z*1000,10)==0

        disp(['Calculating at distance ',num2str(z*1000),' mm'])

    end

    point(3)=z;

```

```

aa=1;

for a=avalues

    point(e1)=a;

    [yy,t] = calc_hp(ape,point);

    II(index,aa)=sum(yy.*yy)/(2*Z)/fs/Tprf;

    PPpeak(index,aa)=sqrt(II(index,aa)*2*Z);

    aa=aa+1;

end

index=index+1;

end

Pmean=sqrt(I*2*Z*Tprf/Tp);

III=20*log((II*1000/(100^2))/(max(max(II))*1000/(100^2)));

PPP=20*log((PPpeak/1e6)/(max(max(PPpeak))/1e6)));

% Plot the calculated response

allfonds = 25;

figure(1)

if (c1 == 1)

```

```

a = mesh(avalues*1000,zvalues*1000,PPpeak/1e6)

xlabel('Pressure [MPa]','FontSize',allfonds)

else

    a= mesh(avalues*1000,zvalues*1000,PPP)

    xlabel('Pressure [dB]','FontSize',allfonds)

end

xlabel('Lateral distance [mm]','FontSize',allfonds);

ylabel('Axial distance [mm]','FontSize',allfonds);

set(gca,'FontSize',allfonds,'XGrid','on');

set(gca,'FontSize',allfonds,'YGrid','on');


set(gcf,'PaperPosition',[0.1 0.1 12 12]);

print('-dpng','1');


figure(2)


if (c1 == 1)

b = plot(zvalues*1000,PPpeak(:,10*d1+1)/1e6);

else

    b = plot(zvalues*1000,20*log(PPpeak(:,10*d1+1)/max(PPpeak(:,10*d1+1))));

```



```

xlabel('Axial distance [mm]', 'FontSize', allfonds+15);

ylabel('Pressure [dB]', 'FontSize', allfonds+15);

set(gca, 'FontSize', allfonds+15, 'XGrid', 'on');

set(gca, 'FontSize', allfonds+15, 'YGrid', 'on');

xlim([0, 50]);

set(b, 'LineWidth', 2);

set(gcf, 'PaperPosition', [0.1 0.1 12 12]);

print('-dpng', '2');

end

figure(3)

if (c1 == 1)

plot(avalues*1000, PPpeak(301, :)/1e6);

xlabel('Lateral distance [mm]')

ylabel('Pressure [MPa]')

else

plot(avalues*1000, 20*log(PPpeak(301, :)/max(PPpeak(301, :))));

xlabel('Lateral distance [mm]')

ylabel('Pressure [dB]')

end

```

```
% Release the aperture
```

```
xdc_free(ape);
```

Appendix II

% Appendix II is a Matlab code using k-wave toolbox to simulate the non-linear acoustic field of dual-frequency (1.5 MHz and 3.3 MHz) transducers.

clear all;

% create the computational grid

Nx = 80; % number of grid points in the x (row) direction

Ny = 80; % number of grid points in the y (column) direction

Nz = 80;

dx = 0.1e-3; % grid point spacing in the x direction [m]

dy = 0.1e-3; % grid point spacing in the y direction [m]

dz = 0.1e-3;

kgrid = makeGrid(Nx, dx, Ny, dy, Nz, dz);

% define the properties of the propagation medium

medium.sound_speed = 1500*ones(Nx, Ny, Nz); % [m/s]

medium.sound_speed(Nx/2:Nx, :, :) = 2000; % [m/s]

medium.density = 1000*ones(Nx, Ny, Nz); % [kg/m³]

medium.density(Nx/2:Nx, :, :) = 1200; % [kg/m³]

medium.alpha_coeff = 0.75*ones(Nx, Ny, Nz); % [dB/(MHz^y cm)]

```

medium.alpha_coeff(Nx/2:Nx, :, :) = 8;

medium.alpha_power = 1.5;

% define properties of the input signal
source_strength = 1e6;      % [MPa]

tone_burst_freq_1 = 1.5e6;   % [Hz]
tone_burst_freq_2 = 3.3e6;   % [Hz]
tone_burst_cycles = 10;

total_time = 1/tone_burst_freq*20;

[kgrid.t_array, dt] = makeTime(kgrid, medium.sound_speed,0.3,total_time);

% create the input signal using toneBurst
input_signal = toneBurst(1/kgrid.dt, tone_burst_freq, tone_burst_cycles);

% scale the source magnitude by the source_strength divided by the
% impedance (the source is assigned to the particle velocity)
input_signal =
(source_strength/(medium.sound_speed(1,1,1)*medium.density(1,1,1)))*input_signal;

% physical properties of the transducer
transducer.number_elements = 30; % total number of transducer elements

```

```

transducer.element_width = 2;    % width of each element [grid points]

transducer.element_length = 60;  % length of each element [grid points]

transducer.element_spacing = 0;  % spacing (kerf width) between the elements [grid points]

transducer.radius = inf;         % radius of curvature of the transducer [m]


% calculate the width of the transducer in grid points

transducer_width = transducer.number_elements*transducer.element_width ...
    + (transducer.number_elements - 1)*transducer.element_spacing;


% use this to position the transducer in the middle of the computational grid

transducer.position = round([1,    Ny/2    -    transducer_width/2,    Nz/2    -
transducer.element_length/2]);


% properties used to derive the beamforming delays

transducer.sound_speed = 1540;    % sound speed [m/s]

transducer.focus_distance = 7e-3;    % focus distance [m]

transducer.elevation_focus_distance = 7e-3; % focus distance in the elevation plane [m]

transducer.steering_angle = 0;    % steering angle [degrees]


% append input signal used to drive the transducer

transducer.input_signal = input_signal;

```

```

% create the transducer using the defined settings

transducer = makeTransducer(kgrid, transducer);

% define a sensor mask through the central plane of the transducer

sensor.mask = zeros(Nx, Ny, Nz);

sensor.mask(:, :, Nz/2) = 1;

% set the record mode such that only the rms and peak values are stored

sensor.record = {'p_rms', 'p_max', 'p'};

% run the simulation

sensor_data = kspaceFirstOrder3D(kgrid, medium, transducer, sensor);

% reshape the returned rms and max fields to their original position

sensor_data.p_rms = reshape(sensor_data.p_rms, [Nx, Ny]);

sensor_data.p_max = reshape(sensor_data.p_max, [Nx, Ny]);

% view final pressure field

allfonds = 15;

time = size(sensor_data.p);

figure(1)

```

```
mesh(10:1:Nx-10,10:1:Ny-10,sensor_data.p_rms(10:Nx-10,10:Ny-10));  
  
set(gcf,'paperposition',[0 0 5 5]);  
  
print('-dpng','a');
```

Appendix III

% Appendix III is a Matlab code to solve the Gilmore equation which is used to calculate bubble dynamics under ultrasonic excitation. In addition, the radiated force is calculated based on bubble dynamics.

clear all;

global c fs dtq fo w Pa phi Ro rho1 Po mu_sh_eps mu_liquid chi gam sigma shell_thick
b_van Vm;

allfonds = 30;

c = 1540; % speed of sound mks units

fs = 100e6; % sampling frequency

dtq = 1/fs; % sampling interval

fo_list = [1.5e6]; % center frequency

% w = 2*pi*fo; % angular frequency

phi = 0; % initial phase of the driving pulse

phi2=0;


```

% Ro_list = 1.8e-6;           % bubble initial radius in meter

Ro_list = [1.8e-6];

rhof = 1000;                  % liquid density

Po = 101.3e3;                 % ambient pressure

mu_liquid = 0.01;            % liquid viscosity

chi = 0.50;                   % shell elastic modulus

gam = 1.07;                   % polytropic gas exponent

sigma = 0.051;                % interfacial tension

shell_thick = 1e-9;           % shell thickness, assume 2 nm

b_van = 0.1727;               % L/mol, volume of a gas molecule

Vm = 22.4;                    % L/mol, gas constant

Nf = length(fo_list);

Nr = length(Ro_list);

Rmax = zeros(Nf,Nr);

Rmin = zeros(Nf,Nr);

Emax = zeros(Nf,Nr);

Emin = zeros(Nf,Nr);

Erms = zeros(Nf,Nr);

phead = zeros(1,500);        % add some zeros in the head and tail

```

```
Pa = 0*1.5e6; % PPpeak(fl,d1+1);          % amplitude of driving pressure in Pascals
```

```
Pa2= 1*1e6; % PPpeak2(fl,d1+1);
```

```
ncyc = 5;          % number of cycles in waveform
```

```
for mm = 1:Nf
```

```
    fo = 1.5e6; % fo_list(mm);
```

```
    fo/1e6
```

```
    w = 2*pi*fo;
```

```
    f0_1 = 3e6;
```

```
    f0_1/1e6
```

```
    w2= 2*pi*f0_1;
```

```
    % driving pulse
```

```
    tpulse = 0:dtq:ncyc/1e6;      % time index for driving pulse
```

```
    % tpulse1 = 0:dtq:ncyc/f0_1;
```

```
    pdr = Pa*sin(w*tpulse + phi)+Pa2*sin(w2*tpulse + phi2);%.*blackman(length(tpulse)).';
```

```

figure(1);

aaa = plot(tpulse,pdr);set(aaa,'LineWidth',2); print('-dpng','c');

rms_pdr(mm) = sqrt(mean(pdr.^2));      % pulse rms for normlization

pr = [phead pdr phead];
t = (0:length(pr)-1)*dtq;

% filter for the transducer bandwidth

filt_pr = pr;

Plist_n = -min(filt_pr);      % Max negative pressure (as a positive value)

pdrive = struct('omega',w,'hyd',filt_pr,'t',t*w,'Pmin',Plist_n);

figure(2);

plot(t,pr,'r',t,filt_pr,'b');

% [max(pr) max(filt_pr)]

% [min(pr) min(filt_pr)]

```

```

for m = 1:Nr

    Ro = Ro_list(m);

%    Ro*1e6

    mu_sh_eps = max(0,(1.90*Ro/1e-6 - 1.1)*1e-9);

% run differential eqn. solver

[t_rp,y_rp] = ode23(('model'),[0 max(pdrive.t)],[1; 0;],[],pdrive);

dtq_rp = t_rp/w;                % redimensionalize the time

r = y_rp(:,1)*Ro;                % redimensionalize the wall radius

rdot = y_rp(:,2)*Ro*w;           % calculate the wall velocity

rdotdot = accel*Ro*w^2;          % calculate the wall acceleratio

r_interp = interp1(dtq_rp,r,t);  % interpolate to the same time scale

rdot_interp = interp1(dtq_rp,rdot,t); % interpolate to the same time scale

rdotdot_interp = interp1(dtq_rp,rdotdot,t); % interpolate to the same time scale

end;

end;

f0 = fo_list/1e6;

d0 = 2*Ro_list*1e6;

```

```
save echo_20cyc.mat Rmax Rmin Emax Emin Erms rms_pdr f0 d0;
```

```
figure(3); a = plot(t,r_interp);  
  
xlabel('time(s)','FontSize',allfonds);  
  
ylabel('bubble size (m)','FontSize',allfonds);  
  
set(gca,'FontSize',allfonds,'XGrid','off');  
  
set(gca,'FontSize',allfonds,'YGrid','off');  
  
set(a,'Color','red','LineWidth',2);  
  
print('-dpng','a');
```

```
figure(4); b = plot(t,r_dot_interp);  
  
xlabel('time(s)','FontSize',allfonds);  
  
ylabel('Radiated pressure (kPa)','FontSize',allfonds);  
  
set(gca,'FontSize',allfonds,'XGrid','off');  
  
set(gca,'FontSize',allfonds,'YGrid','off');  
  
set(b,'Color','red','LineWidth',2);  
  
print('-dpng','b');
```

```
sqrt(mean(r_dot_interp.^2))
```

```
figure(5); b = plot(t,r_dotdot_interp);  
  
xlabel('time(s)','FontSize',allfonds);  
  
ylabel('Radiated pressure (Pa)','FontSize',allfonds);  
  
set(gca,'FontSize',allfonds,'XGrid','off');
```

```

set(gca,'FontSize',allfonds,'YGrid','off');

set(b,'Color','red','LineWidth',2);

% print('-dpng','b');

sqrt(mean(rdotdot_interp.^2))

Fs = 1e8;

T = 1/Fs;

L = length(t);

tt = (0:L-1)*T;

NFFT = 2^nextpow2(L);

Y = fft(rdot_interp,NFFT)/L;

f = Fs/2*linspace(0,1,NFFT/2+1);

FFT = 2*abs(Y(1:NFFT/2+1));

figure(6);

e = plot(f,2*abs(Y(1:NFFT/2+1)));

% e = plot(f,20*log(FFT/max(FFT)));

xlim([0,15e6]);

xlabel('Frequency (Hz)','FontSize',allfonds);

% ylabel('Amplitude (dB)','FontSize',allfonds);

```

```

ylabel('Amplitude (kPa)','FontSize',allfonds);

set(gca,'FontSize',allfonds,'XGrid','on');

set(gca,'FontSize',allfonds,'YGrid','on');

set(e,'Color','red','LineWidth',2);

print('-dpng','e');

%Code for cavitation radiation force

tvalues=1:length(t);

ivalues=f1:b1;

jvalues=-d1:d1;

for i=ivalues

for j=jvalues

for t1=tvalues

A((i-f1+1),j+d1+1,t1)=1000*r_interp(t1)/sqrt((30-i)^2+(0-
j)^2)*1000*(2*r_dot_interp(t1)).^2+r_interp(t1)*r_dotdot_interp(t1);

end

end

end

for x=1:length(ivalues)

for y=1:length(jvalues)

```

```

rmx=A(x,y,:);

RMQ(x,y)=1/length(tvalues).*sum(rmx.^2);

end

end

Irad=RMQ.^2/1000/c;

for i=ivalues
for j=jvalues
Drad=4*pi*((sqrt((a1-i)^2+(0-j)^2))/1000)^.2.*Irad;
end
end

for i=ivalues
for j=jvalues
Dabs=Drad.*(1-exp(-2/13.5*(sqrt((a1-i)^2+(0-j)^2)/1000)));
end
end

for i=ivalues
for j=jvalues
qb=Dabs.*4/3/pi/((sqrt((a1-i)^2+(0-j)^2))/1000)^3;

```


end

end

```
function dy = model(t,y,flag,driv)
```

```
global c w Ro rho_l Po mu_sh_eps mu_liquid chi gam sigma shell_thick b_van Vm;
```

```
% y(1) is R non-dimensional
```

```
% y(2) is Rdot non-dimensional
```

```
P = interp1(driv.t,driv.hyd,t);
```

```
Rnd = y(1);      % Rnd = R/Ro
```

```
R = Ro*y(1);
```

```
Rdot = Ro*w*y(2);
```

```
temp = (Po+2*sigma/Ro+2*chi/Ro)*((1 - b_van/Vm)./(Rnd^3 - b_van/Vm))^gam;
```

```
term1 = rho_l*Rnd*w^2*Ro^2/Po;      % term in front of Rnd_dot_dot
```

```
Rdotdot = - 3/2*rho_l*(Rdot^2)/Po ...
```

```
+ temp*(1-3*gam/c*Rdot)/Po ...
```

$$\begin{aligned}
 & - 4 \mu_{\text{liquid}} \dot{R} / R / P_o \dots \\
 & - 2 \sigma / R (1 - \dot{R} / c) / P_o \dots \\
 & - (1 - 3 \dot{R} / c) / P_o \dots \\
 & - (P_o + P) / P_o;
 \end{aligned}$$

$$\ddot{R} = \ddot{R} / \text{term1};$$

$$dy = [y(2); \ddot{R}];$$